Structure, ionic conductivity and mobile carrier density in fast ionic conducting chalcogenide glasses

by

Wenlong Yao

A dissertation submitted to the graduate faculty

in partial fulfillment of the requirements for the degree of

DOCTOR OF PHILOSOPHY

Major: Materials Science and Engineering

Program of Study Committee:
Steve W. Martin, Major Professor
Alan Goldman
Kurt Hebert
Vitalij Pecharsky
Xiaoli Tan

Iowa State University

Ames, Iowa

2006

Graduate College

Iowa State University

This is to certify that the doctoral dissertation of

Wenlong Yao

has met the dissertation requirements of Iowa State University

Major Professor

Dedicated to my parents, my wife and my daughter

Table of Contents

IS-T 2687

1. General Introduction

1.1 Thesis introduction

Ionic conduction in glassy materials have been investigated since 1884 when Warburg placed a d.c. electrical field on a glass, and observed an electrolytic (Na^+) transport [1]. More recently, ionic glasses have attracted attention from the fast-ion conductor community due to their application as solid electrolytes in electrochemical energy storage systems, such as rechargeable batteries and fuel cells. Glassy electrolytes show some advantages over their crystalline counterparts: isotropic conductivity, absence of grain boundaries, wide compositional flexibility, and easy fabrication into complex shapes.

Many hundreds of glass compositions have been studied, but most have been silver- and alkali-ion conductors. It is observed that the ionic conductivity in these glassy electrolytes has never exceeded ~10^{-2} $(\Omega cm)^{-1}$ at 25 °C as shown in Figure 1-1 [2]. The only exception is AgI + Ag_2O + M_xO_y (M_xO_y=B_2O_3, GeO_2, P_2O_5, MoO_3) glass-ceramic composites which exhibit a conductivity between 10^{-2} and 10^{-1} $(\Omega cm)^{-1}$ at 25 °C [3,4]. The higher conductivity of these α-AgI doped materials arises from the α-AgI crystallites being homogeneously dispersed in the super-ionic glass. The conductivity maximum limitation is thought to be a generic feature of FIC glasses. To date, however, there has been no definitive understanding provided for this conductivity maximum, yet the implications of the conductivity maximum in the performance of batteries and fuel cells are important.

The ionic conductivity is usually given as:

$$\sigma(T) = n(T) \cdot Z \cdot e \cdot \mu(T) \qquad \text{Equation 1-1}$$

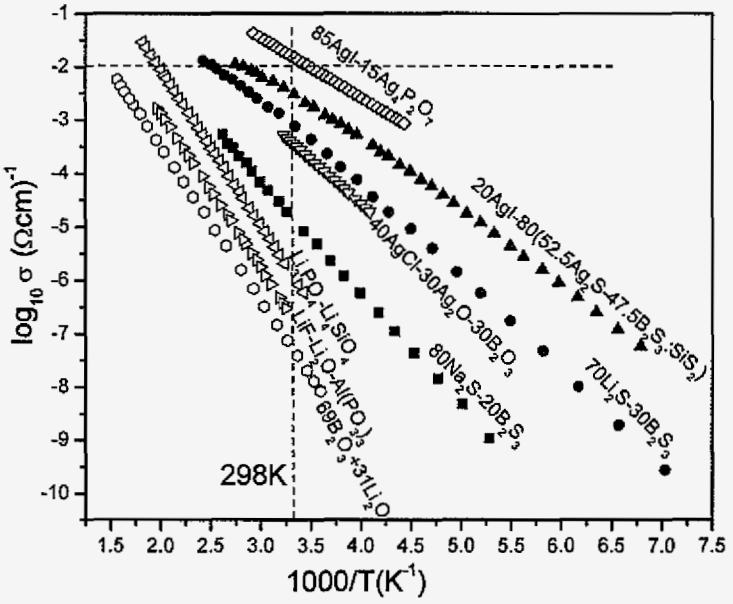

Figure 1-1 Conductivities dependent of temperature of some oxide and chalcogenide glasses

and as such it depends on the number density of charge carriers, n (T), valence of the carrier, Z, fundamental charge unit, e, and mobility of the charge carriers, μ (T). The most important factors are the number density of charge carrier and the mobility of charge carrier. To understand the conductivity maximum limitation in glassy electrolytes, the best way is through independent measurements of charge carrier density and mobility of charge carrier, which can decide whether n(T) or μ(T) or both limit the conductivity in glassy electrolytes. In the experiments proposed here, we will concentrate on the study of space charge polarization to determine the number density of the charge carriers in glassy electrolytes where the influence of n(T) and μ(T) on the ionic conductivity can be separated. With the knowledge of the n(T), μ(T), the ionic conductivity and the structure of the studied glasses,

the conductivity of glasses can be optimized based on the understanding of conductivity maximum limitation in glassy electrolytes.

1.2 Thesis organization

This thesis consists of six sections. The first section gives the basic research background on the ionic conduction mechanism in glass, polarization in the glass, and the method of determining the mobile carrier density in glass. The proposed work is also included in this section.

The second section is a paper that characterizes the structure of MI + M_2S + ($0.1Ga_2S_3$ + $0.9GeS_2$) (M = Li, Na, K and Cs) glasses using Raman and IR spectroscopy. Since the ionic radius plays an important role in determining the ionic conductivity in glasses, the glass forming range for the addition of different alkalis into the basic glass forming system $0.1Ga_2S_3 + 0.9GeS_2$ was studied. The study found that the change of the alkali radius for the same nominal composition causes significant structure change to the glasses.

The third section is a paper that investigates the ionic conductivity of MI + M_2S + ($0.1Ga_2S_3$ + $0.9GeS_2$) (M = Li, Na, K and Cs) glasses system. Corresponding to the compositional changes in these fast ionic conducting glasses, the ionic conductivity shows changes due to the induced structural changes. The ionic radius effect on the ionic conductivity in these glasses was investigated.

The fourth section is a paper that examines the mobile carrier density based upon the measurements of space charge polarization. For the first time, the charge carrier number density in fast ionic conducting chalcogenide glasses was determined. The experimental impedance data were fitted using equivalent circuits and the obtained parameters were used

to determine the mobile carrier density. The influence of mobile carrier density and mobility on the ionic conductivity was separated.

The fifth section is a paper that studies the structures of low-alkali-content $Na_2S + B_2S_3$ ($x \leq 0.2$) glasses by neutron and synchrotron x-ray diffraction. Similar results were obtained both in neutron and synchrotron x-ray diffraction experiments. The results provide direct structural evidence that doping B_2S_3 with Na_2S creates a large fraction of tetrahedrally coordinated boron in the glass.

The final section is the general conclusion of this thesis and the suggested future work that could be conducted to expand upon this research.

1.3 Background of research

1.3.1 Ion conduction mechanisms in glass

The total conductivity of a system is given by the sum of the contributions of all of charge carriers. In most glass systems only one charge carrier exists, so the ionic conductivity in these solid electrolytes is represented as shown in Equation 1-2 to Equation 1-5 [5,6]:

$$\sigma(T) = n(T) \cdot Z \cdot e \cdot \mu(T) = \frac{\sigma_0}{T} \exp\left(\frac{-\Delta E_{act}}{RT}\right) \qquad \text{Equation 1-2}$$

$$n(T) = n_o \exp\left(\frac{-\Delta E_b}{RT}\right) \qquad \text{Equation 1-3}$$

$$\mu(T) = \frac{\mu_0}{T} \exp\left(\frac{-\Delta E_s}{RT}\right) \qquad \text{Equation 1-4}$$

$$\sigma(T) = \frac{n_0 \mu_0 Ze}{T} \exp\left(\frac{-(\Delta E_b + \Delta E_s)}{RT}\right) \qquad \text{Equation 1-5}$$

Here $n(T)$ is the T dependent number density of charge carriers, Z is the valence of the mobile ion, e fundamental unit of charge and $\mu(T)$ is the T dependent mobility of carrier, σ_0, μ_0, n_0 are pre-exponents in the functions, respectively. The conductivity usually behaves in Arrhenius temperature dependence. ΔE_{act} is the total conductivity activation energy, ΔE_b (or ΔE_c) is binding energy (or Coulomb energy) and ΔE_s (or ΔE_m) is strain energy (or migration energy) and $\Delta E_{act} = \Delta E_b + \Delta E_s$. When a charge carrier in a glass transports, it experiences two processes: dissociation and migration, as shown in Figure 1-2 [7]. The charge carrier, usually a cation, dissociates from the anion, such as non-bridging oxygen and then transports to the next available position through the pathway in the glass network.

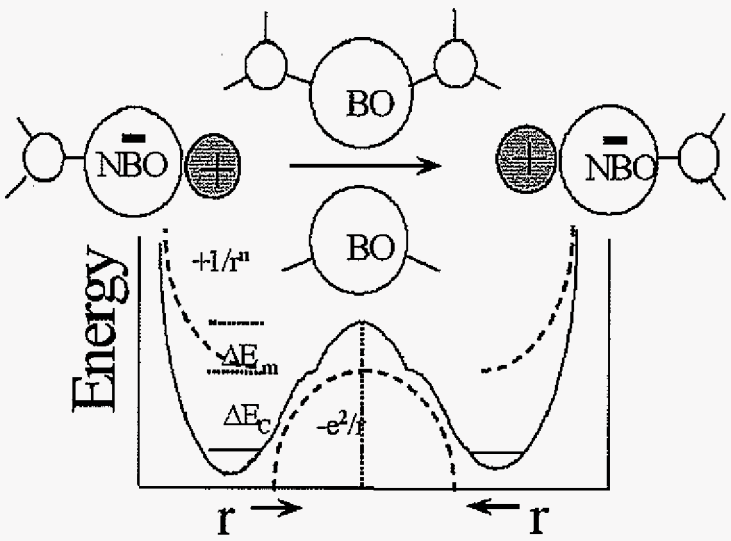

Figure 1-2 A pictorial view of ion transport in glass accounting for the two activation energies [7]

In practice, it is found that the pre-exponent, σ_0, does not change much with composition, so most researchers focus on the study of the behavior of the conductivity

activation energy. Two extreme conduction behaviors have been considered in these glasses. One is the strong-electrolyte behavior which assumes the carrier density *n(T)* is independent of temperature and all ions in the glass are mobile and the strain energy dominates the d.c. conductivity [8,9,10,11]. Another is the weak-electrolyte behavior which assumes that mobility $\mu(T)$ is independent of ion concentration or temperature and the Coulomb energy dominates the d.c. conductivity [12,13]. While many models of ionic conduction in glasses have been proposed, the most widely used models are discussed in the following.

1.3.1.1 The Anderson-Stuart model

In 1954, Anderson and Stuart first proposed a model for the activation energy in ion conducting glasses [8]. The activation energy for the d.c. conductivity, ΔE_{act}, was considered from a microscopic prospective. The activation energy was assumed to be the energy required to move the ion, presupposing that the structure remains unchanged, plus the energy required to deform the structure enough to allow the ion to pass.

The strain energy, taken as similar to the solution of a close-packed liquid, for glasses was given after modification as:

$$\Delta E_s = 4\pi \cdot G r_D (r - r_D)^2 \qquad \text{Equation 1-6}$$

Here, r is the cation radius, r_D is the "doorway" radius in the glasses enough to accommodate the cation, and G is the shear modulus of glass. This energy represents the energy required to dilate the structure from its original radius r_D out to the radius of the cation r.

The Coulomb energy or binding energy was estimated from the ionic crystal theory, making some modification due to the difference between glass systems and ionic crystals, and is shown in the following equation:

$$\Delta E_b = \frac{\beta z z_O e^2}{\gamma(r + r_O)} \qquad \text{Equation 1-7}$$

Here z_O and r_O are the charge and radius of the O^{-2} ion, respectively, β is a lattice parameter depending on the distance between neighboring sites, z is the charge of cation, γ is a covalency parameter, equal to dielectric constant in practical.

Through the Anderson and Stuart model, the total activation energy can be given by:

$$\Delta E_{act} = \Delta E_s + \Delta E_b = \frac{\beta z z_O e^2}{\gamma(r + r_O)} + 4\pi \cdot G r_D (r - r_D)^2 \qquad \text{Equation 1-8}$$

The Anderson-Stuart model has been extensively applied to alkali oxide glasses, mixed anion conductor, some chalcogenide glasses and even to new Li^+ ion conducting glasses [14,15,16,17,18]. It can explain the conductivity behavior with the composition change in the glass.

1.3.1.2 The Weak-electrolyte model

The weak-electrolyte model was proposed initially by Ravaine and Souquet in 1977 [12, 13]. It is based on correlations between the ionic conductivity and thermodynamic activity of fast-ion conducting glass. It is assumed that not all modifier cations are mobile.

It is considered that the following reaction exists in the glass where there is an addition of modifiers or dopant salts MX:

$$MX \Leftrightarrow M^+ + X^- \qquad \text{Equation 1-9}$$

Where M^+ is the mobile cation and X^- are the dissociated anions, such as M^+=Li^+, X^-=OLi^- or I^-, not all modifier cations are presumed to be mobile. An empirical relation was established such that:

$$\sigma = cont \cdot [a(MX)] \qquad \text{Equation 1-10}$$

From conventional thermodynamics assuming constant activity coeffients and charge neutrality, Equation 1-10 becomes:

$$\sigma = cont \cdot [M^+] \qquad \text{Equation 1-11}$$

Clearly it implies that M^+ ion mobility is independent of glass composition.

The overall activation energy for ionic conductivity therefore can be given as [19]:

$$\Delta E_{act} = \Delta H / 2 + \Delta E_s \qquad \text{Equation 1-12}$$

where ΔH is the enthalpy of reaction and ΔE_s is the strain energy.

In the AgI + $AgPO_3$ glasses, it was found that $\sigma = cont \cdot [a(AgI)]^{0.6}$ [20], which was used as early support for the weak-electrolyte theory. Thermodynamic analyses also have been applied to the mixed alkali effect, conductivity enhancement by halide salts and the mixed anion effect [21,22,23].

1.3.2 Space charge polarization in glass

1.3.2.1 Polarization in glass

From the Anderson-Stuart model and the weak-electrolyte model, it is known that binding energy and strain energy are important in determining the activation energy which will affect the conductivity of glass. To understand the conductivity maximum limitation, independent measurements of number of charge carrier and mobility of charge carrier dependence of temperature are good methods, which provide binding energy and strain

energy according to Equation 1-3 and Equation 1-4. Here it is proposed that space charge polarization measurements can be used to determine the density of charge carrier dependent of temperature in the ionic glass and in this way the binding energy of ionic glasses can be determined.

Four types of polarization exist in ionic electrolyte (including crystals and glasses), see Figure 1-3 [24]:

a. Polarization of permanent dipoles by the external electric field (Orientation polarization).

b. Displacement of the atom core from its equilibrium position causing induced dipoles (atomic polarization).

c. Displacement of the electronic cloud around an atom also causing an induced dipole (electronic polarization).

d. Displacement of ions in a material which causes an ion rich region and a vacancy rich region (space charge polarization).

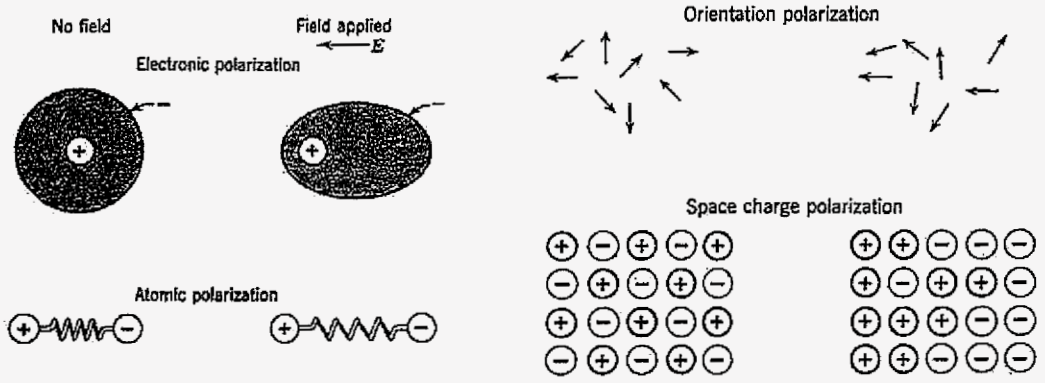

Figure 1-3 Four types of polarization in ionic electrolytes [24]

The frequency dependence of the dielectric responses is summarized in Figure 1-4. The contribution of polarization processes depend upon the temperature and the frequency of the applied electric field. It is seen that in the low frequency region the space charge polarization can contribute to the dielectric, which means that when the electric field switches, the space charge relaxes at a slow rate, requiring minutes or even hours.

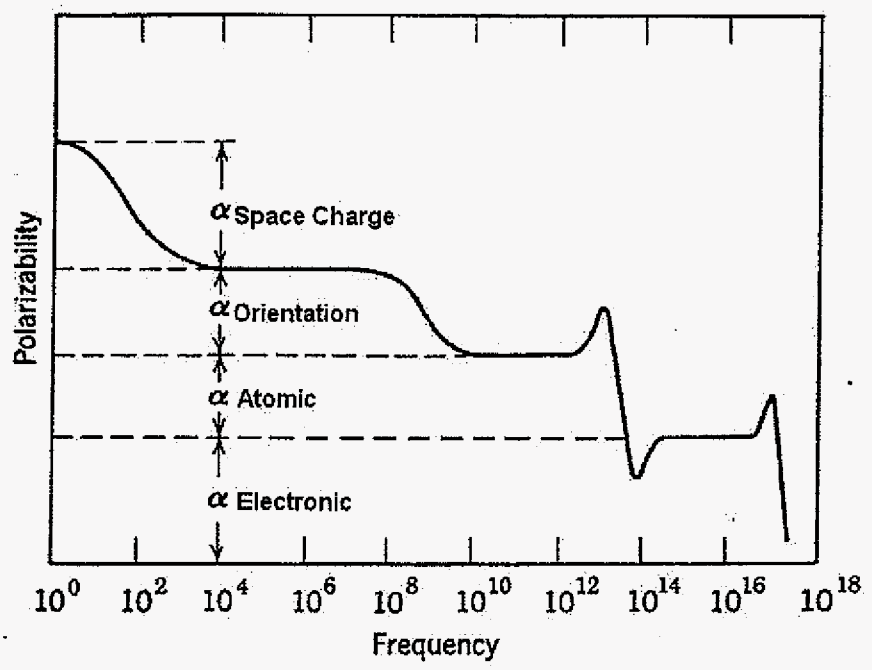

Figure 1-4 Frequency dependent of polarization processes [24]

In glasses below their glass transition temperature, the orientation polarization doesn't exist due to the rigid frozen nature of the network structure. While electronic polarization takes place at much higher frequency (UV region). Only atomic polarization and space charge polarization can be considered in the range of our study.

The complex dielectric function $\varepsilon^*(\omega)$ in its dependence on frequency of the external electrical field comes from the atomic polarization and space charge polarization in the glass.

The dielectric spectroscopy can be used to investigate the dielectric relaxation processes and these dielectric relaxation processes are usually analyzed using model functions. Several functions for both the frequency and the time domain have been proposed to describe the experimentally observed dielectric spectra based on the distribution of relaxation time [25].

With a singe relaxation time of Debye relaxation time τ_D, the Debye function is given by [25]:

$$\varepsilon^*(\omega) = \varepsilon_\infty + \frac{\Delta\varepsilon}{1+i\omega\tau_D} \qquad \text{Equation 1-13}$$

Here $\Delta\varepsilon = \varepsilon_s - \varepsilon_\infty$ is dielectric relaxation strength with $\varepsilon_s = \lim_{\omega\tau<<1} \varepsilon'(\omega)$ and $\varepsilon_\infty = \lim_{\omega\tau>>1} \varepsilon'(\omega)$. The dielectric loss ε" spectrum is symmetric about a central frequency with a characteristic shape and width.

However in most cases more than one relaxation time is included in the dielectric relaxation process. This is called non-Debye relaxation behavior. Several empirical model functions, mostly extended from Debye function, have been developed and tested which can be used to describe the experimentally observed dielectric spectra.

The Cole/Cole function [26]:

$$\varepsilon^*_{CC}(\omega) = \varepsilon_\infty + \frac{\Delta\varepsilon}{1+(i\omega\tau_{CC})^\beta} \qquad \text{Equation 1-14}$$

Here $0 < \beta \leq 1$ and this function can used to describe the symmetrical broadening for the relaxation function. For β=1 the function becomes Debye function.

While for the Cole/Davidson function [27,28]:

$$\varepsilon^*_{CD}(\omega) = \varepsilon_\infty + \frac{\Delta\varepsilon}{(1+i\omega\tau_{CD})^\gamma} \qquad \text{Equation 1-15}$$

Here $0 < \gamma \leq 1$ and the use of parameter γ can describe the asymmetric broadening of the relaxation function. Also with γ=1, the Debye function is obtained.

More generally the Havriliak and Negami function (HN-function) is proposed [29,30]:

$$\varepsilon^*_{HN}(\omega) = \varepsilon_\infty + \frac{\Delta\varepsilon}{(1+(i\omega\tau_{HN})^\beta)^\gamma} \qquad \text{Equation 1-16}$$

This function is actually the combination of the Cole/Cole and Cole/Davidson functions.

The dielectric behavior in the frequency domain is related to that in time domain by a Fourier transform. The useful empirical function to describe the non-Debye relaxation process in time domain is the Kohlrausch/Williams/Watts (KWW) function [31,32]:

$$\varepsilon(t) - \varepsilon_\infty = \Delta\varepsilon\left[1 - \exp\left(\left(-\frac{t}{\tau_{KWW}}\right)\right)^{\beta_{KWW}}\right] \qquad \text{Equation 1-17}$$

1.3.2.2 Electrode polarization in glass

During the impedance spectroscopy measurements of samples, there exists the electrode polarization mainly in the moderately to highly conducting samples. The Figure 1-5 shows the electrode polarization effect on the impedance complex plane plot and frequency dependent dielectric spectra of $Li_{0.5}La_{0.5}TiO_3$ samples [33,34]. In the impedance complex plane plot the straight line at low frequency is thought to come from the electrode polarization. It is more obvious in the real part dielectric dependent of frequency spectrum, Figure 1-5.b. At low frequency the real part dielectric increase largely with the decreasing of the frequency and while as seen in figure, if without electrode polarization, the real part dielectric constant will be much lower than the experimental ones. Only electrode polarization can explain such sudden large increase of real part dielectric at low frequencies.

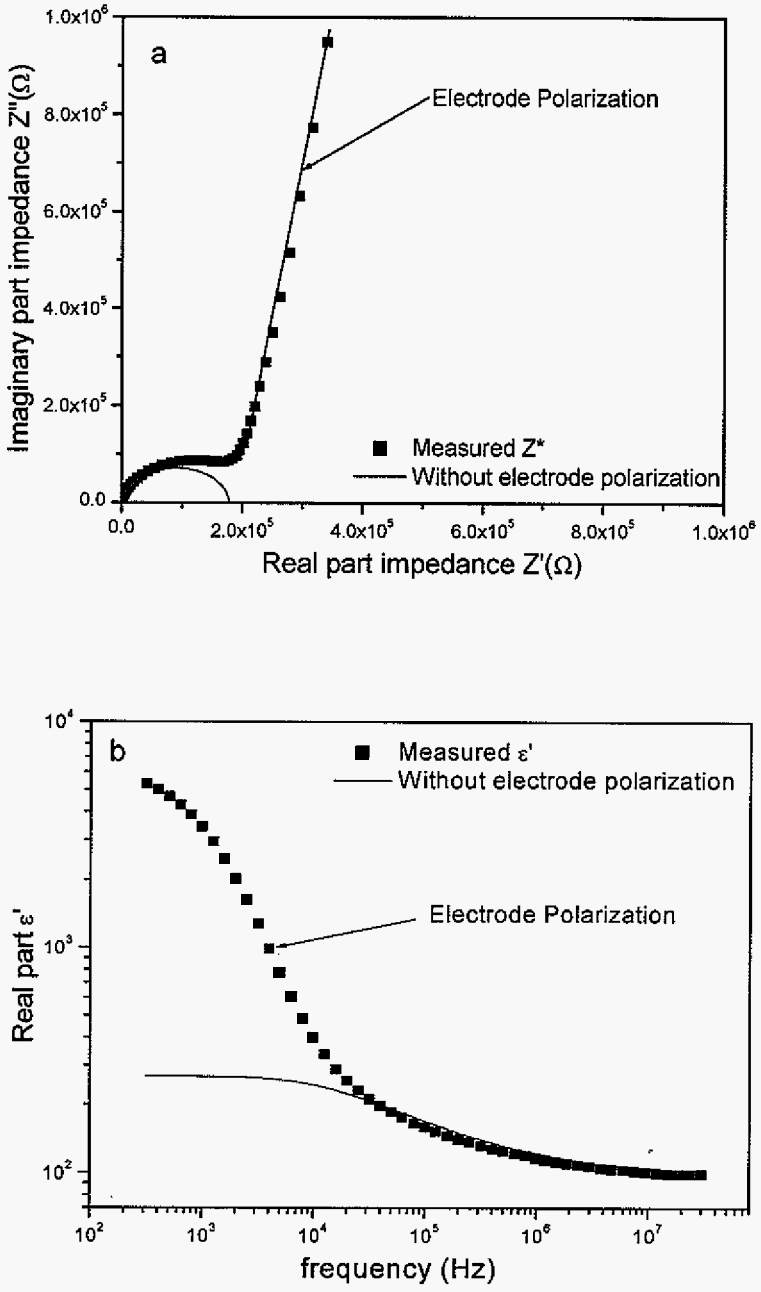

Figure 1- 5 The electrode polarization effect on the impedance complex plane plot and frequency dependent dielectric spectra of $Li_{0.5}La_{0.5}TiO_3$ samples

The electrode polarization is attributed to the blocking of charge carriers (space charges) at the sample/electrode interface. A simple model of diffuse double layer can describe the blocking carriers at the sample/electrode interface and the double layer behaves as a simple parallel plate capacitor. The space of double layer is the Debye length L_D [25, 34]. So the double layer leads to the large capacitance and it is in series to the studied sample. However in practical it is not enough to use the simple parallel plate capacitor to represent the electrode polarization. Actually the significant frequency dispersion is observed in the study of solid-solid interface by impedance spectroscopy. It is found by several authors that the constant-phase element (CPE) can empirically be used to describe this frequency dispersion at interface although there is no well-defined microscopic theory for CPE [35,36].

The equivalent circuit is the powerful tool in the study of impedance spectroscopy. The frequency response data for solid ionic conductor can be fitted satisfactorily by the equivalent circuit in Figure 1-6, which is O circuit from the LEVM program developed by Macdonald et al[34, 37]. This equivalent circuit is thought to fitful for solid state materials, conductive or dielectric system. The right part of circuit usually can fit the bulk properties of sample, such as bulk capacitance and bulk resistance, at high frequency part. And the left part of circuit can fit the data caused by electrode polarization at low frequency part. The appropriate parameters are chosen for conductive or dielectric system. Since the complication of the interface between sample/electrode and the electrode polarization, a series constant-phase element (SCPE) in parallel with C_3 and then in series with a capacitance can best represent the electrode polarization effect. Many impedance data for solid ionic materials have been fitted using the appropriate equivalent circuit by Macdonald [38,39,40, 41,42].

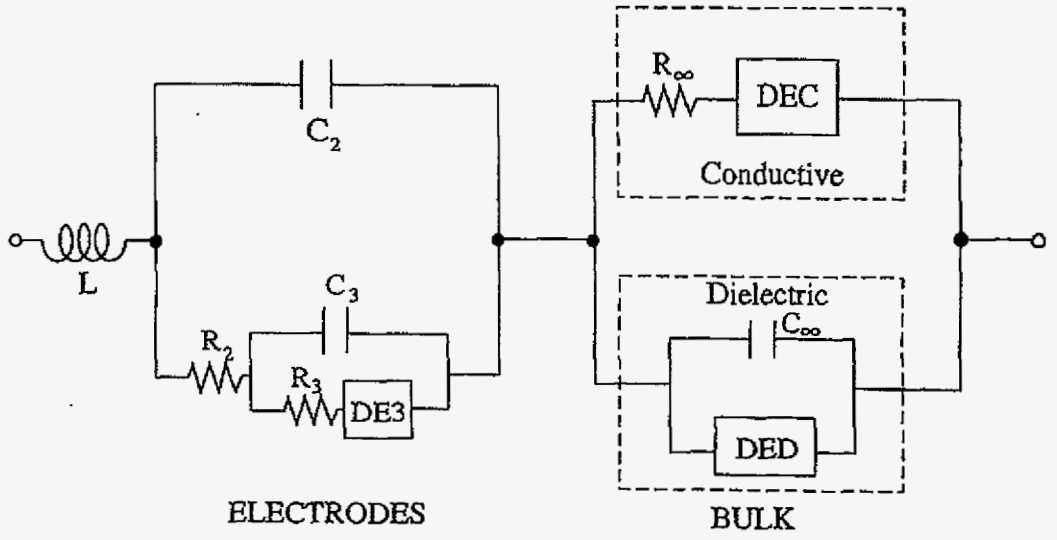

Figure 1-6 An equivalent circuit implemented in LEVM to fit the impedance spectroscopy data for solid state materials [34]

1.3.2.3 Determination of charge carrier density by space charge polarization

Many theories of space charge polarization have been proposed [43,44,45]. The model of Beaumont and Jacobs is often used since it can explain many of important experimentally observed features in glasses [45,46]. A comparatively simple expression for the real and imaginary parts, ε', and ε", of the frequency dependent dielectric constant due to space charge polarization can be derived from model of Beaumont and Jacobs :

$$\varepsilon'(\omega) = \varepsilon_\infty + \frac{2\varepsilon_\infty (D^2 K_1^3 / \omega^2 L)}{1 + (2+\rho)^2 (D^2 K_1^2 / \omega^2 L^2)} \qquad \text{Equation 1-18}$$

$$\varepsilon''(\omega) \approx \frac{\sigma_{dc}}{\omega \varepsilon_0} - \frac{2\varepsilon_\infty (D^3 K_1^4 / \omega^3 L^2)(2+\rho)}{1 + (2+\rho)^2 (D^2 K_1^2 / \omega^2 L^2)} \qquad \text{Equation 1-19}$$

Where ε_∞ is all the polarization contribution except the space charge polarization, ε_0 is the permittivity of free space, L is the thickness of sample, ω is the angular frequency, ρ is a dimension-less parameter representing the extent of the charge transfer at the sample-electrode interface. For a completely blocking electrode, $\rho = 0$, and for partially blocking electrode $\rho > 0$. D is the diffusion coefficient, given as

$$D(T) = \frac{\sigma_{dc}(T)kT}{n(T)e^2} \qquad \text{Equation 1-20}$$

n(T) is the charge carrier concentration dependent of temperature, K_1 is proportional to the reciprocal Debye length and is given by

$$K_1^2 = \frac{n(T)e^2}{kT\varepsilon_0\varepsilon_\infty} \qquad \text{Equation 1-21}$$

Substitute Equation 1-20 and Equation 1-21 into Equation 1-18, we can get:

$$\varepsilon'(\omega) = \varepsilon_\infty \left(1 + \frac{2\sigma_{dc}^2(T)\sqrt{\frac{kT}{n(T)e^2(\varepsilon_0\varepsilon_\infty)^3}}\left(\frac{1}{\omega^2 L}\right)}{1+(2+\rho)^2\left(\frac{\sigma_{dc}^2(T)kT}{n(T)e^2\varepsilon_0\varepsilon_\infty}\right)\frac{1}{\omega^2 L^2}} \right) \qquad \text{Equation 1-22}$$

At the low frequency limit ($\omega \rightarrow 0$), the real part dielectric constant affected by space charge polarization, Equation 1-18 and Equation 1-22 is given by:

$$\varepsilon_s = \varepsilon_\infty + \frac{2K_1 L\varepsilon_\infty}{(2+\rho)^2} = \varepsilon_\infty + \frac{2L\varepsilon_\infty}{(2+\rho)^2}\sqrt{\frac{n(T)e^2}{kT\varepsilon_0\varepsilon_\infty}} \qquad \text{Equation 1-23}$$

It should be noticed that this equation relates the dielectric constant at low frequency ε_s to the number density of charge carrier, n(T).

Using the above equations, Tomozawa et al. studied the sodium silica glasses with changes of temperature, composition, specimen thickness and surface condition [46,47, 48]. Some features of frequency dependent of dielectric constant of glass caused by space charge polarization can be explained by the model of Beaumont and Jacobs. Combine the Equation 1-23 with the experiment data of dielectric constant dependence of frequency, shown in Figure 1-7, the number of charge carrier of sodium silica glass can be determined, and the results are listed on Table 1-1. Pitarch et al studied the dielectric relaxation dependent of bias voltage for one silica glass and the charge number density also was determined based on the model of Beaumont and Jacobs by means of Mott-Schottky capacitance-voltage characteristics. The obtained charge carrier number density is lower by many orders of magnitude than the nominal alkali number density [49].

Table 1-1 Effect of temperature, fictive temperature, and water content of a sodium silica glass on its electrical properties

Sample	L (μm)	T (°C)	$\sigma_{d.c.}$ $(\Omega cm)^{-1}$	$\Delta\varepsilon_{space\ charge}$	n $(\#/m^3)$	n/n_0
As-received (T_f=1069°C)	90	200	3.5×10^{-13}	333	5.9×10^{19}	1
Heat-treated (T_f=1221°C)	99	200	1.0×10^{-13}	216	1.4×10^{20}	2.4
As-received (OH=5 ppm wt.)	90	160	2.1×10^{-14}	91.6	3.0×10^{18}	0.05
Hydrated (OH=762 ppm wt.)	162	160	2.1×10^{-15}	1.64	2.2×10^{14}	3.8×10^{-6}

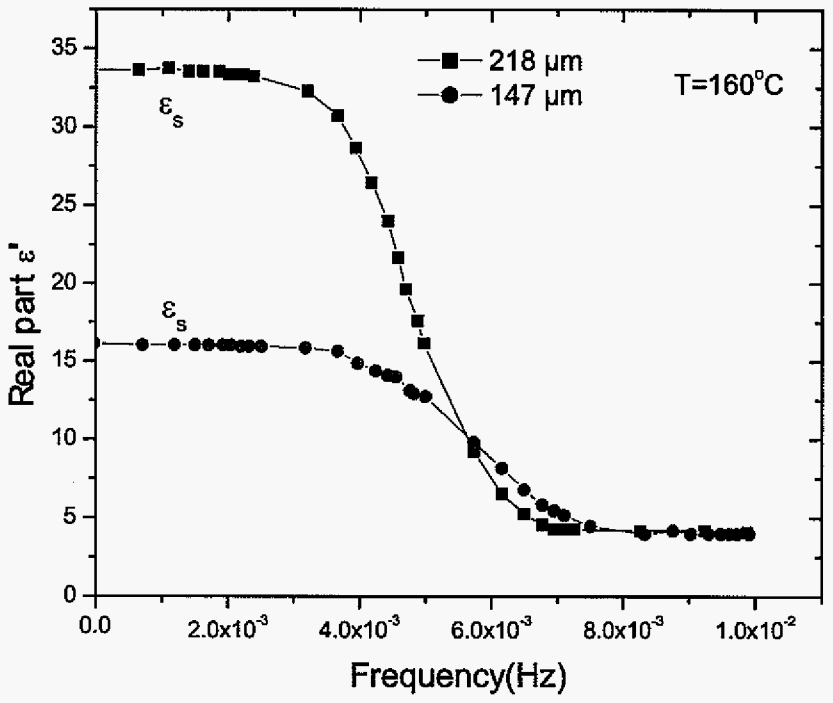

Figure 1-7 The variation of dielectric constant caused by space charge polarization in sodium silica glass

1.4 Proposed work

Up until now, all of the studies of determination of the number of charge carriers using the model of Beaumont and Jacobs have been limited to the low conductivity oxide glasses. Chalcogenide glasses usually have high ionic conductivities compared with oxide glasses. Previous studies of chalcogenide glasses, as shown in Figure 1-8 [50], show that in the low frequency region there is a polarization capacitance caused by a space charge region in the glass. So it is possible that we can determine the number density of charge carrier using space charge polarization measurement in the glass similar to oxide glass. To understand the reason of conductivity maximum limitation in the glass, one of the best way is to understand the behavior of n (T) as a functions of temperature, composition and structure and in this way these results might be used to overcome the conductivity maximum limitation, optimizing the

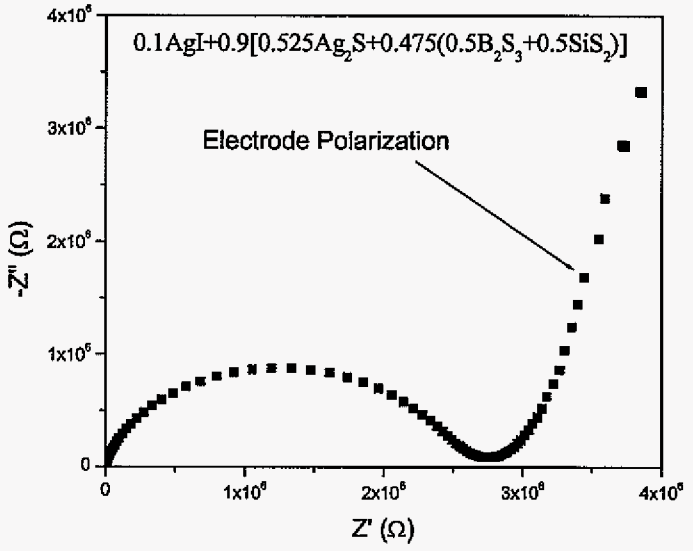

Figure 1-8 Complex impedance spectra of FIC chalcogenide glass [50]

electrical properties of glass.

In their studies of the oxide glass the Anderson and Stuart found that the binding energy ΔE_b was much larger than strain energy ΔE_s, and this result agrees with the weak-electrolyte behavior which means that the conductivity of glass is determined by the number density of charge carrier and hence binding energy ΔE_{act} is important. According to Anderson-Stuart model, the ionic radius plays an important role in determining the magnitude of binding energy. So a way to study the number density of charge carrier would be to study effect of different radius ions.

Using the model of Beaumont and Jacobs, the dielectric constant dependence on frequency and temperature was calculated considering the strong-electrolyte and weak-electrolyte unity behaviors, as shown in Figure 1-9. Figure 1-9(a) corresponds to the strong-electrolyte behaviors, where the number of charge carrier will not change with the temperature, so the low frequency limit of dielectric constant ε_s change little with the change of temperature according to the Equation 1-22. While for the weak-electrolyte behavior, where the number of charge carrier changes exponentially with the change of temperature, the dielectric constant dependence on frequency and temperature, Figure 1-9(b), differs largely from that of strong-electrolyte behavior, Figure 1-9(a). In the experiments proposed here, we expect to get similar plots to Figure 1-9. From these experiments, we can determine the number of charge carriers at different temperature from which we can determine the binding energy. In addition, different glass composition will be studied to determine if n(T) can be determined using space charge polarization method over a wide range of glass composition . Finally the number density of charge carriers as a function of temperature, composition and structure will be determined.

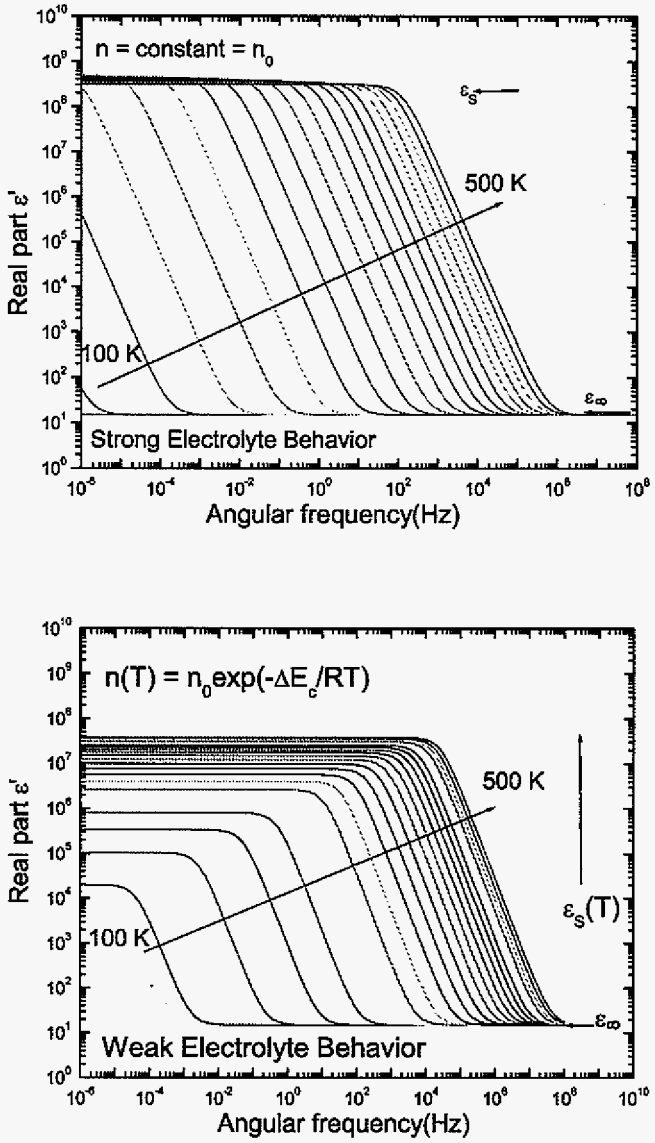

Figure 1-9 Calculated frequency dependence of ε' with Beaumont-Jacob model

1.4.1 Glass systems to be studied

The MI + M_2S + ($0.1Ga_2S_3$ + $0.9GeS_2$) (M=Li, Na, K and Cs) glasses system will be studied. It is known that germanium sulfide are strong glass formers over large composition ranges and the addition of Ga_2S_3 helps to improve the T_g and therefore provide a good glass matrix for different alkali and alkali iodide compositions. Since the columbic binding energy ΔE_b is important in governing the conductivity in the glass, and the Anderson-Stuart model relates the radius of cations and ions to the binding energy, a good way to investigate the behavior of ΔE_b is to decrease the alkali radius under the condition of approximately constant composition and structure. Alkali glasses will be used for this study because they have smaller ionic polarizability which is not accounted for in the simple treatment of the activation energy. Higher conducting Ag glasses have been suggested to have lower activation energies because of the increased polarizability of the Ag^+ cation compared to the less polarizability of alkali cation, such as Li^+.

1.4.2 Characterization measurements to be made

Impedance spectroscopy will be performed to measure the space charge polarization of studied glass compositions. The impedance spectroscopy data will be fitted through appropriate equivalent circuit. Through the dielectric constant data, the number density of charge carrier can be determined according to Beaumont-Jacobs model. Structure characterization of the glasses will be performed for the studied glass composition to correlate the structure and properties of glasses. IR and Raman spectroscopy are useful methods to study the structural units in glasses and will be used to study the change of the glass structure with alkali sulfide and alkali iodide in the glass composition. Neutron

scattering is also a powerful tool to investigate the local atomic structure in the glass and the atom-atom distances can be determined which will give us important information how the charge carrier can transport in the glasses.

1.5 References

[1] G. Warburg, Ann. Phys. und Chem. 21 (1884) 622.

[2] C. Julien, G-A. Nazri, Solid State Batteries: Materials Design and Optimization. Kluwer Academic Publishers 1994.

[3] T.Saito, N. Torata, M. Tatsumisago and T. Minami, Solid State Ionics 86-88 (1996) 491.

[4] T. Saito, M. Tarsumisago and T. Minami, Solid State Ionics 61 (1993) 285.

[5] M. D. Ingram, Physics and Chemistry of Glasses 28 (1987) 215.

[6] H. L. Tuller, D. P. Button, and D. R.Uhlmann, Journal of Non-Crystalline Solids 40 (1980) 93.

[7] S.W. Martin, C.A. Angell, Journal of Non-Crystalline Solids 83 (1986) 185.

[8] O.L. Anderson, D.A. Stuart, Journal of the American Ceramic Society 37 (1954) 574.

[9] D.P. Almond, G.K. Duncan, A.R. West, Solid State Ionics 8 (1983) 159.

[10] D.P. Almond, G.K. Duncan, A.R. West, Journal of Non-Crystalline Solids 74 (1985) 285.

[11] E. F. Hairetdinov, N. F. Uvarov, H. K. Patel, and S. W. Martin, Physical Review B: Condensed Matter 50 (18) , (1994) 13259.

[12] D. Ravaine, J.L. Souquet. Physics and chemistry of glasses 18 (1977) 27.

[13] D. Ravaine, J.L. Souquet. Physics and chemistry of glasses 19 (1977) 115.

[14] J. O. Isard, K. K. Mallick, Solid State Ionics 21 (1986) 7.

[15] S. R. Elliott, Journal of Non-Crystalline Solids 172-174 (Pt. 2) (1994) 1343.

[16] Y. S. Tver'yanovich, V. V. Aleksandrov, I. V. Murin, and E. G. Nedoshovenko, Journal of Non-Crystalline Solids 256&257 (1999) 237.

[17] P.Balaya, V.K.Shrikhande, G.P.Kothiyal, and P.S Goyal, Current Science 86 (4) (2004) 553.

[18] M.M. Ryan, S. I. Smedley, Journal of Non-Crystalline Solids 65 (1984) 29.

[19] A. Kone, J.L. Souquet, Solid State Ionics 18-19 (1986) 454.

[20] J.C. Reggiani, J. P. Malugani, J. Bernard, Journal of Chemical Physics 75 (1978) 254

[21] M. Tomozawa, J.F Cordaro, M. Singh, Journal of Non-Crystalline Solids 40 (1980) 189.

[22] M. D. Ingram, C. T. Moynihan, and A. V. Lesikar, Journal of Non-Crystalline Solids 38-39 (1) (1980) 371.

[23] A. Kone, J.C.Reggiani, J. L. Souquet, Solid State Ionics 9-10 (1983) 709.

[24] L. Liu, Solid State Ionics 85 (1996) 25.

[25] F. Kremer and A. Schonhals, Broadband Dielectric Spectroscopy, Springer (2003).

[26] K. S. Cole, R. H. Cole, Journal of Chemical Physics 9 (1941) 341.

[27] D.W. Davidson, R.H. Cole, Journal of Chemical Physics 18 (1950) 1417.

[28] D.W. Davidson, R.H. Cole, Journal of Chemical Physics 19 (1951) 1484.

[29] S. Havriliak, S. Negami, Journal of Polymer Science C 16 (1966) 99.

[30] S. Havriliak, S. Negami, Polymer 8 (1967) 161.

[31] R. Kohlrausch, Annals of Physics 12 (1847) 393.

[32] G. Williams, D.C Watts, Journal of the Chemical Society, Faraday Transactions 2 68 (1970) 1045.

[33] C. Leon, J. Santamaria, M.A. Paris, J. Sanz, J. Ibarra, and A. Varez, Journal of Non-Crystalline Solids 235-237 (1998) 753.

[34] E. Barsoukov and J.R. Macdonald, Impedance Spectroscopy:theory, experiment, and applications, John Wiley & Sons, Inc (2005).

[35] P.H. Bottleberghs, G.H. J. Broers, Journal of Electroanalytical Chemistry 67 (1976) 155.

[36] I. D. Raistrick, C. Ho, Y. –W. Hu, R. A. Huggins, Journal of Electroanalytical Chemistry 77 (1977) 319.

[37] J.R. Macdonald, Journal of Non-Crystalline Solids 197 (1996) 83.

[38] J.R. Macdonald, Journal of Non-Crystaline Solids 212 (1997) 95.

[39] J.R. Macdonald, Journal of Non-Crystaline Solids 210 (1997) 70.

[40] J.R. Macdonald, Journal of Chemical Physics 116 (8) (2002) 3401.

[41] J.R. Macdonald, Journal of Non-Crystaline Solids 307-310 (2002) 913.

[42] J.R. Macdonald, Journal of Physics: Condensed Matter 17 (2005) 4369.

[43] J.R. Macdonald, The Journal of Chemical Physics , 58 (11) (1973) 4982.

[44] J.R. Macdonald, The Journal of Chemical Physics 29 (6) (1958) 1346.

[45] J. M. Beaumont, and P. W. Jacobs, Journal of Physics and Chemistry of Solids 28 (1967) 657.

[46] C. Kim, and M. Tomozawa, Journal of the American Ceramic Society 59 (3-4) (1976) 127.

[47] D.W.Shin, M.Tomozawa, Journal of Non-Crystalline Solids 211 (1997) 237.

[48] M.Tomozawa, D.W.Shin, Journal of Non-Crystalline Solids 241 (1998) 140.

[49] A.Pitarch, J.Bisquert, and G.Garcia-Belmonte, Journal of Non-Crystalline Solids 324 (1-2) (2003) 196.

[50] J. Schrooten , Ph.D. thesis, Iowa State University (2001).

2. Structure and Properties of MI + M_2S + ($0.1Ga_2S_3 + 0.9GeS_2$) (M=Li, Na, K and Cs) Glasses System

A paper to be submitted to Journal of Non-Crystalline Solids

Wenlong Yao[1], Kyle Berg[1], Steve Martin[1,2]

Abstract:

The structure and properties of MI + M_2S + ($0.1Ga_2S_3 + 0.9GeS_2$) (M=Li, Na, K and Cs) glasses system were studied using Raman, and IR spectroscopy, and T_g and density measurements to help to understand the ionic transport in these glasses. The glass forming ranges of these ternary glasses were compared to those of the binary alkali sulfide and germanium di-sulfide systems. The more extensive glass forming range of Na_2S system were used to show the more extensive changes of structure and properties of these glasses as a function of Na_2S. As expected, non-bridging sulfurs (NBS) form with the addition of alkali sulfide. Unlike their oxide counterparts, however, the alkali sulfide doped glasses appear to support longer range super-structural units. For example, the adamantine-like $Ge_4S_{10}^{4-}$ structure exists in the K_2S and Cs_2S glasses. The structural role of the alkali iodide addition was also explored since the addition of alkali iodide helps to improve the conductivity. For most of these glasses, as observed in many other oxide glasses, the added MI dissolves interstitially into glass structure network without changing the alkali sulfide network structure. In $0.6Na_2S + 0.4(0.1Ga_2S_3 + 0.9GeS_2)$ glasses, however, the added NaI may enter

[1] Department of Materials Science & Engineering, Iowa State University, Ames, IA 50011
[2] Author to whom correspondence should be directed

the glass structure as it causes systematic changes in the frequency of the Ge-S network mode as seen in Raman spectroscopy.

2.1 Introduction

Fast ion conducting (FIC) sulfide glasses have higher ionic conductivities than their oxide counterparts and for this reason are potential solid state electrolytes in high energy density, high performance batteries. Such glasses are isotropic, lack grain boundaries, are easily fabricated into complex shapes and have wide compositional flexibility that can be used to optimize the properties. The structure and properties of these glasses are important to the understanding of their ionic transport. Because alkali ions (especially Li^+ and Na^+) become mobile when doped into these glasses, many structural studies of systematically doped oxide glasses have been reported [1,2].

Fewer studies of the heavy alkali (K, Rb, and Cs) sulfide doped glasses have been done due to the difficulty of obtaining the high purity alkali sulfide and their lack of high conductivity. J. Cho, however, systematically studied the alkali sulfide and boron sulfide binary system [3]. Here Cho produced the alkali sulfide through the direct reaction of alkali metal (K, Rb, and Cs) and sulfur in sealed silica ampoule to attain the high purity alkali sulfide. This reaction, however, is a dangerous and expensive method. While B_2S_3-based glasses have been extensively studied by our group, B_2S_3 is difficult to prepare and also rapidly reacts with oxygen and water and this always produces same level of oxygen in the prepared glasses. GeS_2-based glasses, on the other hand, are more stable and less prone to react with oxygen and water, even in a high alkali content glass. For this reason, the binary systems of $Li_2S + GeS_2$, $Na_2S + GeS_2$, and $Ag_2S + GeS_2$ have been studied by different

groups [4-6] It is found that $Na_2S + GeS_2$ have the largest glass forming region from 0 to 0.6 mole fraction of Na_2S, while both $Li_2S + GeS_2$ and $Ag_2S + GeS_2$ have glass forming regions from 0 to 0.5 mole fraction. Recently the heavy alkali binary systems of $M_2S + GeS_2$ (M = K, Cs, Rb) have been investigated for the first time and involved a novel alkali sulfide preparation route [7]. The $M_2S + GeS_2$ (M = K, Cs, Rb) systems were found to have limited glass forming ranges between 0 to 0.2 mole fraction.

The basic structural unit in GeS_2 glass is the $GeS_{4/2}$ tetrahedral. In the Raman spectrum of pure GeS_2, the peak at 342 cm^{-1} is assigned to symmetrical stretching vibration of the $GeS_{4/2}$ tetrahedral [4]. A strong shoulder at 375 cm^{-1} is assigned to the vibration of two edge-shared tetrahedrals and the 435 cm^{-1} band is due to the vibration of two corner-shared tetrahedrals. The medium-range structure of GeS_2 is thought to consist of the chains of corner-shared $GeS_{4/2}$ tetrahedral units and with edge-shared $GeS_{4/2}$ tetrahedral in the chains to form a layered structure [8]. With the progressive addition of Li_2S into GeS_2, three new peaks appear at 454, 415 and 385 cm^{-1} and are attributed to $GeS_{4/2}$ tetrahedral unit with one, two and three non-bridging sulfurs (NBS) and with structure $MSGeS_{3/2}$, $(MS)_2GeS_{2/2}$, and $(MS)_3GeS_{1/2}$, respectively, as shown in Figure 2-1 [9]. Correspondingly, all of these three peaks are observed in the $Na_2S + GeS_2$, $Ag_2S + GeS_2$ and $Li_2S + B_2S_3 + GeS_2$ glasses with minor shifts due to the compositional differences in these glasses [4,5,10]. With the addition of Ga_2S_3 into GeS_2, the glasses still contain both corner-sharing (435 cm^{-1}) and edge-sharing (370 cm^{-1}) tetrahedral structures and $GaS_{4/2}$ tetrahedral unit forms [11].

In our previous work, glass formation in the $LiI + Li_2S + GeS_2 + Ga_2S_3$ system was studied to optimize their properties for use in solid-state lithium batteries [12]. GeS_2 was chosen as a good glass former, and Ga_2S_3 was added to act as a glass intermediate to extend

the glass forming range by eliminating non-bridging sulfur and to increase the ionic conductivity and glass transition temperature T_g. In this paper, the strategy was to choose the $0.1Ga_2S_3 + 0.9GeS_2$ as the basic glass forming composition because it was found to have the most extensive glass forming range for all of the alkali sulfides, and the different alkali (Li, Na, K and Cs) sulfide were systematically added into $0.1Ga_2S_3 + 0.9GeS_2$ glass system. The Raman and IR spectroscopy were used to study the structure change with extensive composition change and two important properties of these glasses, the density and T_g, are also examined. In doing so, the understanding of structure of glasses will help to understand the ion transport behavior in these glasses due to different ions and glass structure.

2.2 Experimental methods

2.2.1 Preparation of the glass

All glass batching and melting operations were carried out in an oxygen- and water-free (<5ppm) glove-box. High purity glassy GeS_2 was synthesized by the reaction of elemental germanium metal (Cerac, 99.999%) and sulfur (Alfa Aesar 99.999%) at high temperature (900 °C) in an evacuated silica ampoule [3]. Since high purity M_2S (M = Na, K and Cs) are not commercially available, the high purity MSH (M = Na, K and Cs) were prepared by the reaction of MOH (M = Na, K and Cs) and high pressure H_2S gas using a method developed by Poling [13]. To obtain large amount of high purity products, the MOH first was dissolved in methanol and de-ionized water and reacted with H_2S by bubbling H_2S through solution [14]. The obtained dried product, which was not completely reacted with H_2S, was placed in a stainless steel reactor to react completely with high pressure H_2S liquid. The obtained high purity NaSH was put into an alumina tube and the tube is sealed in the stainless steel

container. The container was placed in the vertical furnace connected to a vacuum pump and the furnace temperature was increased to 600 °C, the NaSH slowly decomposed into Na_2S and H_2S gas. The Na_2S in the alumina tube was calculated and the weight loss of 30.28% was comparable to theoretical weight loss of 32.19%. From the Mid-IR spectrum of the Na_2S product, the as prepared Na_2S was found to have a higher purity than that of commercial Na_2S. For K and Cs, the KSH and CsSH were used directly without this pre-decomposition reaction and were decomposed into M_2S and H_2S gas at high temperature during the preparation of the glasses. The glasses samples show no existence of -SH peaks in Raman and IR spectroscopy.

The MI + M_2S + ($0.1Ga_2S_3 + 0.9GeS_2$) (M=Li, Na, K and Cs) glasses were prepared by melting stoichiometric amounts of Ga_2S_3 (Alfa 99.99%), GeS_2, MI (LiI, Cerac 99%, NaI, Alfa 99.9%, KI, Alfa 99.9%, CsI, Aldrich 99.9%) and M_2S(Li_2S, Alfa 99.9%, Na_2S) or MSH (KSH, CsSH) between 870 °C and 920 °C for 6 mins in covered vitreous carbon crucibles inside a high quality glovebox. The melts were quenched in a brass mold at room temperature. Weight loss measurements were done by removing carbon crucible from the furnace after 3 mins melting and all weight losses due to evaporation were generally less than 5 wt.%.

2.2.2 Density measurement

The Archimedes method was used inside the glove box to determine the bulk sample densities using kerosene as the suspending liquid. The dry mass of the sample was first recorded and then the sample was submersed in liquid kerosene and the suspended mass was measured. Three different pieces of the same composition were measured individually and

the average density value was obtained. The error in the density measurements were estimated by the largest difference between average value and the largest or smallest values measured.

2.2.3 Differential scanning calorimetry (DSC)

Glass transition and crystallization temperatures were measured using a Perkin Elmer Pyris Diamond Differential Scanning Calorimeter (DSC). ~15 mg of powder sample was hermetically sealed in an aluminum pan in the oxygen- and water-free (< 5ppm) glove-box. Most samples were heated at a rate of 10 °C / min from 50 °C to 450 °C under a nitrogen gas purge of 20 cm^3 / min.

2.2.4 Far-IR spectroscopy

The far-infrared absorption spectra were obtained in the range of 550-150 cm^{-1} with the use of a Bruker IFS 66v/s spectrometer using 32 scans and 4 cm^{-1} resolution. Three mgs of each sample and 100 mgs CsI were mixed, grounded into fine powder and pressed into pellets for the transmission measurements.

2.2.5 Raman spectroscopy

A Renishaw inVia spectrometer was used to collect the Raman spectra using the 488 nm line of the Ar^+ laser at 25 mW power. Small bulk samples, which were placed into a small cup-like sample holder and covered with clear amorphous tape to not expose the sample to air, were directly focused through the tape to obtain good quality spectra.

2.3 Results

2.3.1 Glass forming ranges

As discussed above, the $0.1Ga_2S_3 + 0.9GeS_2$ system was chosen as the base glass former system because it was found to yield glasses over reasonable ranges of alkali sulfide content for all of the alkali sulfides. The highest alkali sulfide content glasses are preferred because we seek the highest conductivity in this system and we also found that high alkali content glasses (low GeS_2 contents) decrease the evaporation of GeS_2 during the melting of materials and yield more compositionally correct glasses. We report the glass forming range, properties and structure of the alkali (Li, Na, K and Cs) sulfide and iodide doped glasses and all compositions are listed in Table 2-1.

From the compositions in Table 2-1, it is seen that different glass forming abilities are observed for the different alkali sulfides. The Li and Na compositions have good glass forming ranges, while for K and Cs, the glass forming range is limited. With the addition of 10% Ga_2S_3, the Na_2S glass forming ranges extends to $x = 0.67$ and this compares to $x = 0.6$ in the $Na_2S + GeS_2$ binary glass system. Likewise for the K_2S and Cs_2S system, the glass forming ranges extend to $x = 0.4$ compared to $x = 0.2$ in their GeS_2 binary system. Although low mole fractions of alkali sulfide compositions were not explored in this study, it is expected that they should also yield glasses according to studies of the previous binary systems [7].

2.3.2 Raman spectroscopy

In the Raman spectra of binary $Li_2S + GeS_2$, the peaks at 454, 415, 385 and 340 cm^{-1} have been assigned to a $GeS_{4/2}$ tetrahedral with one, two, three non-bridging sulfurs (NBS)

and the all-bridging sulfur unit $GeS_{4/2}$, respectively[9]. Figure 2-2 shows the Raman spectra of $xLi_2S + (1-x)(0.1Ga_2S_3 + 0.9GeS_2)$ glasses. All three composition glasses show the bridging sulfur peak at 345 cm^{-1}, and the one non-bridging sulfur peak at 460 cm^{-1}. With the increase of Li_2S, the peak due to two non-bridging sulfurs at 410 cm^{-1} begins to appear and its intensity increases. For the x = 0.5 glass, the 410 cm^{-1} peak is more pronounced than that of 460 cm^{-1} peak and this suggests that in this composition there are $GeS_{4/2}$ tetrahedral with two non-bridging sulfurs structures and the bridging sulfur units. It appears that the structure units with three non-bridging sulfurs do not form in these glasses.

Similarly, the Raman spectra of $xNa_2S + (1-x)(0.1Ga_2S_3 + 0.9GeS_2)$ glasses are shown in Figure 2-3. These glasses have a wide glass forming range and the compositional dependence of the spectra is strong and for this reason, as expected, the compositional change of the structure is expected to be stronger than that of other alkali sulfide glass. For the x = 0.4 glass, in addition to the bridging sulfur $GeS_{4/2}$ tetrahedral peak at 331 cm^{-1}, all three peaks at 451, 413 and 382 cm^{-1}, related to GeS_4 tetrahedral with one, two and three non-bridging sulfurs are observed. In contrast to the Li_2S glass, all four structure units exist in the Na_2S glasses at the same composition. With the increase of Na_2S, the bridging sulfur $GeS_{4/2}$ tetrahedral peak intensity slowly decreases until it disappears (as expected) at x = 0.67. For the Ge-S tetrahedral units with non-bridging sulfurs, the structural units change from one to two to three non-bridging sulfur with the increasing Na_2S. Finally at x = 0.67, the $GeS_{4/2}$ tetrahedral with four non-bridging sulfur peak appears at 372 cm^{-1} as expected in the glasses.

The effect of alkali iodide on the glass structure was studied through the Raman spectra of glasses and these are given in Figure 2-4. At the top of figure are the Raman spectra of the

$0.3Na_2S + 0.7(0.1Ga_2S_3 + 0.9GeS_2)$ glasses doped with NaI. As observed in other similar systems [15], there is no significant change due to the addition of NaI. The same trend appears in all of the Li_2S, K_2S and Cs_2S glasses with the addition of alkali iodide. For the $0.6Na_2S + 0.4(0.1Ga_2S_3 + 0.9GeS_2)$ glasses however, the peak at 385 cm^{-1} was splits into two peaks, one at 375 and one at 390 cm^{-1} with the addition of NaI and this suggests that a new structural unit appears with the addition of NaI in these glasses.

The Raman spectra of $xM_2S + (1-x)(0.1Ga_2S_3 + 0.9GeS_2)$ glasses with different alkali composition (M = Li, Na, K and Cs, x = 0.3, 0.4) are compared in Figure 2-5. The addition of the different alkali sulfides gives rise to the different peaks in the Raman spectra, while the $GeS_{4/2}$ tetrahedral structure with four bridging sulfurs peak appears in all compositions. The intensity of the peaks arising from units with non-bridging sulfurs increases with the increase of alkali radius. One obvious change is that there is a new peak at ~191 cm^{-1} in K_2S and Cs_2S glasses. This peak is attributed to the symmetric Ge-S-Ge bridge-bending mode due to the creation of $Ge_4S_{10}^{4-}$ adamantine-like structures, shown in Figure 2-1 [7].

2.3.3 Far-IR spectroscopy

The Far-IR spectra of $xLi_2S + (1-x)\ (0.1Ga_2S_3 + 0.9GeS_2)$ glasses are shown in Figure 2-6. The strong peak at 380 cm^{-1} is assigned to the $GeS_{4/2}$ tetrahedral structure with four bridging sulfurs and the peak at 450 cm^{-1} is assigned to the formation of non-bridging sulfurs. In the x = 0.5 glass, a new peak at 405 cm^{-1} appears and is assigned to the formation of other non-bridging sulfurs. Hence, the number of non-bridging sulfurs on the $GeS_{4/2}$ tetrahedral units changes with the addition Li_2S, similar to the result found in the Raman spectra of the same glasses. A similar trend is also seen in the Far-IR spectra of $xNa_2S+ (1-x)\ (0.1Ga_2S_3 +$

$0.9GeS_2$) glasses, Figure 2-7, which has a more extensive composition range as discussed above. The intensity of the IR peak arising from the $GeS_{4/2}$ tetrahedral structure with four bridging sulfurs decreases with the addition of Na_2S due to the formation of more non-bridging sulfurs. Also, the GeS_4 tetrahedral structures with increasing numbers of non-bridging sulfurs are formed with the increasing fraction of added Na_2S, as shown in the Figure 2-7 with change in the peak position. Finally, at the limit of the glass forming range one peak is observed in the spectrum as expected from the Raman spectra and this peak is attributed to the $GeS_{4/2}$ tetrahedral structure with four non-bridging sulfurs.

Figure 2-8 shows the effect of alkali iodide on the Far-IR spectra of the glasses. The spectra of $xNa_2S + (1-x)(0.1Ga_2S_3 + 0.9GeS_2)$, x = 0.3 and 0.6 glasses are shown. Different from the Raman spectra of the M_2S-doped glasses, there is no significant effect on the Far-IR spectra with the addition of alkali iodide. All of Far-IR spectra are unchanged with the addition of alkali iodide, as shown in Figure 2-8. Figure 2-9 shows the Far-IR spectra of the $xM_2S + (1-x)\ (0.1Ga_2S_3 + 0.9GeS_2)$ glasses with the addition of 30% alkali sulfide. The $GeS_{4/2}$ tetrahedral with four bridging sulfur peak and the non-bridging sulfur peak appear in all compositions, and there are some peaks in K_2S and Cs_2S composition glasses which are attributed to the formation of $Ge_4S_{10}^{4-}$ structure unit.

2.3.4 T_g, T_c and density measurements

The glass transition temperature (T_g), crystallization temperature (T_c) and density of bulk glasses for all samples were measured using DSC and through Archimedes method, respectively. Table 2- 2 lists the T_g and T_c and density values of selected glasses. In the $0.1Ga_2S_3 + 0.9GeS_2$ system, the same fraction of alkali sulfide (30% of alkali sulfide) show

different T_g and T_c values and the difference between T_g and T_c shows varying glass-forming ability with the different alkali sulfide additions. Usually, the addition of alkali iodide leads to a decrease of T_g because of the larger radius of iodide I^- which dilates the glass structure. In the density data, the density decreases with the increase of mass and radius of alkali ion from Li to K. Due to the larger mass of Cs, the density Cs_2S composition glasses is larger than those for the other alkali composition glasses. Table 2- **2** also gives the T_g and T_c and density of series of $xNa_2S + (1-x)(0.1Ga_2S_3 + 0.9GeS_2)$ glasses. The T_g decreases with the increase of Na_2S. The main reason is that Na_2S works as glass modifier to increases the formation of non-bridging sulfurs and break the glass structure network. The density decreases with the increase of Na_2S content because of the break of the tetrahedral units due to the formation of non-bridging sulfurs units and leads to the loose glass structure network. However at x=0.67, the T_g increases and it may attribute to the formation of four non-bridging sulfur structure unit.

2.4 Discussion

The structure of GeS_2 glass has been extensively studied and its structure is similar to that of GeS_2 crystal [16,17]. It is thought that in the glass the basic structural unit is the $GeS_{4/2}$ tetrahedral unit. In the intermediate range structure, the $GeS_{4/2}$ units form chains by sharing corners and the chains are connected through edge-sharing of $GeS_{4/2}$ units. The compositional change of the short range structural units in the glass is our primary study. The strongest peak at 340 cm^{-1} in Raman spectra is attributed to the symmetrical stretching vibration of $GeS_{4/2}$ tetrahedral with 4 bridging sulfurs. When Ga_2S_3 is added into GeS_2, the width of 340 cm^{-1} in Raman spectra increases because of the formation of $GaS_{4/2}$ tetrahedral

units whose symmetrical stretching vibration appears at 350 cm^{-1}[11]. In the $0.1Ga_2S_3$ + $0.9GeS_2$ glass forming system, part of $GaS_{4/2}$ tetrahedral exists, but the dominating structure unit is $GeS_{4/2}$ tetrahedral unit with bridging sulfurs.

The alkali sulfide, working as glass modifier, will enter the glass structure network and change the glass basic structure unit. When Li_2S is added into the $0.1Ga_2S_3$ + $0.9GeS_2$ system, a new peak appears because of the formation of $GeS_{4/2}$ tetrahedrals with non-bridging sulfurs as shown in Figure 2-2. The change of intensity of the peaks at 454 and 415 cm^{-1} in the Raman spectra and 450 cm^{-1} in the Far-IR spectra indicates that $GeS_{4/2}$ tetrahedrals with one non-bridging sulfur forms first with the addition of Li_2S and then with more added Li_2S, the number of one non-bridging sulfur decreases and at the same time the two non-bridging sulfur units forms. The addition of Li_2S helps to break the $GeS_{4/2}$ tetrahedral network connections through corner and edge sharing. The added alkali sulfide will cause the formation of $GaS_{4/2}$ tetrahedral unit just as $AlO_{4/2}$ units form in alkali alumina-silica glass [18].

The wide Na_2S content glasses have been studied and for this reason it is easier to follow the structural evolution in $xNa_2S + (1-x)(0.1Ga_2S_3 + 0.9GeS_2)$ glasses through Raman and Far-IR spectra. Different numbers of non-bridging sulfurs are formed with the increase of Na_2S. At low Na_2S contents (x = 0.2 and 0.3), the one non-bridging sulfur unit first forms, similar to the Li_2S compositions. Two and three non-bridging sulfurs units begin to appear with the increase of Na_2S. At median Na_2S contents (x = 0.4 and 0.5), the all bridging sulfur unit and three types of non-bridging sulfur exist at the same time in the glasses. The more Na_2S is added, the more non-bridging sulfur units form. Finally, the four non-bridging sulfurs structure units exist in the glass structure with none of the bridging sulfurs in high Na_2S

content (x = 0.67) glasses. The $Na_4Ge_4S_{10}$ ($0.33Na_2S+0.67GeS_2$) crystal had been studied and it is found that the adamantine-like $Ge_4S_{10}^{4-}$ structure exist in this crystal [5]. The Raman spectrum of $Na_4Ge_4S_{10}$ poly-crystal shows a peak at 200 cm^{-1} arising from the symmetrical bridge bending in $Ge_4S_{10}^{4-}$ structure. In our study, there is no strong peak at ~200 cm^{-1} in Raman spectra and this suggests that not many $Ge_4S_{10}^{4-}$ structural units may form in the glasses.

In the $xM_2S + (1-x)(0.1Ga_2S_3 + 0.9GeS_2)$, M = K, Cs and x= 0.3 and 0.4 composition glass, the peak at ~200 cm^{-1} appears in Raman spectra indicating the formation of $Ge_4S_{10}^{4-}$ structure unit in the glass. There is no such peak in the Raman spectra of $xM_2S + (1-x)GeS_2$(M = K, Cs and $0 \leq x \leq 0.2$) glasses [7]. With further addition of K_2S and Cs_2S(x = 0.27, 0.33), the composition is not glass forming anymore and the poly-crystal is preferred to form. The peak at ~200 cm^{-1} appears in the Raman spectra of these poly-crystals. All $M_4Ge_4S_{10}$ ($0.33M_2S + 0.67GeS_2$, M = Na, K and Cs) crystals show the existence of $Ge_4S_{10}^{4-}$ structure unit in the study of the crystal structure [19-21]. Different from K_2S and Cs_2S, the Na_2S composition glass doesn't show the peak at ~200 cm^{-1} in the Raman spectra although there is existence of $Ge_4S_{10}^{4-}$ structure in $Na_4Ge_4S_{10}$ ($0.33Na_2S + 0.67GeS_2$) crystal. From a literature search, there is no reference for the $Li_4Ge_4S_{10}$ crystal structure. It is expected that the radius of alkali ion plays an important role in the formation of this structural unit in the glass. It is not surprising to find that there are changes in the Raman spectra of $xM_2S + (1-x)(0.1Ga_2S_3 + 0.9GeS_2)$, M = Na, K, Cs, composition glass from x= 0.3 to x= 0.4 because the ratio of alkali/Ge reaches one over this compositional range.

The addition of alkali iodide helps to improve the glass' conductivity so the effect of alkali iodide on the glass structure has been studied using Raman and Far-IR spectroscopy.

The alkali iodide is usually thought to enter the interstitial structure in the glass network [15]. So there appears to be little change in the glass structure due to the addition of alkali iodide. This is true for most of our glass samples because there is no obvious change in the Raman and Far-IR spectra with the addition of alkali iodide. That suggests that the glass structure network changes very little since the alkali iodide only enters into the interstitials in the glass network. Saienga found that the ionic conductivity of the glasses reaches a maximum value with the addition of LiI greater than 50% [12]. A possible reason for this is that the LiI may not enter the interstitials any more after 50% instead of entering into the glass structure network and changing the glass structure. A similar trend is also found in the present system. Different from all other glass compositions, the addition of NaI into $0.6Na_2S + 0.4(0.1Ga_2S_3 + 0.9GeS_2)$ glasses shows obvious changes in the Raman spectra. The peak assigned to three non-bridging sulfurs at 385 cm^{-1} split into two peaks with the increase of NaI. It suggests that NaI has entered the glass structure network and caused the change of glass structure. It is possible that the $GeS_{4/2}$ tetrahedral with three non-bridging sulfurs appears. The interstitials in the glass structure network may not be big enough to accommodate the large I^- anion in the high alkali sulfide composition glass.

2.5 Conclusions

Raman and Far-IR spectroscopy have been performed on a series of $MI + M_2S + (0.1Ga_2S_3 + 0.9GeS_2)$ (M = Li, Na, K and Cs) glasses. The addition of alkali sulfide into $0.1Ga_2S_3 + 0.9GeS_2$ leads to the formation of non-bridging sulfur in the glass structure. The extensive range of Na_2S composition in $0.1Ga_2S_3 + 0.9GeS_2$ system shows the strong composition dependence of structure in the glasses. While the $Na_4Ge_4S_{10}$ ($0.33Na_2S +$

$0.67GeS_2$) crystal is known, the peak assigned to adamantine-like $Ge_4S_{10}^{4-}$ structure doesn't appear in the Raman and Far-IR spectra of Na_2S glasses. In K_2S and Cs_2S composition, the peak at ~200 cm^{-1} in Raman spectrum indicates the existence of adamantine-like $Ge_4S_{10}^{4-}$ structure. The effect of alkali iodide on the glass structure has been studied. Different from other glass, the three non-bridging sulfur peak at 385 cm^{-1} in the Raman spectra of $0.6Na_2S + 0.4(0.1Ga_2S_3 + 0.9GeS_2)$ glasses split into two peaks with the addition of NaI. It suggests that NaI enters the glass structure instead of entering the interstitials in the glass structure network, like other samples.

2.6 Acknowledgements

This work is supported by National Science Foundation grant # DMR-0610813.

2.7 Captions

Figure 2-1 Structure units in the studied glass: all bridging sulfurs $GeS_{4/2}$ tetrahedral unit, $GeS_{4/2}$ tetrahedral unit with non-bridging sulfur and $Ge_4S_{10}^{4-}$ structure unit

Figure 2-2 Raman spectra of $xLi_2S + (1-x)(0.1Ga_2S_3 + 0.9GeS_2)$ glasses, x = 0.3,0.4 and 0.5

Figure 2-3 Raman spectra of $xNa_2S + (1-x)(0.1Ga_2S_3 + 0.9GeS_2)$ glasses, x = 0.2,0.3,0.4 , 0.5,0.6 and 0.667

Figure 2-4 Effect of NaI on Raman spectra of $xNa_2S + (1-x)(0.1Ga_2S_3 + 0.9GeS_2)$ glasses, x = 0.3 and 0.6

Figure 2-5 Raman spectra of $xM_2S + (1-x)\ (0.1Ga_2S_3 + 0.9GeS_2)$ glasses, M = Li, Na, K and Cs, x=0.3, 0.4

Figure 2-6 Far-IR spectra of $xLi_2S + (1-x)(0.1Ga_2S_3 + 0.9GeS_2)$ glasses, x = 0.3,0.4 and 0.5

Figure 2-7 Far-IR spectra of $xNa_2S + (1-x)(0.1Ga_2S_3 + 0.9GeS_2)$ glasses, x = 0.2,0.3,0.4 , 0.5,0.6 and 0.67

Figure 2-8 Effect of NaI on Far-IR spectra of $xNa_2S + (1-x)(0.1Ga_2S_3 + 0.9GeS_2)$ glasses, x = 0.3 and 0.6

Figure 2-9 Far-IR spectra of $0.3M_2S + 0.7(0.1Ga_2S_3 + 0.9GeS_2)$ glasses, M = Li, Na, K and Cs

Table 2-1 Glass compositions examined in this study

Table 2-2 T_g, T_c and density values of the selected glasses

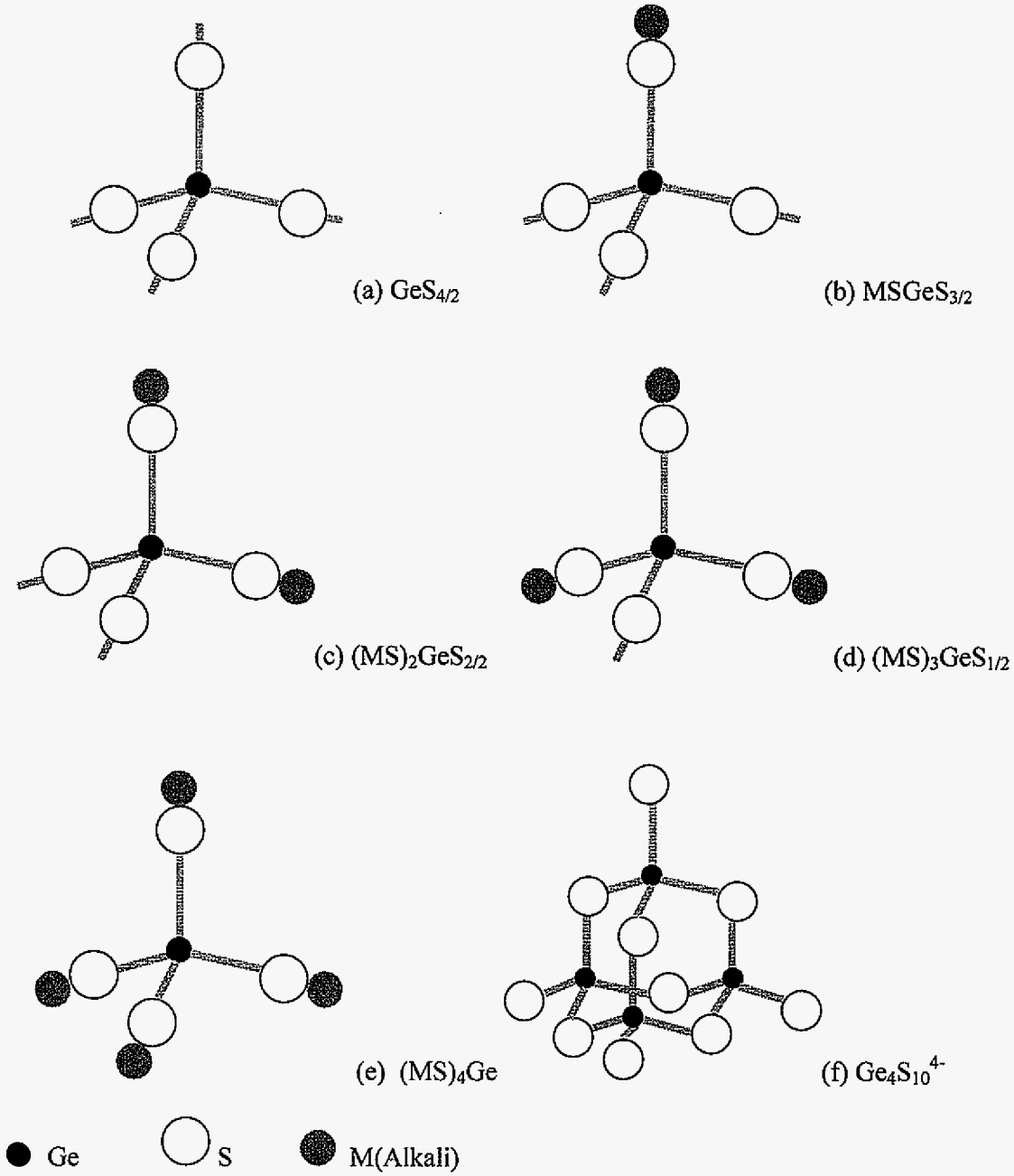
(a) $GeS_{4/2}$
(b) $MSGeS_{3/2}$
(c) $(MS)_2GeS_{2/2}$
(d) $(MS)_3GeS_{1/2}$
(e) $(MS)_4Ge$
(f) $Ge_4S_{10}^{4-}$
Ge
S
M(Alkali)

Figure 2- 1

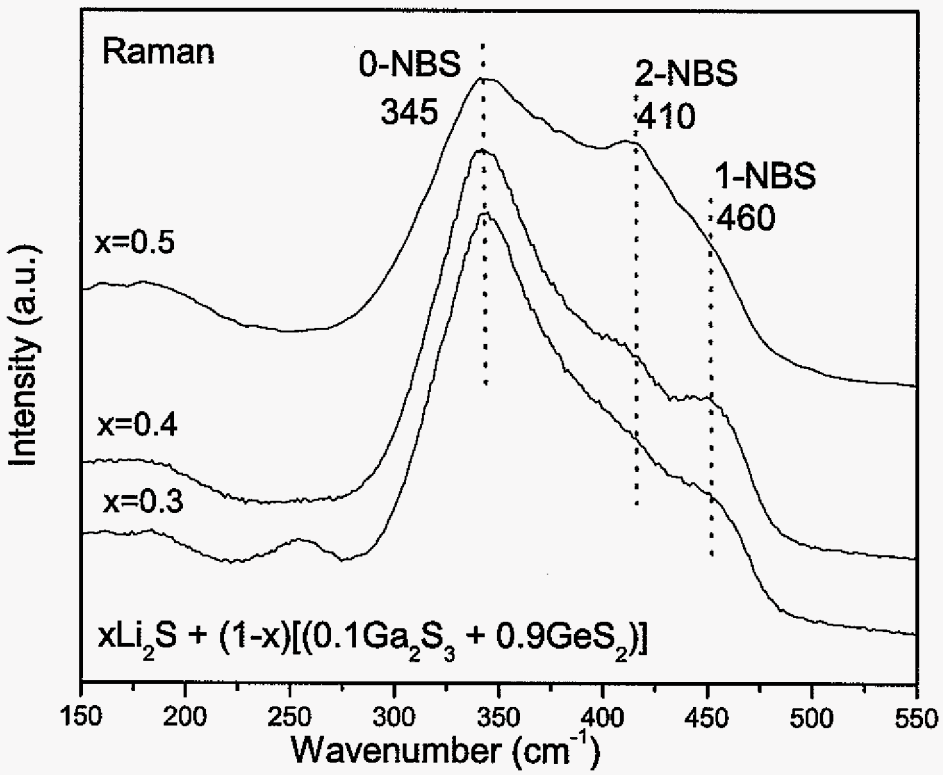
Raman
0-NBS
345
2-NBS
410
1-NBS
460
x=0.5
x=0.4
x=0.3
xLi2S + (1-x)[(0.1Ga2S3 + 0.9GeS2)]
Intensity (a.u.)
150
200
250
300
350
400
450
500
550
Wavenumber (cm-1)

Figure 2- 2

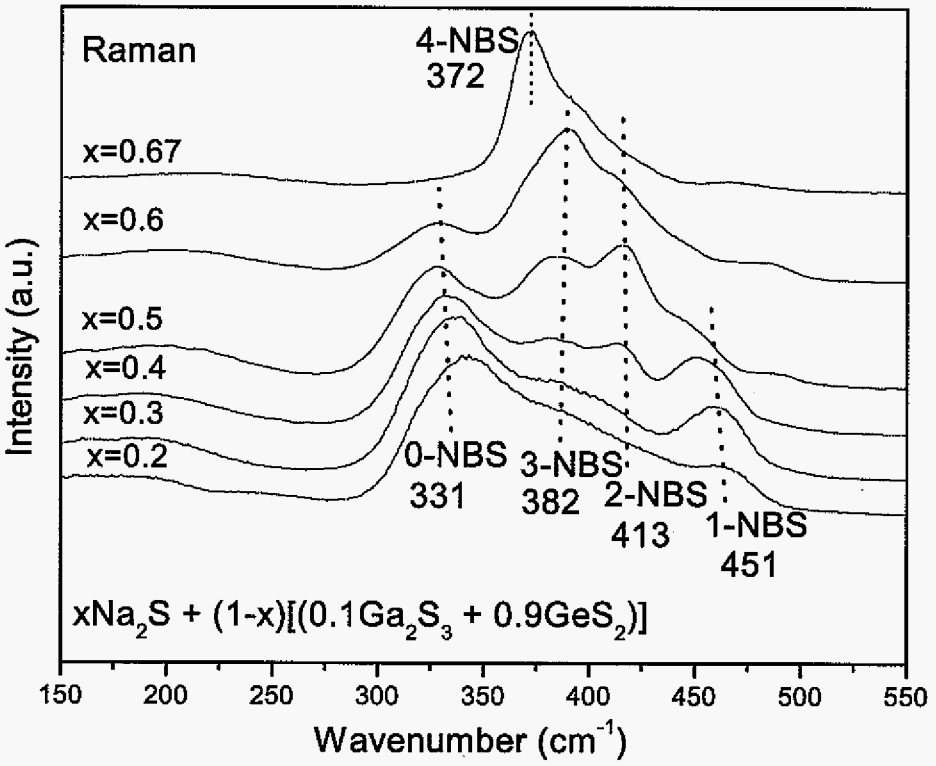
Raman
4-NBS
372
x=0.67
x=0.6
x=0.5
x=0.4
x=0.3
x=0.2
0-NBS
331
3-NBS
382
2-NBS
413
1-NBS
451
xNa2S + (1-x)[(0.1Ga2S3 + 0.9GeS2)]
Intensity (a.u.)
150
200
250
300
350
400
450
500
550
Wavenumber (cm-1)

Figure 2- 3

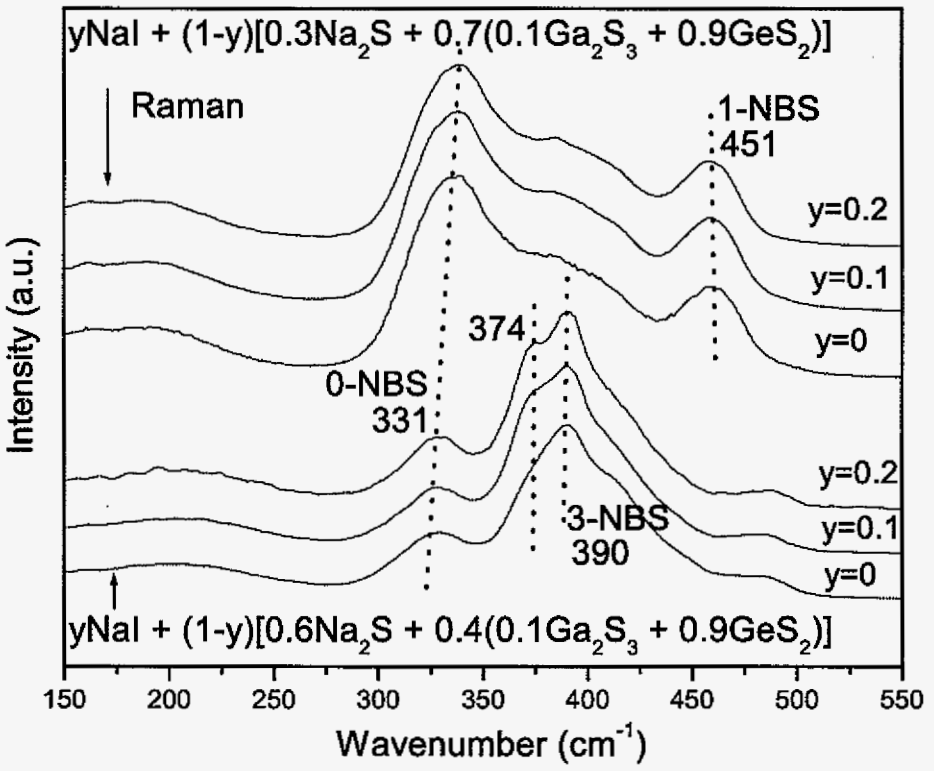
yNaI + (1-y)[0.3Na2S + 0.7(0.1Ga2S3 + 0.9GeS2)]
Raman
1-NBS
451
y=0.2
y=0.1
y=0
374
0-NBS
331
y=0.2
3-NBS
390
y=0.1
y=0
yNaI + (1-y)[0.6Na2S + 0.4(0.1Ga2S3 + 0.9GeS2)]
Intensity (a.u.)
150
200
250
300
350
400
450
500
550
Wavenumber (cm-1)

Figure 2- 4

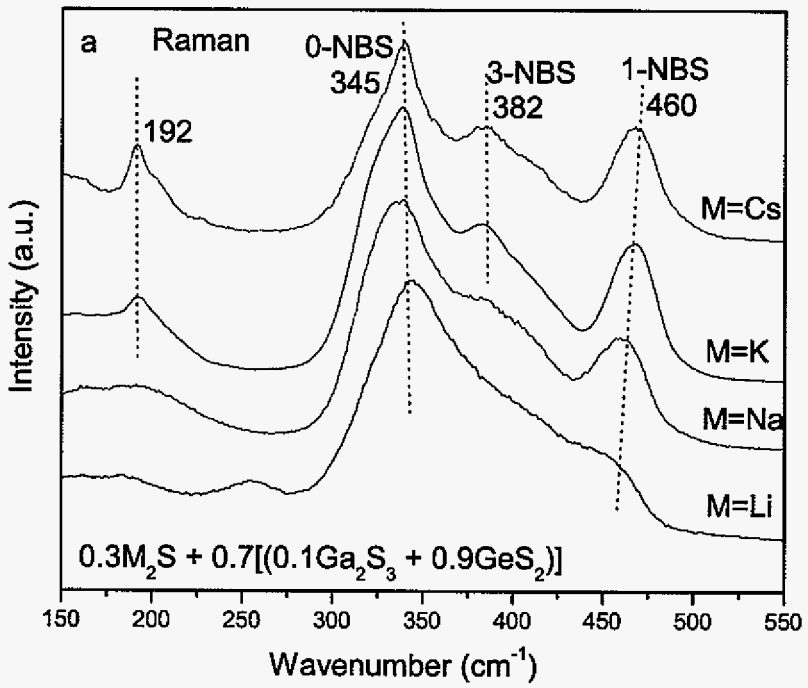
a
Raman
0-NBS
345
3-NBS
382
1-NBS
460
192
M=Cs
M=K
M=Na
M=Li
0.3M2S + 0.7[(0.1Ga2S3 + 0.9GeS2)]
Intensity (a.u.)
150
200
250
300
350
400
450
500
550
Wavenumber (cm-1)

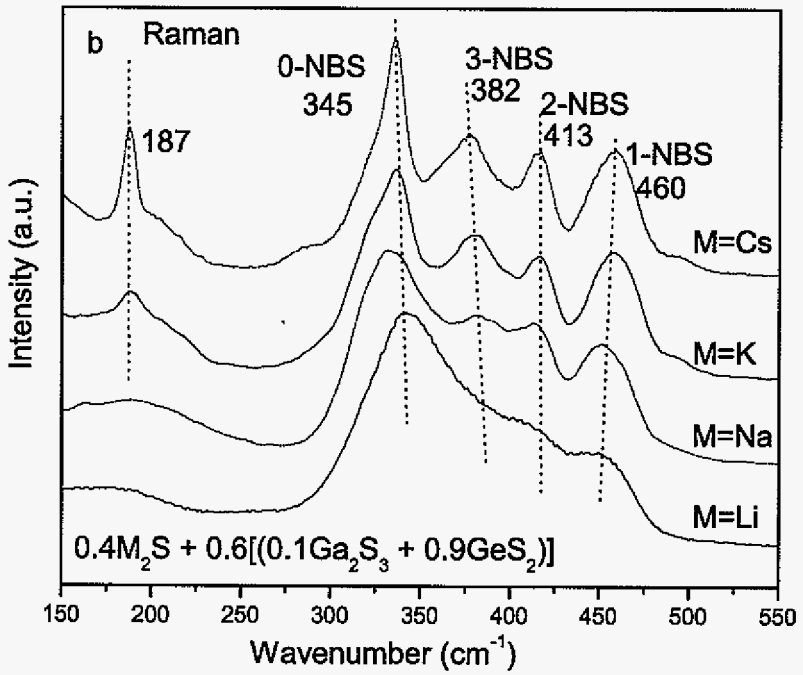
b
Raman
0-NBS
345
3-NBS
382
2-NBS
413
1-NBS
460
187
M=Cs
M=K
M=Na
M=Li
0.4M2S + 0.6[(0.1Ga2S3 + 0.9GeS2)]
Intensity (a.u.)
150
200
250
300
350
400
450
500
550
Wavenumber (cm-1)

Figure 2-5

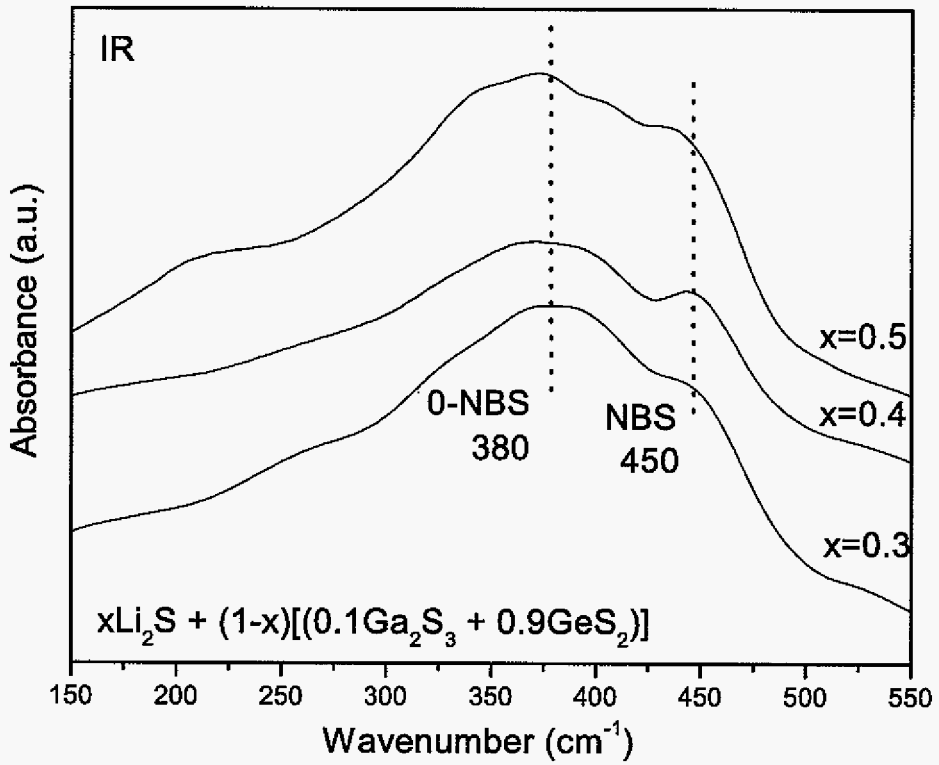
IR
Absorbance (a.u.)
0-NBS
380
NBS
450
x=0.5
x=0.4
x=0.3
xLi2S + (1-x)[(0.1Ga2S3 + 0.9GeS2)]
150
200
250
300
350
400
450
500
550
Wavenumber (cm-1)

Figure 2-6

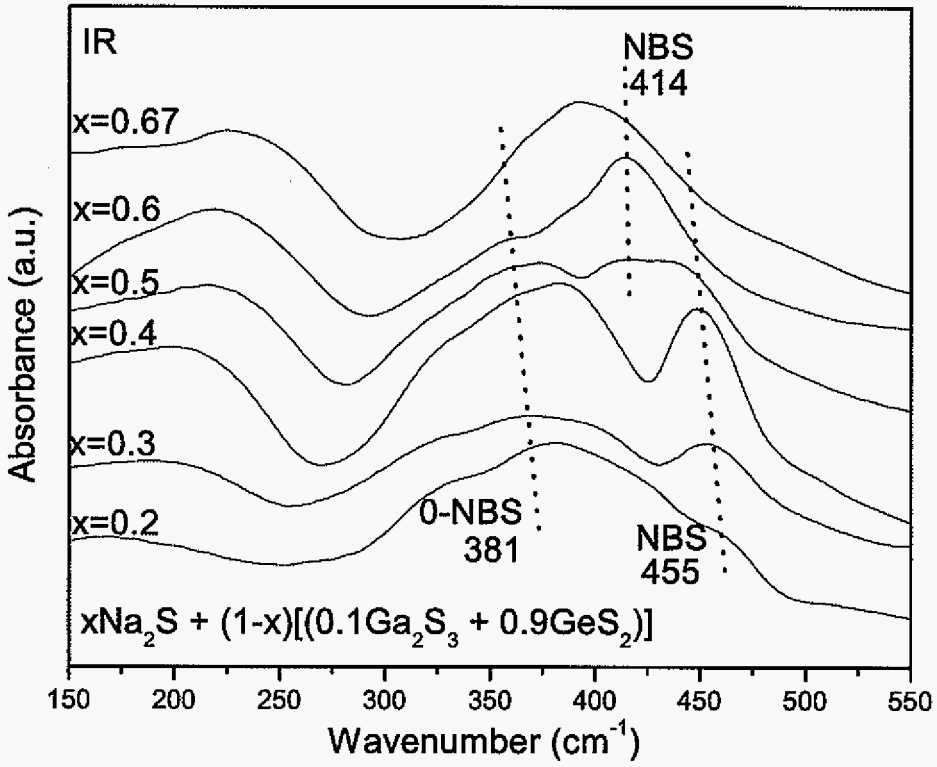
IR
NBS
414
x=0.67
x=0.6
x=0.5
x=0.4
x=0.3
x=0.2
0-NBS
381
NBS
455
xNa2S + (1-x)[(0.1Ga2S3 + 0.9GeS2)]
Absorbance (a.u.)
150
200
250
300
350
400
450
500
550
Wavenumber (cm-1)

Figure 2-7

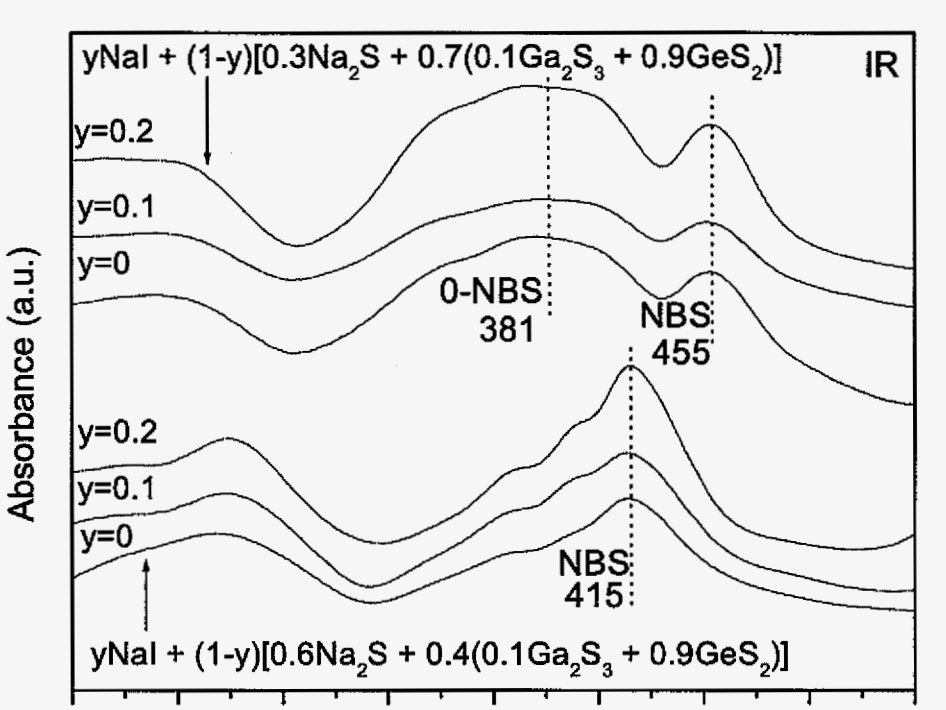
yNaI + (1-y)[0.3Na2S + 0.7(0.1Ga2S3 + 0.9GeS2)]
IR
y=0.2
y=0.1
y=0
0-NBS
381
NBS
455
y=0.2
y=0.1
y=0
NBS
415
yNaI + (1-y)[0.6Na2S + 0.4(0.1Ga2S3 + 0.9GeS2)]
Absorbance (a.u.)
150
200
250
300
350
400
450
500
550
Wavenumber (cm-1)

Figure 2-8

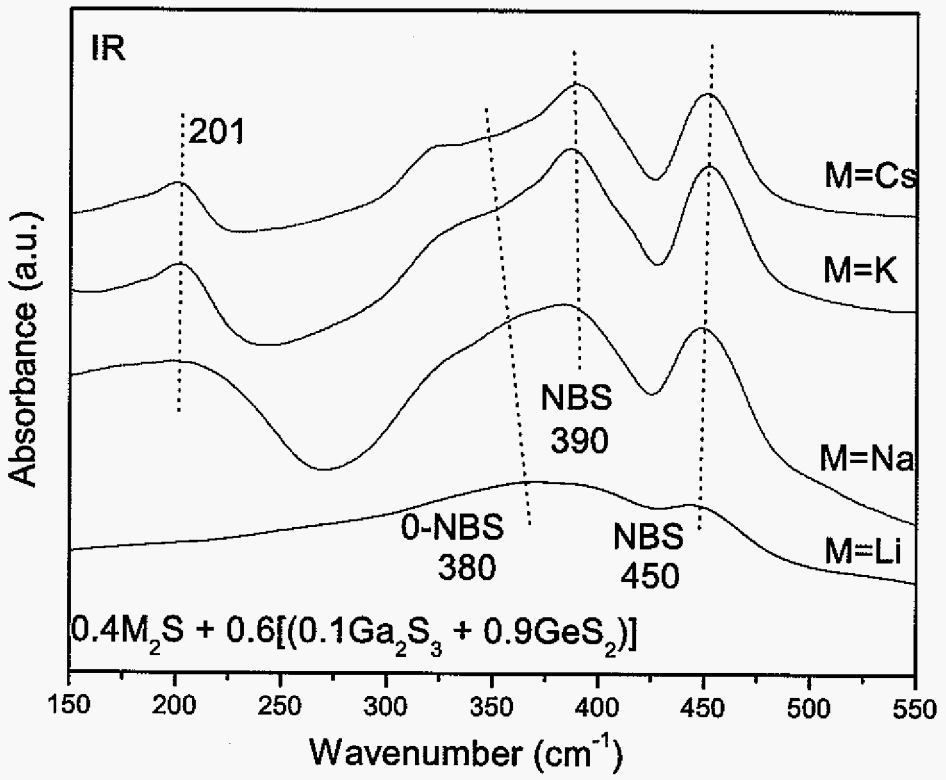
IR
201
M=Cs
M=K
NBS
390
M=Na
0-NBS
380
NBS
450
M=Li
0.4M2S + 0.6[(0.1Ga2S3 + 0.9GeS2)]
Absorbance (a.u.)
150
200
250
300
350
400
450
500
550
Wavenumber (cm-1)

Figure 2-9

Table 2-1

$yMI + (1-y)[xM_2S + (1-x)(0.1Ga_2S_3 + 0.9GeS_2)]$	x	y
M = Li	0.3-0.5	0-0.3
M = Na	0.2-0.67	0-0.2
M = K	0.3, 0.4	0-0.1
M = Cs	0.3, 0.4	0-0.1

Table 2- 2

Composition $yMI + (1-y)[xM_2S + (1-x)(0.1Ga_2S_3 + 0.9GeS_2)]$	Tg (°C) (±5°C)	Tc (°C) (±5°C)	Density (g/cm^3)
M = Li, x = 0.3, y = 0	320	395	2.82±0.05
M = Li, x = 0.3, y = 0.3	272	372	2.97±0
M = Na, x = 0.3, y = 0	313	432	2.74±0.04
M = Na, x = 0.3, y = 0.2	262	426	2.78±0.04
M = K, x = 0.3, y = 0	294	406	2.57±0.02
M = K, x = 0.3, y = 0.1	283	426	2.63±0.01
M = Cs, x = 0.3, y = 0	292	387	3.43±0.04
M = Cs, x = 0.3, y = 0.1	282	438	3.30±0.02
$xNa_2S + (1-x)(0.1Ga_2S_3 + 0.9GeS_2)$			
x = 0.2	331	449	----
x = 0.3	313	432	2.74±0.04
x = 0.4	286	>400	2.64±0
x = 0.5	270	365	2.54±0.02
x = 0.6	264	365	2.44±0.04
x = 0.67	304	366	----

2.8 References

[1] E. I Kamitsos, G. D.Chryssikos, A. P. Patsis, Solid State Ionics, Proc.Symp.A2 Int.Conf.Adv.Mater. (1992) 331.

[2] E. I. Kamitsos, W. M. Risen, Journal of Non-Crystalline Solids 65 (2-3) (1984) 333.

[3] J. Cho, PhD thesis, Iowa State University (1995).

[4] J. L. Souquet, E. Robinel, B. Barrau, M. Ribes, Solid State Ionics 3-4 (1981) 317.

[5] B. Barrau, M. Ribes, M. Maurin, A. Kone, J. L. Souquet, Journal of Non-Crystalline Solids 37 (1980) 1.

[6] E. I. Kamitsos, J. A. Kapoutsis, G. D. Chryssikos, G. Taillades, A. Pradel, M.Ribes, Journal of Solid State Chemistry 112 (2) (1994) 255.

[7] C. R. Nelson, S. A. Poling, S.W. Martin, Journal of Non-Crystalline Solids 337 (2004) 78.

[8] J. Heo, J. D. Mackenzie, Journal of Non-Crystalline Solids 113 (1) (1989) 1.

[9] Y. Kim, J. Saienga, S.W. Martin, Journal of Non-Crystalline Solids 351 (49-51) (2005) 3716.

[10] B.Meyer, F. Borsa, S.W. Martin, Journal of Non-Crystalline Solids 337 (2) (2004) 166.

[11] J. Heo, J. M.Yoon, S.Y. Ryou, Journal of Non-Crystalline Solids 238 (1-2) (1998) 115.

[12] J. Saienga, Y. Kim, B. Campbell, S.W. Martin, Solid State Ionics 176 (2005) 1229.

[13] S. A. Poling, S.W.Martin, J.T.Sutherland, US Patent Application Serial No. 10/627, 584 (7-25-2003).

[14] M.A. Chad, PhD thesis, Iowa State University (2006).

[15] Y. Kawamoto, C. Kawashima, Materials Research Bulletin 17 (12) (1982) 1511.

[16] H. L.Tuller, D. P. Button, D. R.Uhlmann, Journal of Non-Crystalline Solids 40 (1980) 93.

[17] K. Miyauchi, J. Qiu, M. Shojiya, Y. Kawamoto, N. Kitamura, Journal of Non-Crystalline Solids 279 (2-3) (2001) 186.

[18] E.D Lacy, Physics and Chemistry of Glasses 4 (6) (1963) 234.

[19] S. Pohl, B. Krebs, Zeitschrift fuer Anorganische und Allgemeine Chemie 424 (3) (1976)

265.

[20] K. O. Klepp, M. Zeitlinger, Zeitschrift fuer Kristallographie - New Crystal Structures 215 (1) (2000) 7.

[21] K. O. Klepp, F.Fabian, Zeitschrift fuer Naturforschung, B: Chemical Sciences 54 (12) (1999) 1499.

3. Ionic Conductivity of Glasses in the MI + M_2S + ($0.1Ga_2S_3 + 0.9GeS_2$) (M=Li, Na, K and Cs) System

A paper to be submitted to Solid State Ionics

Wenlong Yao[1], Steve W. Martin[1,2]

Abstract:

The LiI + Li_2S + GeS_2 + Ga_2S_3 system was previously studied to optimize the properties for use in the solid state lithium batteries. In this study the $0.1Ga_2S_3 + 0.9GeS_2$ is chosen because it was experimentally found that it could be combined with all the alkali sulfides to yield glasses in the same glass forming range. Both M_2S and MI (M=Li, Na, K and Cs) were added to form broad glass forming ranges to study the ionic conductivity systematically in these fast ionic conducting (FIC) chalcogenide glasses. As expected, both additions of alkali sulfide (M_2S) and alkali iodide (MI) help to improve the conductivity of glass. Only the conductivity of 60% Na_2S glasses reaches saturation with the addition of NaI. The ionic conductivities show significant differences between Li_2S, Na_2S and K_2S, Cs_2S glasses due to the large differences between their activation energies. The alkali radius effect on the activation energy was discussed based on the modified Anderson and Stuart model.

3.1 Introduction

Fast ion conducting (FIC) sulfide glasses are well known to have large ionic conductivities compared to their oxide counterparts and for this reason are potential solid

[1] Department of Materials Science & Engineering, Iowa State University, Ames, IA 50011
[2] Author to whom correspondence should be directed

state electrolytes in high energy density , high performance batteries [1,2]. These glasses are isotropic, lack grain boundaries, easily fabricated into complex shapes and have wide compositional flexibility to optimize their properties and conductivity.

Extensive studies have been done to understand the mechanisms of ionic transport in these ionic glasses in the past [2-7]. While it is still not clear how ions transport in glass, it is well known that the ionic conductivity consists of two terms, the concentration of charge carrier (n) and their mobility (μ). To date there is no method to separate the individual contribution to the total ionic conductivity. Anderson and Stuart proposed that the ion transport needed to overcome two energy barriers [8]: a binding energy or coulomb energy is required to dissociate the mobile cations from the non-bridging oxygen and a strain energy is needed to dilate the glasses structure sufficiently to allow the mobile cations to pass to the next available site. The Anderson-Stuart model has been extensively applied to alkali oxide glasses, mixed anion conductor glasses, some chalcogenide glasses and even to new Li^+ ion conducting glasses [9-13]. Another theory, the weak electrolyte theory, proposes that the process of carrier generation dominates the ion transport process, while the mobility is thought to be independent of glass composition [4,5,14]. To understand ion transport in glasses, alkali oxide glasses have been studied widely since they are usually good glasses former and are easily prepared and handled [3,15,16]. For the chalcogenide glasses, most research has been done on lithium or silver ion conductor glasses because of their high ionic conductivity [17-20]. However, very little research has been done on a series of alkali chalcogenide glasses because of difficulty to obtain the high purity alkali (especially for K and Cs) chalcogenide compounds and lack of high conductivity. The binary alkali sulfide and germanium sulfide system has been studied by different groups [21,22].

In previous, work the glass formation in the LiI + Li_2S + GeS_2 + Ga_2S_3 system has been studied to optimize their properties for use in solid state lithium batteries [23]. GeS_2 was chosen as a good glass former and Ga_2S_3 was added to act as a glass intermediate to extend the glass forming range and to increase the ionic conductivity and glass transition temperature (T_g). In this study, $0.1Ga_2S_3 + 0.9GeS_2$ was chosen as the basic glasses former system because it was found to have the most extensive glass forming range for all of the alkali sulfides and the different alkali (Li, Na, K and Cs) sulfides were systematically added into $0.1Ga_2S_3$+$0.9GeS_2$ glass system. Based on the structure of $0.1Ga_2S_3$+$0.9GeS_2$, the effects of concentration of charge carriers change and structure change due to the addition of alkali sulfides and iodides on the electrical conductivity can help to understand the ion transport process in these FIC sulfide glasses.

3.2 Experimental methods

All glass batching and melting operations were carried out in an oxygen- and water-free (< 5ppm) glove-box. High purity glassy GeS_2 was synthesized by the reaction of elemental germanium metal (Cerac, 99.999%) and sulfur (Alfa Aesar 99.999%) at high temperature (900 °C) in an evacuated silica ampoule [24]. Since high purity M_2S (M = Na, K and Cs) are not commercially available, high purity MSH (M = Na, K and Cs) were prepared by the reaction of MOH (M = Na, K and Cs) and high pressure H_2S gas using a method developed by Poling [25] and improved by Martindale [26]. Na_2S was obtained by decomposing the NaSH at ~600 °C. For K and Cs, the KSH and CsSH were used directly and decomposed into M_2S and H_2S gas at high temperature during preparing the glasses. Weight

loss, IR and Raman spectroscopy are used to verify that MSH fully decomposes to M_2S evolving H_2S at elevated temperature.

The MI + M_2S + ($0.1Ga_2S_3 + 0.9GeS_2$) (M = Li, Na, K and Cs) glasses were prepared by melting stoichiometric amounts of Ga_2S_3 (Alfa 99.99%), GeS_2, MI (LiI, Cerac 99%, NaI, Alfa 99.9%, KI, Alfa 99.9%, CsI, Aldrich 99.9%) and M_2S(Li_2S, Alfa 99.9%, Na_2S) or MSH (KSH, CsSH) between 870 °C and 920 °C for 6 mins. in vitreous carbon crucibles inside a high quality glovebox. The melts were quenched in a brass mold at room temperature. Weight loss measurements were done by removing carbon crucible out of furnace after 3 mins. Melting time and all measured weight losses due to evaporation were generally less than 5 wt. %. Bulk glass discs for density and conductivity measurements were made by quenching the melt on a pre-heated brass mold held at 30 to 50 °C below the glass transition temperature (T_g), annealing at this temperature for 30 mins. and slowly cooled (2 °C/min) to room temperature.

The bulk glass discs were carefully dry polished inside the glove box to 4000 grit using SiC polishing papers to improve the electrode/glass contact surfaces. The polished glass discs were then sputter coated with gold on both sides to form blocking electrodes for the conductivity experiments. The sputtering, also performed inside the glove box, was performed at a pressure of 10^{-1} mbar of Argon with a current of 18 mA for a total of four minutes on each side and the thickness of gold film is ~20 nm. The glass discs were put into an airtight sample chamber which then was connected to a Solartron 1260 Impedance Gain-Phase Analyzer to measure the magnitude and phase angle of the impedance of the sample. The measurements were made by applying a sinusoidal voltage (50 mV) across the sample from room temperature to ~200 °C over a frequency range of 0.003 Hz to 10 MHz. The

sample temperature was controlled to within ±1 °C by placing the heater around sample area of sample chamber.

3.3 Results

The LiI + Li_2S + GeS_2 + Ga_2S_3 glass system has been previously studied by Saienga in our research group to optimize their properties for use in solid state lithium batteries [23]. GeS_2 was chosen as a good glass former, and Ga_2S_3 was added to act as a glass intermediate to improve the glass forming ability and to increase the ionic conductivity and T_g of the glass. In the present study, the $0.1Ga_2S_3 + 0.9GeS_2$ base glass forming system was selected because it was experimentally found that it could be combined with all the alkali sulfides to yield glasses in the same glass forming range. Other systems such as B_2S_3, for example, were found to yield glasses for some of the alkali sulfides, but the glass forming range was not wider than that of $xM_2S + (1-x)(0.1Ga_2S_3 + 0.9GeS_2)$ system. To increase the conductivity further, alkali iodides were added to these glasses.

Table 3-1 shows all of the compositions that were prepared and examined. It was found that the different alkali compositions show different glass forming abilities. For example, it was found that the Li and Na compositions have wide glass forming ranges, while the K and Cs system had more limited glass forming ranges. There were some differences in the glass forming ranges for the different alkali sulfide system, but the above compositions were found to be sufficient to study both the compositional dependence of the conductivity within any one alkali sulfide system and to compare these compositional dependences of the conductivity among the different alkali to examine the effect of alkali ion radius on the conductivity.

The d.c conductivity was determined using a Nyquist plot by extrapolating the imaginary part of the complex impedance to the intercept along the real part of the impedance axis. The impedance is usually high at room temperature, where the complex plane plot is seen as a semicircle. The arc will disappear into a spike due to electrode polarization processes when the temperature increases and the impedance decreases. For all samples, the d.c. conductivity $\sigma_{d.c.}$ dependence on temperature T was found to follow an Arrhenius equation of the form:

$$\sigma_{d.c.}(T) = \frac{\sigma_0}{T}\exp(\frac{-\Delta E_{act}}{RT}) \qquad \text{Equation 3-1}$$

where, σ_0 is the pre-exponential factor and ΔE_{act} the activation energy of the ionic conductivity.

The effect of alkali sulfide (M_2S) on the ionic conductivity of the glass samples was studied first. Figure 3-1 and Figure 3-2 show the Arrhenius plots of d.c ionic conductivity of Li_2S and Na_2S glasses. As expected, increasing of the Li_2S and Na_2S content increases the conductivity. The same amount increase of Li_2S content causes a higher increase in the conductivity of the glass compared to that of Na_2S system. Similar trends are also found for the K_2S and Cs_2S doped glasses, where 30% K_2S and Cs_2S glasses have lower conductivities than that of 40% K_2S and Cs_2S glasses.

The effect of alkali iodide (MI) doping on conductivity of the glasses is shown in Figure 3-3 and Figure 3-4 for the Li_2S and Na_2S glasses, respectively. For the 30% Li_2S glass, the increase of the LiI content increases the conductivity faster than the increase due to Li_2S addition. The same trend is also found in the 40% and 50% Li_2S glass. For the Na_2S glasses the addition of NaI still increases the conductivity as shown in Figure 3-4, but as the concentration of Na_2S increases, the magnitude of the effect of NaI addition on the

conductivity decreases. For example, for the 60% Na_2S glass shown in Figure 3-4, the addition of 10% NaI only slightly increases the conductivity and the conductivity of the 20% NaI doped glass is similar to that of 10% NaI doped glass. For the K_2S and Cs_2S glass, only 10% KI and CsI, respectively, could be added to the base glass before devitrification and for this addition the conductivity still increases.

With the same amount of alkali sulfide (M_2S) addition, the conductivity of glasses decreases with the increase of radius of alkali ions as shown in Figure 3-5 for 30% alkali sulfide (M_2S) glass composition. The K_2S and Cs_2S glasses have much lower conductivities than those of the Li_2S and Na_2S glasses. From these measurements, we conclude that the K and Cs glasses are actually poor ionic conductors. Indeed, the conductivity of the Cs glasses (even with CsI doping) is so low that the data is very noisy experimentally in the low frequency and low temperature range.

The activation energy ΔE_{act} and pre-exponent σ_0 were obtained from fitting the conductivity to the Arrhenius Equation 3-1. As found in many other studies, the pre-exponents of all the glass samples do not change significantly with the different glass compositions, varying between 10^5 and 10^6 (K/Ωcm). For this reason, the contribution to the change of the ionic conductivity with different compositions arises from the change of activation energy. For the Li_2S and Na_2S glasses, the activation energy ranges from a high of ~50 kJ/mol to a low of ~30 kJ/mol. For the K_2S and Cs_2S glasses, the conductivity activation energy ranges from a high of ~80 kJ/mol to a low of ~65 kJ/mol. Figure 3-6 shows the activation energy dependence on alkali radius for 30% alkali sulfide doped glasses. The large activation energy difference between the Li_2S , Na_2S and the K_2S ,Cs_2S glasses is reflected

in the larger difference in the ionic conductivity, with the ionic conductivity of the Li_2S and Na_2S being significantly larger than that of the K_2S and Cs_2S glasses.

The following, we will provide a detailed explanation, comparison, and structure dependence of the activation energies in these glasses. This study, for example, will provide the first detailed examination of the alkali ion radius dependence of the conductivity activation energy in alkali ion conducting sulfide glasses. While similar studies have been done for Li, Na and K oxide glasses by Button and Fusco et al. [3,15,16], the present study has extended this examination of the alkali ion radius dependence of the conductivity activation energy to the significantly large Cs^+ cation in the sulfide glasses where the sulfide glasses enable sufficient Cs^+ mobility to provide measurable conductivity below T_g. Cs^+ cations are sufficiently large as to produce negligible conductivity in oxide glasses.

3.4 Discussion

3.4.1 Review of structure of the glasses

The structure of the studied glasses has been studied by Raman and IR spectra [27]. As expected, the additions of alkali sulfides lead to the formation of non-bridging sulfurs. Most of the additions of the alkali iodides do not cause any obvious change in the Raman and IR spectra and it suggests that the additions don't lead to the change of the structure unit. At 60% Na_2S glass, there is one peak split into two peaks in Raman spectra with the addition of NaI which suggests the changes in the glass structure. Also a new peak appears in the Raman spectra in the K_2S and Cs_2S glasses, which is attributed to the formation of $Ge_4S_{10}^{-4}$ units in the glasses. This unit can be found in the $K_4Ge_4S_{10}$ and $Cs_4Ge_4S_{10}$ crystals. In the following, the relationship between structure and ionic conductivity will be discussed.

3.4.2 Composition dependence of the conductivity

The alkali sulfide (M_2S) works as glass modifier when added into the $0.1Ga_2S_3 + 0.9GeS_2$ glass forming system. So the alkali sulfide (M_2S) forms non-bridging sulfurs in the glass as found in the structure study of these glasses with Raman and IR spectroscopy. The mobile cation ions in these ion conducting glasses come from these cations bonded to non-bridging sulfurs. In order to participate in ionic conduction, the ion must disassociate from a non-bridging sulfur by overcoming the binding energy. Once the cation is dissociated it is believed that it must overcome a further energy barrier. This additional energy barrier is identified as a strain energy barrier and is strongly dependent upon the alkali cation radius. So when alkali sulfide (M_2S) concentration increases, the conductivity of samples also increases because more non-bridging sulfurs form and more alkali ions (M^+) are mobile in the glass. As expected, the conductivity decreases with the increase of the alkali ion radius. Although the composition of these different alkali sulfide doped glasses is analogous, the glass structure is different between Li, Na and K, Cs composition glasses due to the formation of $Ge_4S_{10}^{-4}$ units in K and Cs content glass. It may be possible that this unit will affect the transport of cation in these glasses. However, the important factor affecting the ionic conductivity is the radius of the alkali ion. The larger the radius of the ion, the more difficult it is for the ion to move through the glass network. The effect of alkali radius will be discussed below.

In our study of alkali iodide (MI) doping on the conductivity, the conductivity is found to saturate at 10% NaI for 60% Na_2S composition glasses. That is for the addition of 10% and 20% NaI, the conductivity of 60% Na_2S glasses shows very little change. The same saturation behavior can be found in Li_2S glasses at LiI concentration greater than 30%[23].

One possible explanation is that because of the low melting point of NaI there will be more NaI vaporization, so there will be a lower NaI content in the glass. However, weight loss measurements of all Na_2S compositions were ~2 wt. %. Furthermore, the higher the alkali modifiers content, the lower the required temperature of the melt and hence the lower the temperature used to melt and prepare the glass. This should lead to lower weight losses in the high alkali content glasses. It should be expected, therefore, that such conductivity saturation behavior would be more prevalent for the low alkali glasses. Hence, it is more likely that the addition of more than 10% NaI has no further contribution to the increase of conductivity and this leads to the conductivity saturation behavior. Many FIC glasses show an increase of the ionic conductivity with alkali iodide addition. It is usually thought that the added MI dissolves interstitially between the structural units of glass, instead of becoming an integral part of the glass structure [3]. Due to the large radius of I^- anion, it will dilate the glass structure and this will help to make cation ion move more easily. Different from the Li_2S glasses, the Na_2S glasses reach saturation at 10% NaI at the higher Na_2S compositions (60%) and this may be attributed to glass structure changes due to the addition of alkali sulfide (M_2S). The Raman spectra of 60% Na_2S have shown that the structure changes due to the addition of NaI. It is possible that the added NaI instead enter into the glasses structure and become integral part of the glass structure, which is not helpful to improve the conductivity.

3.4.3 Composition dependence of the activation energy

The plots of the activation energy against alkali iodide and alkali sulfide content are shown in Figure 3-7 and Figure 3-8. It is found that for the Li_2S glasses, the activation energy, as expected, decreases with the increase of LiI. For the Na_2S glasses, at low Na_2S

composition (30%), the activation energy decreases with increasing NaI content, but at 60% Na_2S, the activation energy changes slightly with the increase of NaI and this in turn leads to the behavior of conductivity saturation as discussed above. Similarly, the activation energy decreases with the increase of alkali sulfide concentration corresponding to the increase of conductivity.

In addition, the total alkali ion atomic fraction dependence of the room temperature conductivity and activation energy are plotted in Figure 3-9 where only data for the Li and Na glasses are plotted due to limited samples and data for K and Cs glasses. Figure 3-9 shows that as the total alkali fraction increases, the conductivity increases and the activation energy decreases. The trend is most clear for the Li glasses. The discontinuous jumps in the data are associated with the stepwise variance in the fraction of alkali sulfide in the glass. At highest ion fraction, the conductivity appears to saturate for the Na glasses. While not observed here, reference [23] shows that the Li glass also reaches saturation at higher fraction of Li.

The decrease in the activation energy with alkali content for the Li, Na and K glasses is consistent with previous reports of both oxide and sulfide glasses, yet a definitive explanation for the behavior is still lacking. Martin and Angell proposed some time ago that the decreasing activation energy with increasing alkali ion content may be due to the energy overlap of the coulombic potential energy that exist between sites [28]. At low alkali content the cations are more separated than at high alkali content and this forces the cation to overcome a higher potential energy before it is captured by the next cation site. This behavior has been qualitatively expected by Martin and Patel for $Na_2S + B_2S_3$ glasses, where the Na_2S

fraction varied from x=0.0001 to x=0.41 [29,30]. We will explore this relationship further below by an examination of the model of the conductivity activation energy.

To understand the compositional dependence activation energy more completely, the model for ionic conduction developed by Anderson and Stuart [8] is considered. This model proposes that the total measured activation energy consists of two parts in Equation 3-1: a coulombic energy, ΔE_b , and strain energy , ΔE_s. Equation 3-2 shows the coulombic energy of alkali modified by Greaves and Ngai [31] and Equation 3-3 shows the strain energy modified by McElfresh and Howitt [32].

$$\Delta E_{act} = \Delta E_b + \Delta E_s \qquad \text{Equation 3-1}$$

$$\Delta E_b = \frac{e^2}{4\pi\varepsilon_0\varepsilon_\infty}\left(\frac{1}{R_{M-S}} - \frac{1}{R_{M-M}}\right) \qquad \text{Equation 3-2}$$

$$\Delta E_s = \pi \cdot G\left(r - r_D\right)^2(\lambda/2) \qquad \text{Equation 3-3}$$

For these equations, e is the charge; ε_0 is the permittivity of free space and ε_∞ is the dielectric constant of glass at high frequency; $R_{M\text{-}S}$ is the distance between alkali ions and its neighboring sulfur ion and is equal to the radius of the alkali ion and sulfur; $R_{M\text{-}M}$ and λ actually are same and are the jump distance between equivalent alkali sites near non-bridging sulfur; G is the shear modulus; r_D is the radius of a network doorway or interstice opening; r is the radius of alkali ions.

The following, we explore which factors have an effect on the activation energies of our glasses based on the above model. Based on the Equation 3-2 and Equation 3-3, the relative magnitude of the calculation of the two energy term can be estimated using the appropriate parameters. The shear modulus G is found to be between 0.97 and 2.06×10^{10} N/m^2 for various chalcogenide glasses and the value of 2×10^{10} N/m^2 is used for all of the studied glasses. This value comes from the $Ga_2S_3 + GeS_2 + MCl$ (M=alkali ions) system and is similar to our glass system [12]. r_D is assumed to be same for all the studied glass and the value of 0.3Å is taken from the previous detailed analysis of similar $Li_2S + GeS_2$ binary glasses[33]. ε_∞ is also assumed to be same for all the studied glass and the value is 10 based on our measurement of dielectric constant at high frequency. The jump distance value was estimated from cation separation distances calculated through the density.

Table 3-2 lists the calculated binding energy and strain energies using the above equations with appropriate parameters for some of the studied glasses. As we can see, the equations only give the relative magnitudes of the activation energies and are compared to our experimental activation energies. However, from the trend in the calculated energy we can learn which factor was important in the total activation energy. With the addition of alkali sulfide, the activation energy decreases because the jump distance decreases due to the concentration of alkali ions, but the magnitude of the activation energy doesn't change much. However, the composition change from Li_2S to Cs_2S, the calculated activation energy shows much difference, similar to the experimental activation energy. From Equation 3-1, ΔE_b is largest for the smallest cation and smallest for the largest cation. In a similar way, ΔE_s is smallest for the smallest cation and largest for the largest cation. Due to these trends, the strain energy term is a small fraction of the total activation energy for the Li glasses, while it

is a dominant fraction of the total activation energy for the Cs_2S glass. Table 3-2 shows that ΔE_b does not change much in all alkali glasses, but ΔE_s increases dramatically from Na_2S to K_2S to Cs_2S glasses due to the change of alkali radius and this is the cause of the large difference in the conductivity of the Na and K glasses as observed in the experiment. The large difference between the K_2S and Cs_2S glasses in the calculated activation energy is not observed and it may suggest that G or r_D changes significantly although we assume they are constant in the calculation. From the calculated energy, it is found that the radius of the ion is so important to determine the activation energy. However, the calculation of the activation energy based on the Anderson and Stuart model only give relative magnitude of activation energy and it is difficult to precisely determine the binding energy and strain energy. In our other work, the binding energy will be determined with temperature dependence mobile cation density based on space charge polarization theory and the binding energy and strain energy will be separated.

3.5 Conclusions

The alkali sulfide (M_2S) and alkali iodide (MI) were systematically added into $0.1Ga_2S_3 + 0.9GeS_2$ glass form system to study the ionic conductivity. It is found that the K_2S and Cs_2S compositions have limited glass forming ability comparing to Li_2S and Na_2S composition, but the same amount of addition of alkali sulfide glasses was obtained for all alkali glasses. As expected, both additions of alkali sulfide (M_2S) and alkali iodide (MI) help to improve the conductivity of glass. The conductivity of 60% Na_2S glasses reaches saturation with the addition of NaI. With the increase of radius of alkali ions the conductivity decreases, especially for K_2S and Cs_2S glasses, the conductivity is so low comparing to that

of Li_2S and Na_2S glasses that they are poor ionic conductor. The large difference of the activation energy between Na_2S and K_2S glasses was found which leads to the poor conductivity of K_2S glass. The discussion of compositional dependence of activation energy was discussed based on the modified Anderson and Stuart model. The radius of alkali ions was found to be important to determine the activation energy of ionic conductivity.

3.6 Acknowledgements

This work is supported by National Science Foundation grant # DMR-0610813.

3.7 Captions

Figure 3-1 Temperature dependence of d.c conductivity in $xLi_2S + (1-x)(0.1Ga_2S_3 + 0.9GeS_2)$ glasses, x = 0.3, 0.4 and 0.5

Figure 3-2 Temperature dependence of d.c conductivity in $xNa_2S + (1-x)(0.1Ga_2S_3 + 0.9GeS_2)$ glasses, x = 0.3, 0.4, 0.5 and 0.6

Figure 3-3 Temperature dependence of d.c conductivity in $yLiI + 0.7[0.3Li_2S + (1-x)(0.1Ga_2S_3 + 0.9GeS_2)]$ glasses, y = 0, 0.1, 0.2 and 0.3

Figure 3-4 Temperature dependence of d.c conductivity in $yLiI + (1-y)[xLi_2S + (1-x)(0.1Ga_2S_3 + 0.9GeS_2)]$ glasses, y = 0, 0.1, 0.2 and x=0.3, 0.6

Figure 3-5 Temperature dependence of d.c conductivity in $0.3M_2S + 0.7(0.1Ga_2S_3 + 0.9GeS_2)$ glasses, M = Li, Na, K and Cs

Figure 3-6 Alkali radius dependence of activation energy in $0.3M_2S + 0.7(0.1Ga_2S_3 + 0.9GeS_2)$ glasses, M = Li, Na, K and Cs

Figure 3-7 Alkali iodides (MI) composition dependence of activation energy

Figure 3-8 Alkali sulfides (M_2S) composition dependence of activation energy

Figure 3-9 Alkali atomic fractions dependence of activation energy and d.c conductivity at room temperature (M = Li and Na)

Table 3-1 Glasses compositions studied in this study

Table 3-2 Calculated binding energy, strain energy, activation energy based on modified Anderson and Stuart model and experimental activation in some glasses

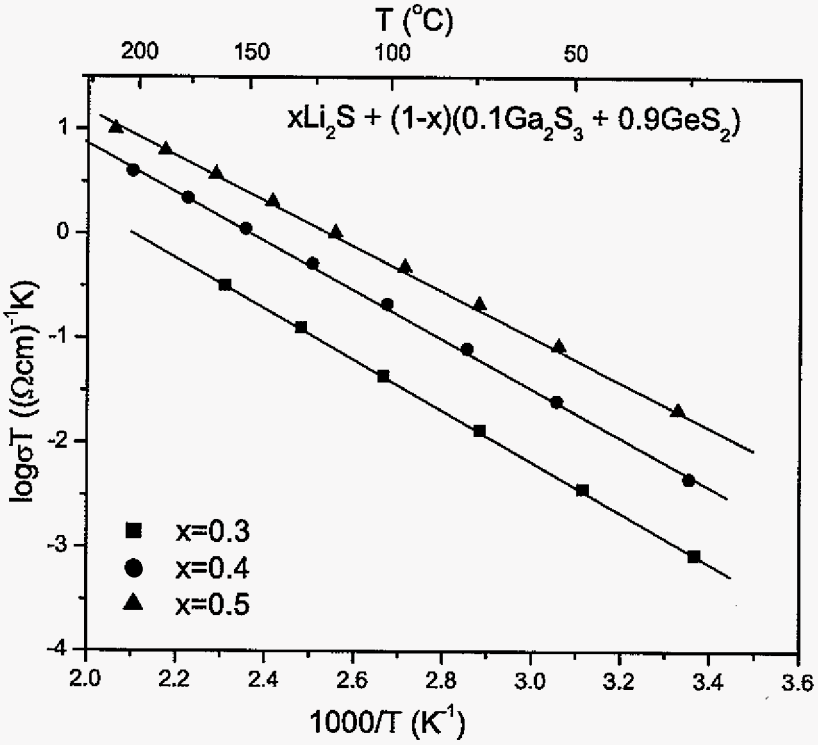
T (°C)
200
150
100
50
xLi2S + (1-x)(0.1Ga2S3 + 0.9GeS2)
logσT ((Ωcm)-1K)
1
0
-1
-2
-3
-4
x=0.3
x=0.4
x=0.5
2.0
2.2
2.4
2.6
2.8
3.0
3.2
3.4
3.6
1000/T (K-1)

Figure 3- 1

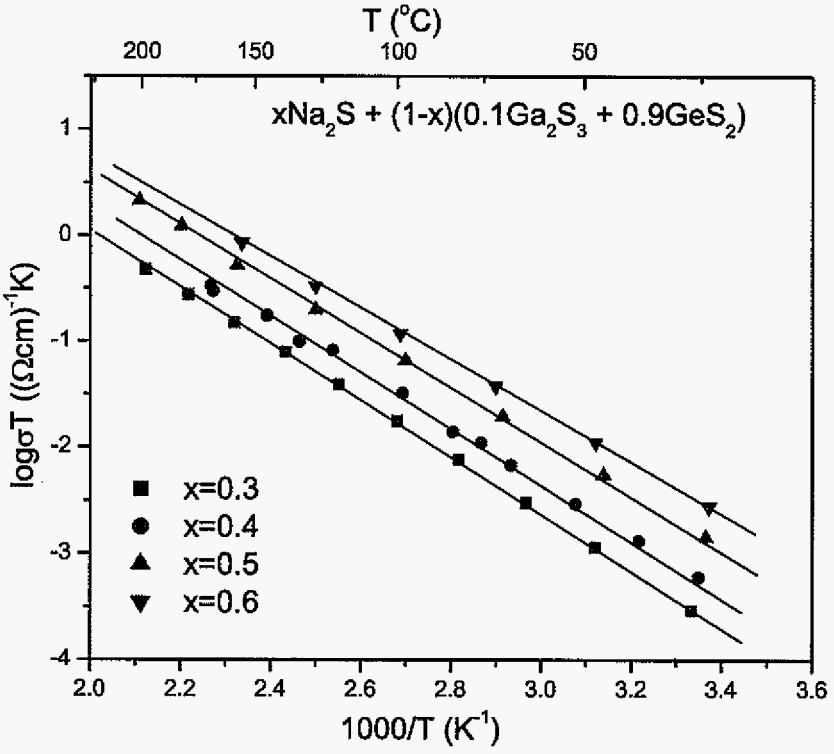
T (°C)
200
150
100
50
xNa2S + (1-x)(0.1Ga2S3 + 0.9GeS2)
logσT ((Ωcm)-1K)
1
0
-1
-2
-3
-4
x=0.3
x=0.4
x=0.5
x=0.6
2.0
2.2
2.4
2.6
2.8
3.0
3.2
3.4
3.6
1000/T (K-1)

Figure 3- 2

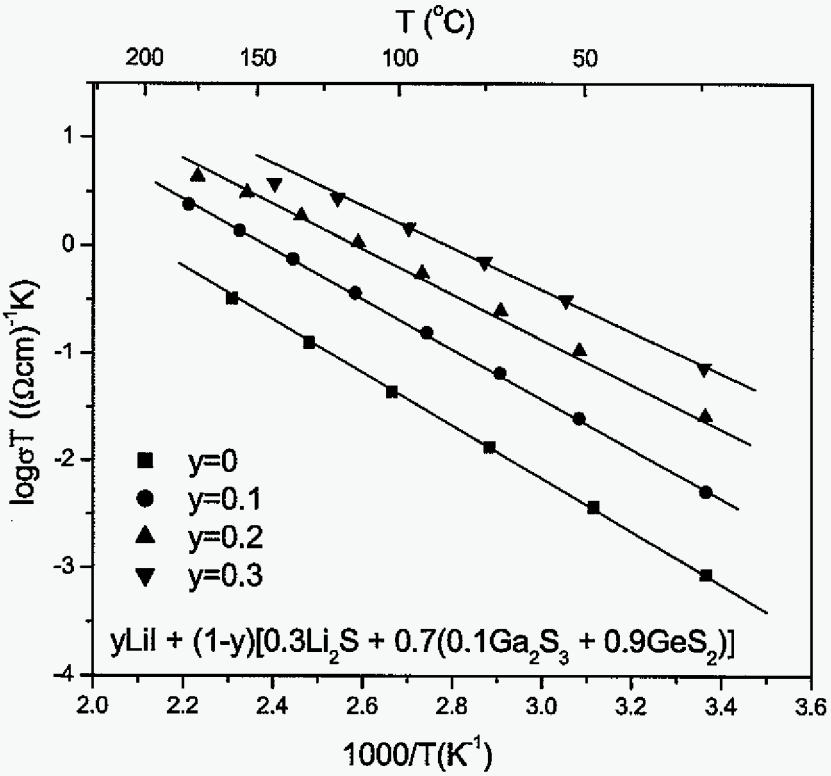
T (°C)
200
150
100
50
1
0
-1
-2
-3
-4
logσT ((Ωcm)$^{-1}$K)
y=0
y=0.1
y=0.2
y=0.3
yLiI + (1-y)[0.3Li$_2$S + 0.7(0.1Ga$_2$S$_3$ + 0.9GeS$_2$)]
2.0
2.2
2.4
2.6
2.8
3.0
3.2
3.4
3.6
1000/T(K^{-1})

Figure 3- 3

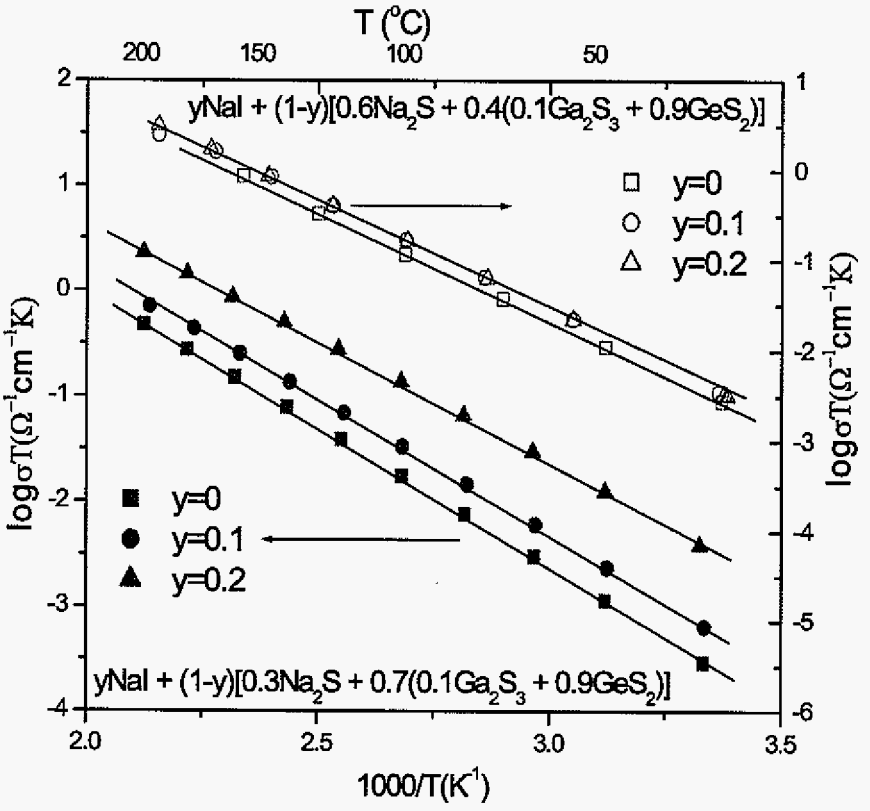
T (°C)
200
150
100
50
yNaI + (1-y)[0.6Na2S + 0.4(0.1Ga2S3 + 0.9GeS2)]
y=0
y=0.1
y=0.2
yNaI + (1-y)[0.3Na2S + 0.7(0.1Ga2S3 + 0.9GeS2)]
y=0
y=0.1
y=0.2
logσT(Ω-1cm-1K)
logσT(Ω-1cm-1K)
1000/T(K-1)
2.0
2.5
3.0
3.5

Figure 3- 4

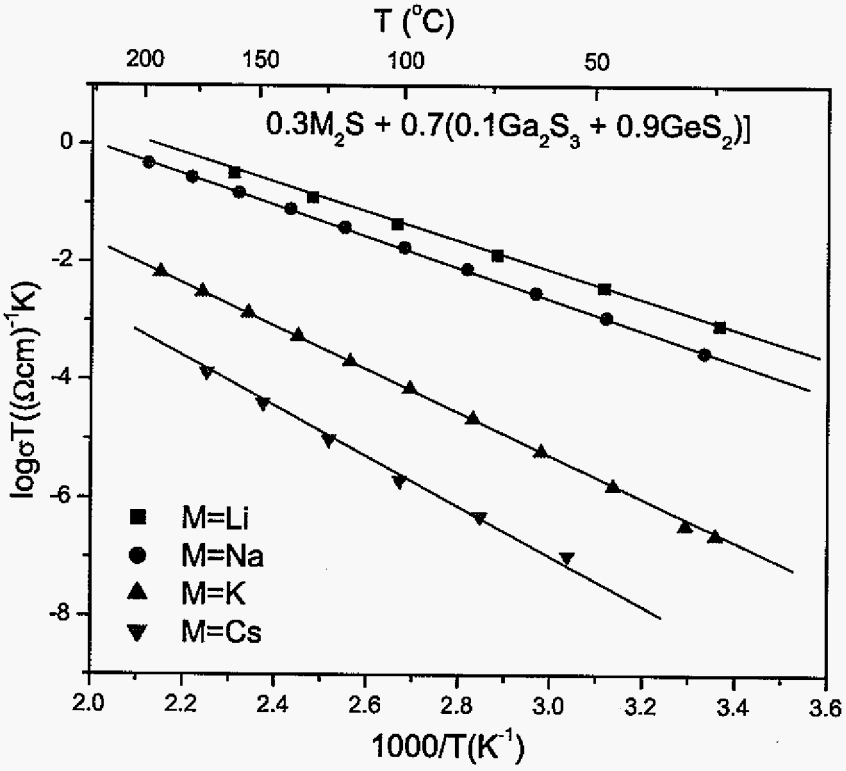
T (°C)
200
150
100
50
0.3M2S + 0.7(0.1Ga2S3 + 0.9GeS2)]
0
-2
-4
-6
-8
logσT((Ωcm)-1K)
M=Li
M=Na
M=K
M=Cs
2.0
2.2
2.4
2.6
2.8
3.0
3.2
3.4
3.6
1000/T(K-1)

Figure 3- 5

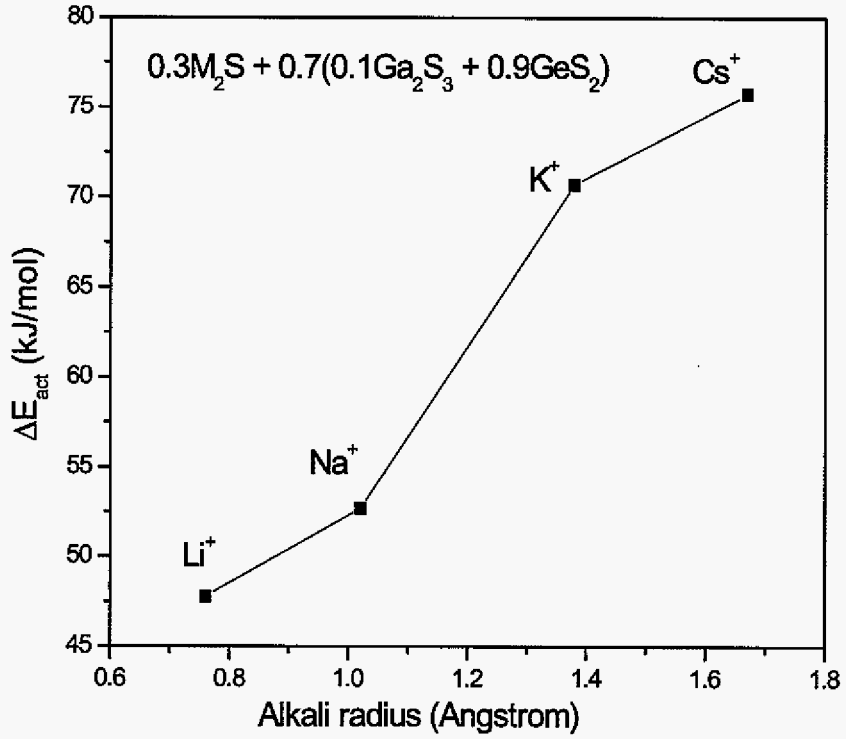
0.3M2S + 0.7(0.1Ga2S3 + 0.9GeS2)
Cs+
K+
Na+
Li+
ΔEact (kJ/mol)
Alkali radius (Angstrom)
80
75
70
65
60
55
50
45
0.6
0.8
1.0
1.2
1.4
1.6
1.8

Figure 3- 6

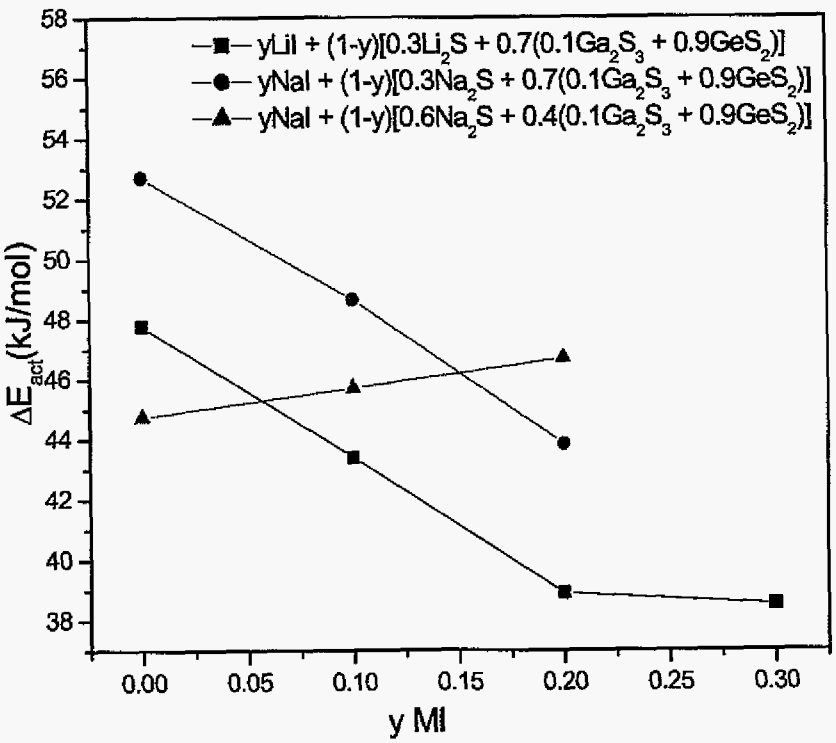
yLiI + (1-y)[0.3Li2S + 0.7(0.1Ga2S3 + 0.9GeS2)]
yNaI + (1-y)[0.3Na2S + 0.7(0.1Ga2S3 + 0.9GeS2)]
yNaI + (1-y)[0.6Na2S + 0.4(0.1Ga2S3 + 0.9GeS2)]
ΔEact(kJ/mol)
58
56
54
52
50
48
46
44
42
40
38
0.00
0.05
0.10
0.15
0.20
0.25
0.30
y MI

Figure 3- 7

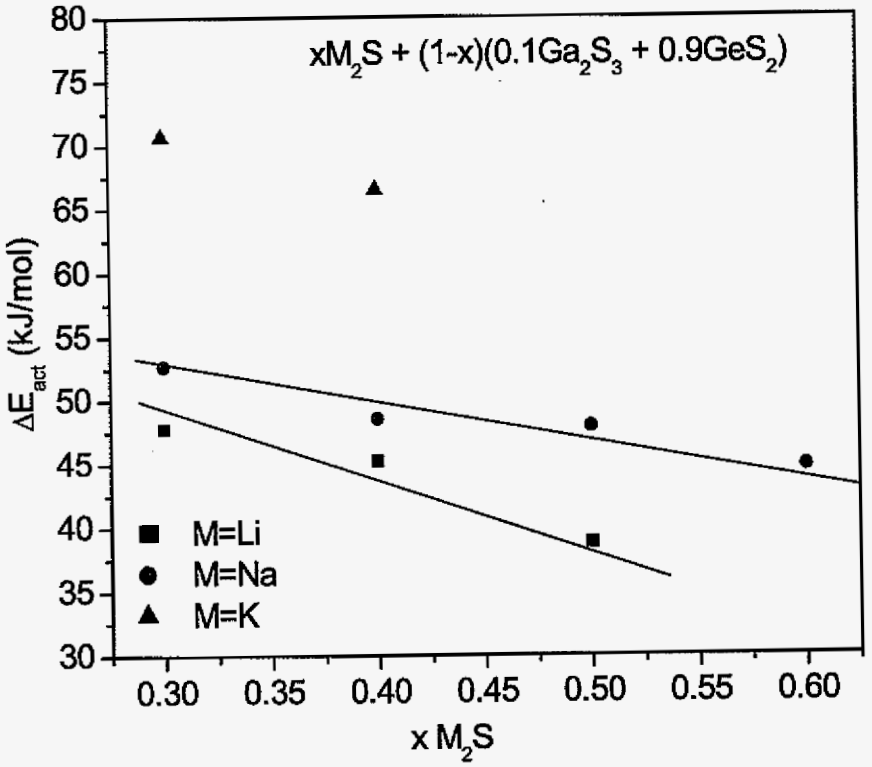
xM2S + (1-x)(0.1Ga2S3 + 0.9GeS2)
ΔEact (kJ/mol)
80
75
70
65
60
55
50
45
40
35
30
M=Li
M=Na
M=K
0.30
0.35
0.40
0.45
0.50
0.55
0.60
x M2S

Figure 3- 8

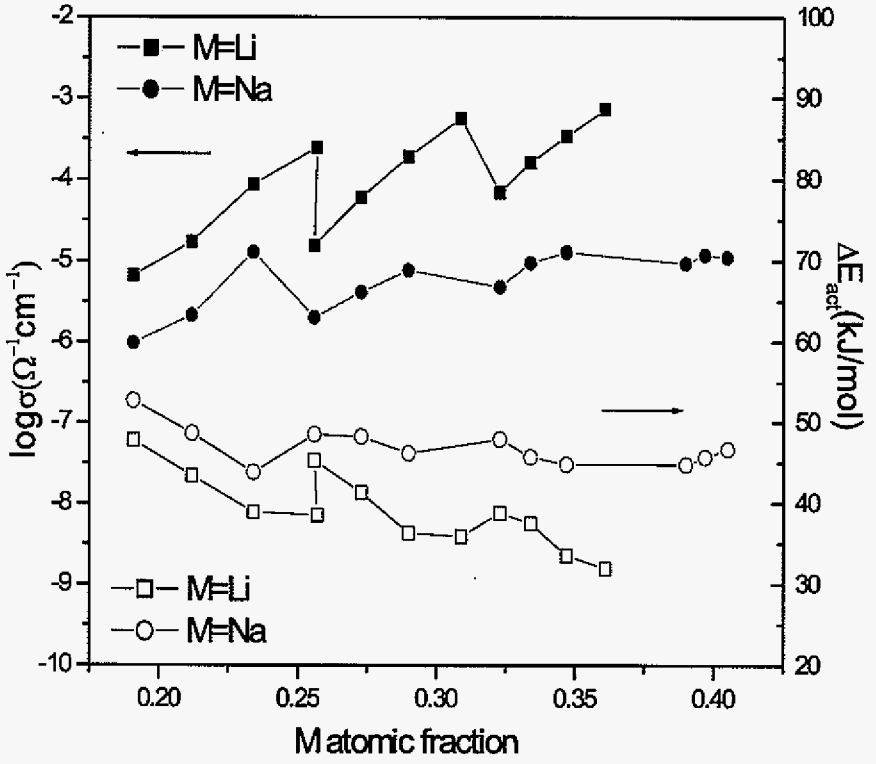
M=Li
M=Na
M=Li
M=Na
logσ(Ω⁻¹cm⁻¹)
ΔE_act(kJ/mol)
M atomic fraction
-2
-3
-4
-5
-6
-7
-8
-9
-10
100
90
80
70
60
50
40
30
20
0.20
0.25
0.30
0.35
0.40

Figure 3- 9

Table 3- 1

$yMI + (1-y)[xM_2S + (1-x)(0.1Ga_2S_3 + 0.9GeS_2)]$	x	y
M = Li	0.3-0.5	0-0.3
M = Na	0.2-0.67	0-0.2
M = K	0.3, 0.4	0-0.1
M = Cs	0.3, 0.4	0-0.1

Table 3- 2

$xM_2S + (1-x)(0.1Ga_2S_3 + 0.9GeS_2)$	ΔE_b Calc. (kJ/mol)	ΔE_s Calc. (kJ/mol)	ΔE_{act} Calc. (kJ/mol)	ΔE_{act} Exp. (kJ/mol)
M = Li, x = 0.3	24.8	9.7	34.5	47.78
M = Li, x = 0.4	21.2	8.6	29.8	45.26
M = Li, x = 0.5	18.2	7.9	26.1	38.77
M = Na, x = 0.3	20.9	24.6	45.5	52.7
M = Na, x = 0.4	17.9	22.3	40.2	48.52
M = Na, x = 0.5	15.4	20.5	35.9	47.9
M = Na, x = 0.6	13.0	19.2	32.2	44.75
M = Li, x = 0.3	24.8	9.7	34.5	47.78
M = Na, x = 0.3	24.6	20.9	45.5	52.7
M = K, x = 0.3	16.7	58.1	74.8	70.68
M = Cs, x = 0.3	13.7	95.3	109	75.72

3.8 References

[1] K.Takada, T.Inada, A.Kajiyama, M.Kouguchi, H.Sasaki, S.Kondo, Y.Michiue, S.Nakano, M.Tabuchi, M.Watanabe, Solid State Ionics 172 (2004) 25.

[2] C.Julien and G-A.Nazri, Solid State Batteries: Materials Design and Optimization,Kluwer Academic Publishers (1994).

[3] H. L.Tuller, D. P. Button, D. R.Uhlmann, Journal of Non-Crystalline Solids 40 (1980) 93.

[4] D.Ravaine, J. L.Souquet, Physics and Chemistry of Glasses 19 (5) (1977) 115.

[5] D.Ravaine, J. L.Souquet, Physics and Chemistry of Glasses 18 (2) (1977) 27.

[6] A.M.Glass, K.Nassau, Journal of Applied Physics 51 (7) (1980) 3756.

[7] M.D.Ingram, Philosophical Magazine B 60 (6) (1989) 729.

[8] O. L.Anderson, D. A.Stuart, Journal of the American Ceramic Society 37 (12) (1954) 573

[9] J. O Isard, K. K. Mallick, Solid State Ionics 21 (1) (1986) 7.

[10] M. J.Ryan, S. I.Smedley, Journal of Non-Crystalline Solids 65 (1984) 29.

[11] S. R.Elliott, Journal of Non-Crystalline Solids 172-174 (Pt. 2) (1994) 1343.

[12] Y. S.Tver'yanovich, V. V. Aleksandrov, I. V. Murin, E. G.Nedoshovenko, Journal of Non-Crystalline Solids 256&257 (1999) 237.

[13] P.Balaya, V.K.Shrikhande, G.P.Kothiyal, P.S Goyal,Current Science 86 (4) (2004) 553.

[14] M. D.Ingram, C. T.Moynihan, A. V.Lesikar, Journal of Non-Crystalline Solids 38-39 (1) (1980) 371.

[15] F. A. Fusco, H. L. Tuller, D. P.Button, Materials Science and Engineering B13 (1992) 157.

[16] D. P.Button, R. P. Tandon, H. L.Tuller, D. R.Uhlmann, Journal of Non-Crystalline Solids 42 (1980) 297.

[17] J. Kincs, S. W. Martin, Physical Review Letter 76 (1) (1996) 70.

[18] B. Meyer, F. Borsa, S. W. Martin, Journal of Non-Crystalline Solids 337 (2) (2004) 166.

[19] A.Pradel, N. Kuwata, M.Ribes, Journal of Physics: Condensed Matter 15 (16) (2003)

S1561.

[20] N. Chbani, A. Ferhat, A. M. Loireau-Lozac'h, J.Dugue, Journal of Non-Crystalline Solids 231 (3) (1998) 251.

[21] J. L. Souquet, E. Robinel, B. Barrau, M. Ribes, Solid State Ionics 3-4 (1981) 317.

[22] C. R. Nelson, S. A. Poling, S.W. Martin, Journal of Non-Crystalline Solids 337 (2004) 78.

[23] J.Saienga, Y. Kim, B. Campbell, S.W. Martin, Solid State Ionics 176 (2005) 1229.

[24] J. Cho, PhD thesis, Iowa State University (1995).

[25] S. A. Poling, S.W. Martin, J.T. Sutherland, US Patent Application Serial No. 10/627, 584(7-25-2003).

[26] M. A. Chad, PhD thesis, Iowa State University (2006).

[27] W. Yao, K. Berg, and S.W. Martin, to be submitted, (2006).

[28] S. W. Martin, C. A. Angell, Journal of Non-Crystalline Solids 83 (1-2) (1986) 185.

[29] E. F. Hairetdinov, N. F. Uvarov, H. K. Patel, S. W. Martin, Physical Review B: Condensed Matter 50 (18) (1994) 13259.

[30] H. K.Patel S. W. Martin, Physical Review B: Condensed Matter 45 (18) (1992) 10292.

[31] G.N.Greaves, K.L Ngai, Physical Review B: Condensed Matter 52 (9) (1995) 6358.

[32] D. K.McElfresh, D. G.Howitt, Journal of the American Ceramic Society 69 (10) (1986) C-237.

[33] Y. Kim, J. Saienga, S. W. Martin, Journal of Physical Chemistry B (In press), (2006).

4. Electrode Polarization and Determination of Mobile Carrier Density in Thiogermanate Glasses

A paper to be submitted to Journal of Physics: Condensed Matter

Wenlong Yao[1], Kyle Berger[1] and Steve Martin[1,2]

Abstract:

The electrode effect in fast ion conducting (FIC) thiogermanate glass during impedance spectroscopy measurements has been studied. The appropriate equivalent circuit including the electrode effect element was applied to fit the experimental impedance data. The replacement of Au with Cu leads to a higher low frequency dielectric constant. For the first time the mobile carrier density was determined based on the space charge polarization theory in FIC chalcogenide glasses. The mobile carrier density was found to be dependent on temperature for several of the composition glasses following an Arrhenius expression. The mobile carrier density increases with the increase of the temperature. The binding energy and strain energy were separated through temperature dependent of charge carrier number density and d.c conductivity for the first time. The mobile carrier density and mobility both are found to be important in determining the ionic conductivity.

4.1 Introduction

Solid state electrolytes have been extensively studied because of their potential application in high energy density, high performance batteries and fuel cells. Glassy electrolytes are isotropic, lack grain boundaries, are easily fabricated into complex shapes

[1] Department of Materials Science & Engineering, Iowa State University, Ames, IA 50011

[2] Author to whom correspondence should be directed

and have wide compositional flexibility to optimize the properties, showing their advantages on polycrystalline materials. Fast ion conducting (FIC) chalcogenide glasses have much larger ionic conductivities compared to oxide glass counterparts.

The fundamental equation to describe the temperature (T) dependence of the ionic conductivity is $\sigma(T) = n(T)eZ\mu(T)$, where n(T) is the temperature dependent number density of charge carriers, eZ is the charge of the carrier ion and μ(T) is the temperature dependent mobility [1]. The temperature dependence of n(T) and μ(T) are governed by the energy barrier ΔE_b, binding (or coulombic) energy, and ΔE_s, strain (or migration) energy, respectively. The total activation energy ΔE_{act} for σ(T) is therefore $\Delta E_b + \Delta E_s$. The Anderson-Stuart model gives the interpretation of the energy barriers for ionic conduction [2] based on the classical ideas of ionic crystal theory and elasticity theory. Furthermore, a structural interpretation of the two Anderson-Stuart model activation energy terms was given by Martin and Angell [3]. The binding energy ΔE_b needs to be overcome to dissociate the cation from non-bridging oxygen and strain energy ΔE_s is needed to dilate the interstitial from its initial radius to that of the mobile cation. However these models only provide order of magnitude approximations to the activation energies and cannot give accurate values to model the temperature dependence of the ionic conductivity σ(T). In practice, only the total activation energy ΔE_{act} can be obtained through temperature dependent ionic conductivity σ(T) measurements. In contrast to electronic conductors, whose charge carrier number density n(T) and mobility μ(T) can be separated by Hall effect and d.c conductivity measurements, the separation of these two terms in solid ionic conductors is very difficult because of the relatively low mobility of the mobile cations [4]. However, the separation of carrier density n(T) and mobility μ(T) can provide information for different glasses as a

function of composition, structure and temperature. Even the question of considering the ionic glass as strong electrolyte [5,6]or weak electrolyte [7-9] can be answered.

Many attempts have been made to separate the mobile carrier density n(T) and mobility μ(T) in ion conducting glass [7]. Recently it was found that space charge polarization can be used to determine the charge carrier density. The electrode polarization phenomena exist at the glass-electrode interface during the measurement of a.c impedance spectroscopy at low frequencies, which usually causes dramatically decreasing a.c conductivity and an increasing real dielectric constant with decreasing of frequency. The electrode polarization is dependent upon carrier number density, temperature, electrode materials, surface condition and sample thickness [10]. The space charge theory can satisfactorily explain the electrode polarization phenomena. Although the glass-electrode reaction is one cause for electrode polarization [11], only the space charge polarization leads to the electrode polarization under complete blocking electrode conditions.

Many theories of space charge polarization have been developed with the assumption of one type of mobile species in alkali silicate glasses and similar electrolytes. It was found that the model of Beaumont and Jacobs could be used to describe many features in the experimental data in glasses [12]. Macdonald's theory was extended to treat conductors that may have electrodes that are not completely blocking and the case where there may be more than one mobile carrier [13, 14]. His theory collapses to Beaumont and Jacobs' model under the condition of completely blocking electrodes and single carrier conductivities. Recently, the mobile carrier density has been determined in silica glass based on the model of Beaumont and Jacobs through the measurement of dielectric constant. Tomozawa and Shin studied dielectric relaxation in several types of silica glasses with variance sample

thicknesses and the carrier density was determined for one silica glass with different sample conditions, such as thickness, water content and fictive temperature [15]. Pitarch et al. studied the dielectric relaxation dependence upon bias voltage for one silica glass and the carrier density also was determined based on the model of Beaumont and Jacobs by means of Mott-Schottky capacitance-voltage characteristics. The obtained charge carrier density is lower by many orders of magnitude than the nominal alkali number density [16].

In this study, for the first time the charge carrier density of FIC chalcogenide glasses $xM_2S + (1-x)(0.1Ga_2S_3 + 0.9GeS_2)$, M = Li, Na and x = 0.3 to 0.6, were determined based on the model of Beaumont and Jacobs. The charge carrier density dependence on temperature was determined and the binding energy was obtained. Also the effect of different electrode material on the electrode polarization was studied with the use of two electrode materials, Au and Cu.

4.2 Experimental methods

4.2.1 Preparation of the glasses

All glass batching and melting operations were carried out in an oxygen- and water-free (< 5ppm) glove-box. High purity glassy GeS_2 was synthesized by the reaction of elemental germanium metal (Cerac, 99.999%) and sulfur (Alfa Aesar 99.999%) at high temperature (900 °C) in an evacuated silica ampoule[17]. Since high purity Na_2S is not commercially available, high purity NaSH was prepared by the reaction of NaOH and H_2S gas using Poling's methods[18]. The NaSH was decomposed to Na_2S and H_2S at elevated temperatures (~600 °C).

The MI + M_2S + ($0.1Ga_2S_3 + 0.9GeS_2$) (M = Li, Na) glasses were prepared by melting stoichiometric amounts of Ga_2S_3 (Alfa 99.99%), GeS_2, MI (LiI, Cerac 99%, NaI, Alfa 99.9%) and Li_2S (Alfa 99.9%) and NaSH between 870 °C and 920 °C for 6 mins. in vitreous carbon crucibles. The melt was quenched in a room-temperature brass mold. Weight loss measurements were done by removing the carbon crucible from the furnace after 3 mins. All weight losses due to evaporation were generally less than 5 wt. %. The bulk glass discs for impedance spectroscopy measurement were made by quenching the melt on a brass mold held at temperature 30 °C to 50 °C below the glass transition temperature (T_g), annealing at this temperature for half an hour and slow cooling (2 °C/min) to room temperature.

4.2.2 Impedance spectroscopy measurements

The bulk glass discs were carefully dry polished inside the glove box to 4000 grit using SiC polishing papers to improve the electrode and glass contact surface. The polished glass discs were then sputter coated with gold on both sides to form blocking electrodes for the impedance spectroscopy experiments. The sputtering, also performed inside the glove box, was performed at a pressure of 10^{-1} mbar of Argon with a current of 15 mA for a total of four minutes on each side. The sample thickness is ~ 1.5 mm to 2.5 mm and the sputtered electrode area is ~ 40.72 mm^2. A Cu target was also used to sputter copper electrode for our samples. The glass discs with sputtered electrode was put into an airtight sample chamber, which then was connected to a Solartron 1260 Impedance Gain-Phase Analyzer to measure the magnitude and phase angle of the impedance of the sample. The measurements were made by applying a sinusoidal voltage (50 mV) across the sample over a frequency range of 0.003 Hz to 10 MHz. While lower frequencies would have been preferred, the time required

for the measurements became exorbitantly long and unpractical for any significant number of measurements. The sample was put in a sample cell holder [19] and temperature was controlled from -60°C to 160°C within ±1°C depending on the different glasses.

4.3 Equivalent circuit

The processes considered during the impedance spectra study of an electrode-material system are so complicated that it is difficult to give a detailed physical-electrical model. So the impedance $Z_{cc}(\omega)$ from an equivalent circuit consisting of ideal resistors, capacitors, inductances and various distributed circuit elements was tried to approximate the experimental impedance data $Z_e(\omega)$. The physical interpretation can be given to these circuit elements.

The LEVM program developed by Macdonald et al. was used to fit the experimental data [20]. The O circuit of this program was chosen since this kind of circuit is found to fit many solid state conductive or dielectric materials [21-26]. The circuit in Figure 4-1, which is extracted from the O circuit in the LEVM program, can be used to fit the experimental impedance spectroscopy data well for solid state ionic conductors. The right part, called "bulk" part, consist of DE_1 and C_∞. The C_∞ is the dielectric constant at high frequencies and DE_1 is one distributed circuit element, stretched-exponential time response function, also known as Kohlrausch-Williams-Watts (KWW) function. The KWW response is frequently observed in many glasses and disorder materials and it is found that the KWW function is appropriate for many conductive systems, such as solid ionic conductors [21]. This part of the circuit can fit the experiment data at high frequencies, as shown in the Figure 4-2. Without considering the electrode effect, the bulk part can fit the high frequency region well.

The electrode polarization effect, which causes the spike in the complex impedance plot plane in Figure 4-2.a and dramatically increases the real dielectric constant as shown in Figure 4-2.b at low frequencies, can be well fitted by the left circuit part in Figure 4-1. The simplest model to present the electrode effect is a series capacitance, but the electrode effect is so complicated in the experimental impedance spectroscopy data that the left circuit part in Figure 4-1 was used to represent it. The DE_2 is another distributed circuit element, a series constant phase element (SCPE), where $\sigma_{sc}(\omega) = \varepsilon_0 A_{sc}(i\omega)^{\gamma_{sc}}, 0 \le \gamma_{sc} \le 1$, and A_{sc} is dielectric constant for a completely blocking series capacitance when $\gamma_{sc}=1$ and ε_0 is the dielectric constant in the free space. C_s is the blocking capacitance at low frequencies and C_1 is parallel to the SCPE to better model the electrode behavior. The use of CPE combining with capacitance has successfully modeled the electrochemical impedance spectroscopy data at low frequencies for many different disordered materials and can describe the space charge, diffusion in the electrode and rough surface electrode effect. So the circuit in Figure 4-1 can fit the experimental impedance spectroscopy data in the whole range of frequency in the studied samples.

4.4 Results and discussion

4.4.1 Thickness effect on dielectric constant

As observed in the silica glass measurement of Tomozawa [10], the similar features of the dielectric constant dependence of frequency also can be found in the studied glasses, shown in Figure 4-3. Figure 4-3.a shows the sample thickness dependence of the dielectric constant when the sample was polished very well. The dielectric constant spectra is dependent upon the sample thickness at low frequencies where the electrode effect begins to

occur and increases the dielectric constant significantly with the decrease of the frequency. At the lowest frequencies the larger the thickness is, the larger the dielectric constant. The two dielectric constant spectra will cross each other at a certain frequency. These features have been explained based on the space charge polarization for silica glass and also applicable to the studied chalcogenide glasses[10]. Figure 4-3.b also shows the sample thickness effect on the dielectric constant spectra but with the unpolished samples, which directly is obtained from annealing of the glass melt. Similar features are also observed but with a little difference at mid range of frequency. This may attribute to the different surface roughness.

Since the possible effect of thickness and surface roughness on the dielectric constant spectra, the following studies only consider the same thickness and polished condition samples and the same samples with different temperatures. So that only one factor will change and easy to understand the electrode effect behavior.

4.4.2 Effects of different electrodes on the dielectric constant

The two different kinds of electrodes, Au and Cu were used in the measurement of impedance spectroscopy for several samples. While for the $0.3Li_2S + 0.7(0.1Ga_2S_3 + 0.9GeS_2)$ glass, the stainless steel electrode was also used. Figure 4-4 shows the effects of different electrode on the dielectric constant at room temperature for $0.3Li_2S + 0.7(0.1Ga_2S_3 + 0.9GeS_2)$ glass. Similar to the thickness effect, the different electrode also shows significant difference at low frequencies. At lowest frequency, the glass with copper electrode has the highest dielectric constant, while the sample with stainless steel electrode shows the lowest dielectric constant and the dielectric constant of the sample with gold

electrode is between that of copper and stainless steel. For other samples with Au and Cu electrode, the significant feature in $0.3Li_2S + 0.7(0.1Ga_2S_3 + 0.9GeS_2)$ glass can be observed: the dielectric constant with copper electrode shows higher values than that of samples with gold electrode at low frequencies. The electrode effect on the measured dielectric constant depends on the reactivity of electrode to glass. The copper is thought to react with glass easily and in the experiment of impedance measurement, the impedance data begin to show obvious change from the last temperature after ~100 °C and after the measurement being finished around 200 °C. It was found that the copper on the surface is almost gone indicating that the copper completely reacts with the glass. For the gold electrodes, the gold is still intact after the high temperature measurement and suggests that the copper has a higher degree of reactivity with these glasses than does gold. The reaction with glass leads to the formation of Cu ions in the glass-electrode interface and at low frequency these ions form the space charge deposited at glass-electrode interface. Due to the higher reactivity of copper, the higher dielectric constant is observed at low frequency region than that of gold. Similar trends were also observed in silica glass for gold and silver electrode [27]. From Figure 4-4, stainless steel electrode shows higher stability to glass than gold and however with the increase of temperature, the dielectric spectra become bad. This may attribute to the thinness of stainless steel electrode film on the glass surface because the deposition rate of stainless steel in the sputter system is very low and thin film is easy to be removed by wiping. More work need to be done on stainless steel electrode work.

To understand well the electrode behavior in the glass-electrode interface which causes the different dielectric relaxation, impedance spectroscopy data of samples with Au and Cu were fitted with the circuit of Figure 4-1 in the LEVM program. The change of parameters

will show how the electrode materials can affect the electrode polarization behavior. As discussed in the above section, the A_{sc} is dielectric constant for a completely blocking series capacitance when γ_{sc}=1. So the A_{sc} is chosen as the dielectric constant at low frequency ε_s and its value is similar magnitude to the experimental data. From the left circuit of Figure 4-1, the C_s will probably represent the dielectric constant for a completely blocking series capacitance when the frequency reach zero. However in the process of experimental data fitting, it is found that to achieve the best fitting result, sometimes C_s and C_1 are not necessary in the circuit. Probably in the range of measured frequency the series constant phase element (SCPE) plays the most important role in the process of electrode polarization and it is expected that with including more low frequency range, the C_s will be important in the circuit and dielectric constant representing the C_s will be same magnitude to A_{sc}.

Table 4-1 gives the fitting parameters of A_{sc} and γ_{sc} of several composition samples with Au and Cu electrode. A_{sc} is the magnitude of the dielectric constant at lowest frequency and γ_{sc} is used to describe the shape change of the dielectric constant at low frequency region. From the Table 4-1, most of A_{sc} with copper electrode is larger than that of gold electrode, corresponding to the trend in the dielectric constant spectra at lowest frequency part. Instead the γ_{sc} with copper electrode is lower than that of gold electrode, which leads to the shape change of the dielectric constant spectra with different electrode. So the parameters of A_{sc} and γ_{sc} can be used to describe the change of dielectric constant spectra when the different electrodes are used in the measurement of impedance spectroscopy of materials.

4.4.3 Determination of mobile carrier density

The space charge polarization theory from Beaumont and Jacobs gives a frequency dependent dielectric constant function for the diffusion of single mobile cation in an ionic conductor system. This function relates to the sample base conductivity σ, thickness L, high frequency dielectric constant ε_∞, blocking factor ρ (ρ= 0 for completely blocking electrodes) and mobile carrier density n(T). When the zero frequency limit real dielectric constant ε_s is taken it can be given as:

$$\varepsilon_s = \varepsilon_\infty + \frac{2L\varepsilon_\infty}{(2+\rho)^2}\sqrt{\frac{n(T)e^2}{kT\varepsilon_0\varepsilon_\infty}}$$

Here T is the absolute temperature, e is the elementary charge and k is the Boltzmann constant. In this equation, the mobile carrier density n(T) is included so that the n(T) can be determined using this equation in the studied glass if other values are obtained in the experiments.

A blocking parameter ρ can be calculated from the conductivity using the below expression [15]:

$$\sigma_{sc} = \frac{\rho}{2+\rho}\sigma_{d.c.}$$

Where σ_{sc} is the d.c. conductivity at zero frequency caused by electrode polarization and $\sigma_{d.c.}$ is the d.c. conductivity of the glass. Actually it is found that $0 < \rho \ll 2$ in the studied glass indicating that nearly completely blocking electrode is applied in the experiment. So $\rho = 0$ is used in the calculation of n(T) for all glasses. As discussed in the above section, the obtained A_{sc} from fitting is used as ε_s and ε_∞ use the value of parameters C_∞ in the calculation.

The mobile carrier density n(T) dependent of temperature was calculated for several studied chalcogenide glass and Table 4-2 lists the n(T) of these glass at room temperature and also the nominal cation number density for these glass. The calculated n(T) is a few orders of magnitude lower than that of nominal cation number density and with the increase of temperature, the calculated n(T) is closer to the nominal number density. It indicates that our method of calculating n(T) is applicable to the studied glass.

The n(T) dependent of temperature is calculated for the same sample under the same condition. It is known that n(T) is determined by the binding energy ΔE_b through the function $n(T) = n_o \exp\left(\frac{-\Delta E_b}{RT}\right)$. So that the binding energy ΔE_b can be obtained by plotting the n(T) dependent of 1/T. Figure 4-5 shows the mobile carrier density n(T) and d.c conductivity dependent of 1/T for $0.3Li_2S + 0.7(0.1Ga_2S_3 + 0.9GeS_2)$ glass. Through linear fitting of the plot, the binding energy ΔE_b and the total activation energy ΔE_{act} can be calculated and obtained. The strain energy ΔE_s is obtained by subtracting the binding energy ΔE_b from the total activation energy ΔE_{act}. This way the separation of charge carrier number density and the mobility can be done with this method. Similarly the binding energy ΔE_b and the strain energy ΔE_s for other glasses were obtained in this study, list in Table 4-2.

It is better that if we can study the $0.3Li_2O + 0.7(0.1Ga_2O_3 + 0.9GeO_2)$ composition glass, the anion effect on the conductivity can be learned. However, it is difficult for us to get the $0.3Li_2O + 0.7(0.1Ga_2O_3 + 0.9GeO_2)$ composition glass due to its extreme high melting temperature. So the common ionic conductor glass $LiPO_3$ was studied and the same method is applied to get the charge carrier density n(T) and d.c conductivity dependent of 1/T and the different energy, shown in Figure 4-6 and Table 4-2. As expected, the $LiPO_3$ glasses were

found to have the lower carrier density than that of the sulfide glasses. This is attributed to the stronger bonding of lithium oxygen than lithium sulfur bonding, leading to the higher binding energy for $LiPO_3$ glasses as shown in Table 4-2.

The influence of charge carrier density and the mobility on the ionic conductivity is controversial due to the difficulty to separate the carrier density and mobility. The ionic conducting glass may act like strong electrolyte, where all charge carriers are dissociated and it is the mobility that determines the conductivity. Or it may act like a weak electrolyte where the charge carrier dissociation is limited and the dissociated carrier number density determines the conductivity. According to the space charge polarization theory of Beaumont and Jacobs, the real dielectric constant at zero frequency depends on the mobile carrier density n(T). So if the ionic conducting glass act like strong electrolyte, all the dissociated charge carriers will accumulate at glass-electrode interface and form the space charge leading to the electrode polarization effect when the frequency reaches to zero. In this case the real dielectric constant at zero frequency will be a constant value for all temperatures. When the ionic conducting glass acts as weak electrolyte, the real dielectric constant at zero frequency will increase with the increase of temperature. This is because the dissociated charge carrier density increases with the increase of the temperature. Actually, it is experimentally observed that the low frequency real dielectric constant increases when the temperature increases, as shown in Figure 4-7 and Figure 4-8 of $0.3Li_2S + 0.7(0.1Ga_2S_3 + 0.9GeS_2)$ and $LiPO_3$ glasses. All other studied glasses have similar trends in frequency dependent of the real dielectric constant with change of temperature. This behavior indicates that the studied glasses act as weak electrolyte. In the expression of conductivity $\sigma(T) = \frac{n_0 \mu_0 Ze}{T} \exp\left(\frac{-(\Delta E_b + \Delta E_s)}{RT}\right)$, it is

experimentally observed that the pre-exponent is similar for most of ionic conducting glass regardless of the composition change. The conductivity is determined by the value of the binding energy ΔE_b and the strain energy ΔE_s. So from the value of the binding energy ΔE_b and the strain energy ΔE_s for the studied glass in Table 4-2, it may mean that both mobile carrier density and mobility are important in determining the ionic conductivity in sulfide and oxide glasses.

4.5 Conclusions

For the first time the mobile carrier density is determined in the fast ionic conducting chalcogenide glass based on the space charge polarization theory. The calculated charge carrier number density close to the nominal cation number density indicates the capability of the current method. The replacement of Cu to Au leads to the higher dielectric constant at low frequency region. The binding energy and migration energy can be separated through temperature dependent of mobile carrier density and d.c conductivity. The charge carrier density and mobility both are important in determine the ionic conductivity.

To use the current method to determine the mobile carrier density precisely, more appropriate equivalent circuit and higher quality experimental data is required since the experimental data covers a wide range of frequency from 10^{-3} to 10^{7} Hz. Also highly polished and thinner sample helps to obtain good data and avoid too many factors considered in the electrode effect.

4.6 Acknowledgement

We are grateful to Dr. Klaus Funke and David Laughman (University of Muenster, Germany) for the measurement of $LiPO_3$ sample. This work is supported by National Science Foundation grant # DMR-0610813.

4.7 Captions

Figure 4-1 Appropriate equivalent circuit for solid ionic conductors, including the electrode effect element

Figure 4-2 A typical impedance spectroscopy data with electrode effect. (a) impedance complex plane plot. (b) frequency dependent real dielectric constant

Figure 4-3 Thickness effect on frequency dependent dielectric constant. (a) polished samples. (b) as annealed samples, unpolished

Figure 4-4 Effect of different electrode material on frequency dependent real dielectric constant

Figure 4-5 Temperature dependent charge carrier number density and d.c conductivity for $0.3Li_2S + 0.7(0.1Ga_2S_3 + 0.9GeS_2)$ glass

Figure 4-6 Temperature dependent charge carrier number density and d.c conductivity for $LiPO_3$ glass

Figure 4-7 Frequency dependent real dielectric constant change with the increase of temperature for $0.3Li_2S + 0.7(0.1Ga_2S_3 + 0.9GeS_2)$ glass

Figure 4-8 Frequency dependent real dielectric constant change with the increase of temperature for $LiPO_3$ glass

Table 4-1 The fitting parameters of A_{sc} and γ_{sc} of the studied glasses with different electrode

Table 4-2 The calculated charge carrier number density, nominal cation number density, total activation energy, binding energy and migration energy for the studied glass

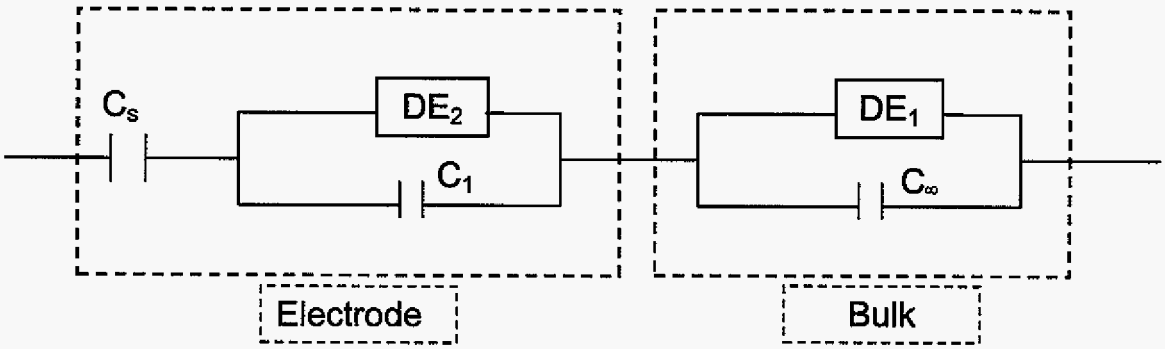

Figure 4- 1

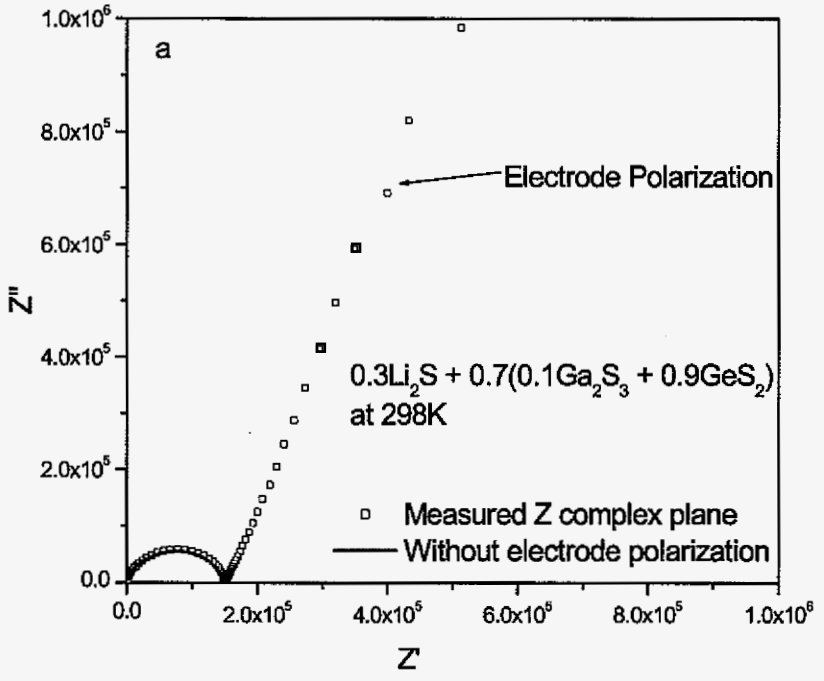
a
Electrode Polarization
0.3Li2S + 0.7(0.1Ga2S3 + 0.9GeS2)
at 298K
Measured Z complex plane
Without electrode polarization
Z''
Z'
1.0x10^6
8.0x10^5
6.0x10^5
4.0x10^5
2.0x10^5
0.0
0.0
2.0x10^5
4.0x10^5
6.0x10^5
8.0x10^5
1.0x10^6

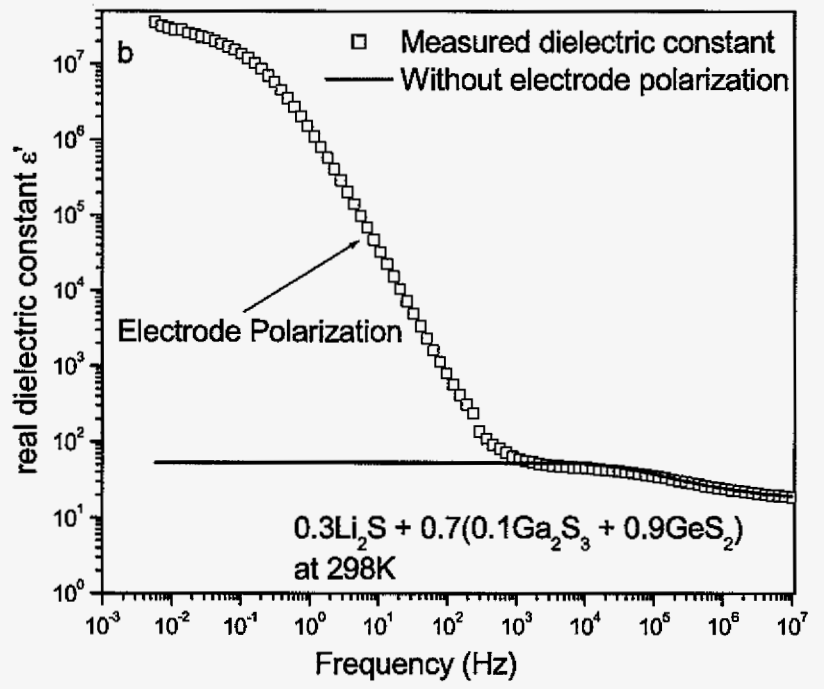
b
Measured dielectric constant
Without electrode polarization
Electrode Polarization
0.3Li2S + 0.7(0.1Ga2S3 + 0.9GeS2)
at 298K
real dielectric constant ε'
Frequency (Hz)
10^7
10^6
10^5
10^4
10^3
10^2
10^1
10^0
10^-3
10^-2
10^-1
10^0
10^1
10^2
10^3
10^4
10^5
10^6
10^7

Figure 4- 2

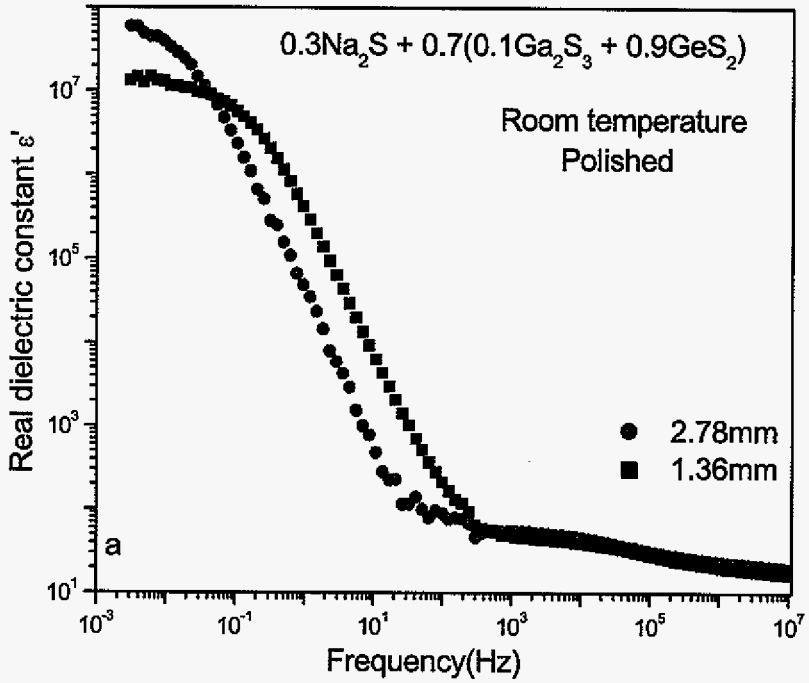
0.3Na2S + 0.7(0.1Ga2S3 + 0.9GeS2)
Room temperature
Polished
2.78mm
1.36mm
a
Real dielectric constant ε'
Frequency(Hz)

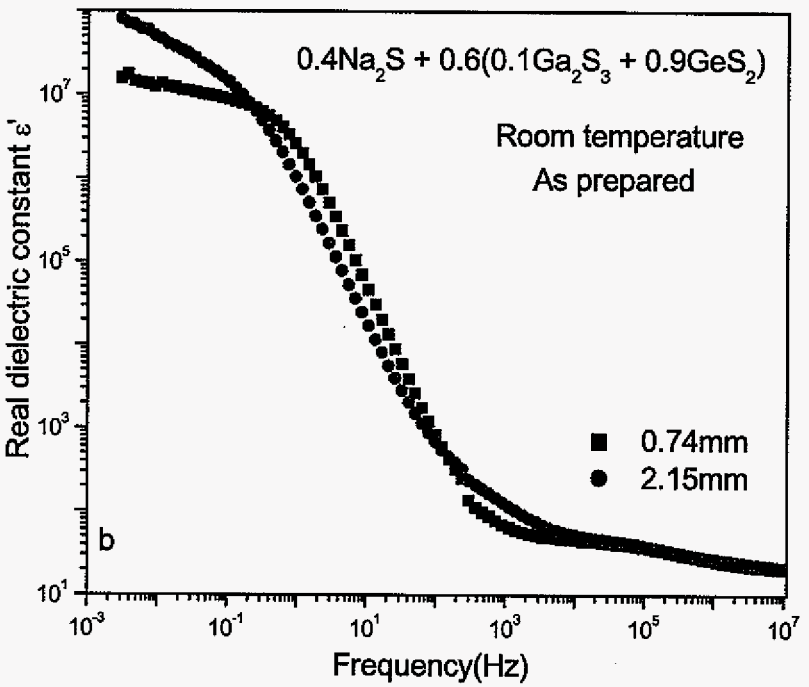
0.4Na2S + 0.6(0.1Ga2S3 + 0.9GeS2)
Room temperature
As prepared
0.74mm
2.15mm
b
Real dielectric constant ε'
Frequency(Hz)

Figure 4- 3

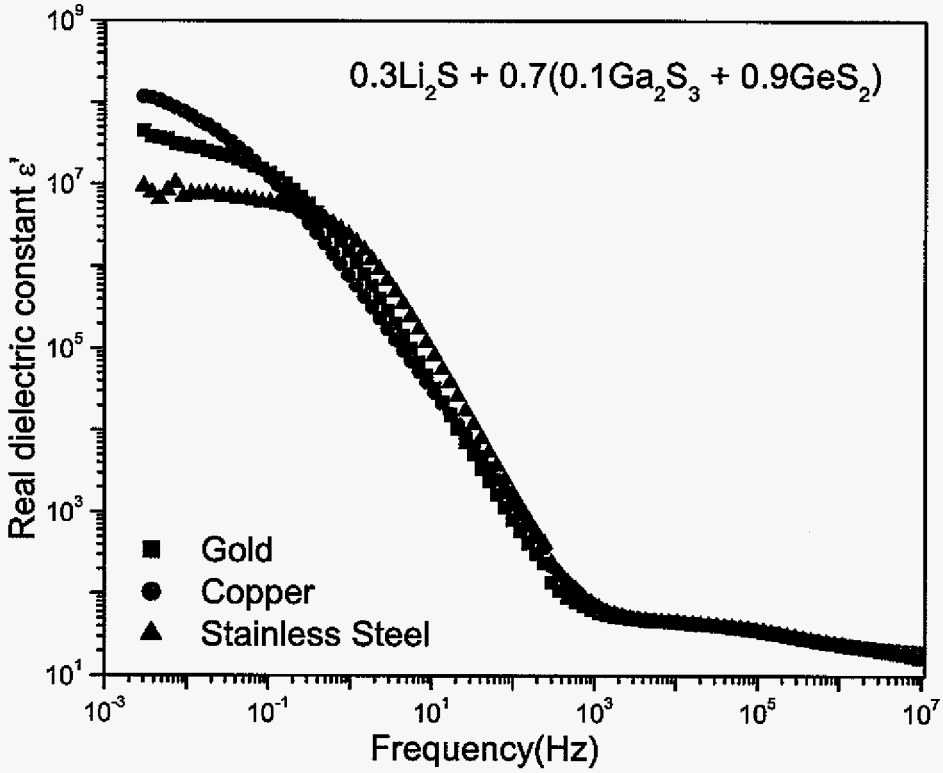
0.3Li2S + 0.7(0.1Ga2S3 + 0.9GeS2)
Real dielectric constant ε'
Frequency(Hz)
Gold
Copper
Stainless Steel
10^9
10^7
10^5
10^3
10^1
10^-3
10^-1
10^1
10^3
10^5
10^7

Figure 4- 4

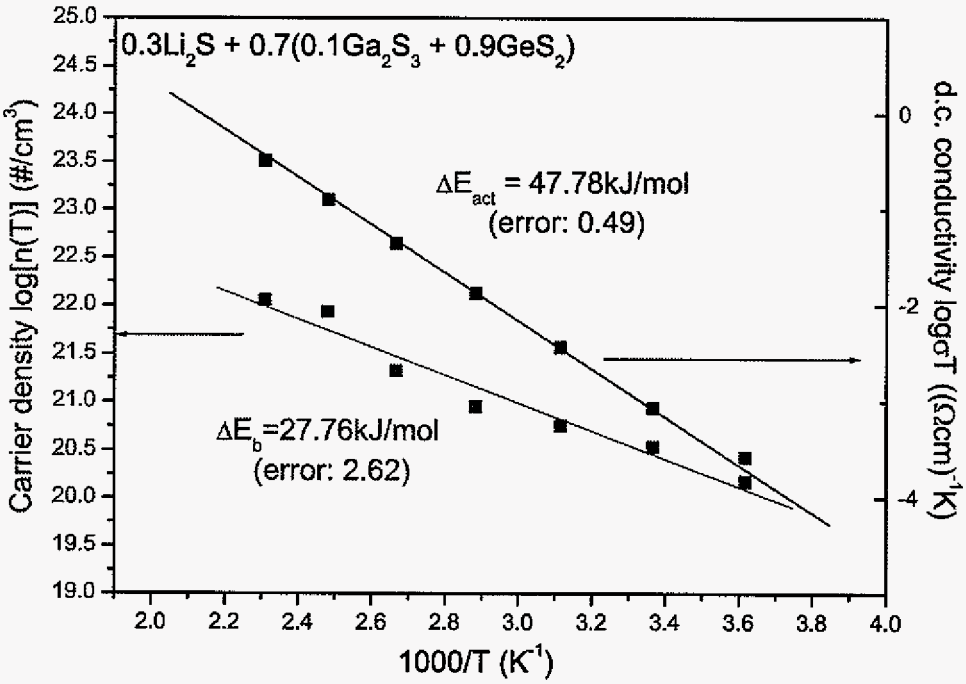
0.3Li2S + 0.7(0.1Ga2S3 + 0.9GeS2)
ΔEact = 47.78kJ/mol
(error: 0.49)
ΔEb=27.76kJ/mol
(error: 2.62)
Carrier density log[n(T)] (#/cm3)
d.c. conductivity logσT ((Ωcm)-1K)
1000/T (K-1)
25.0
24.5
24.0
23.5
23.0
22.5
22.0
21.5
21.0
20.5
20.0
19.5
19.0
0
-2
-4
2.0
2.2
2.4
2.6
2.8
3.0
3.2
3.4
3.6
3.8
4.0

Figure 4- 5

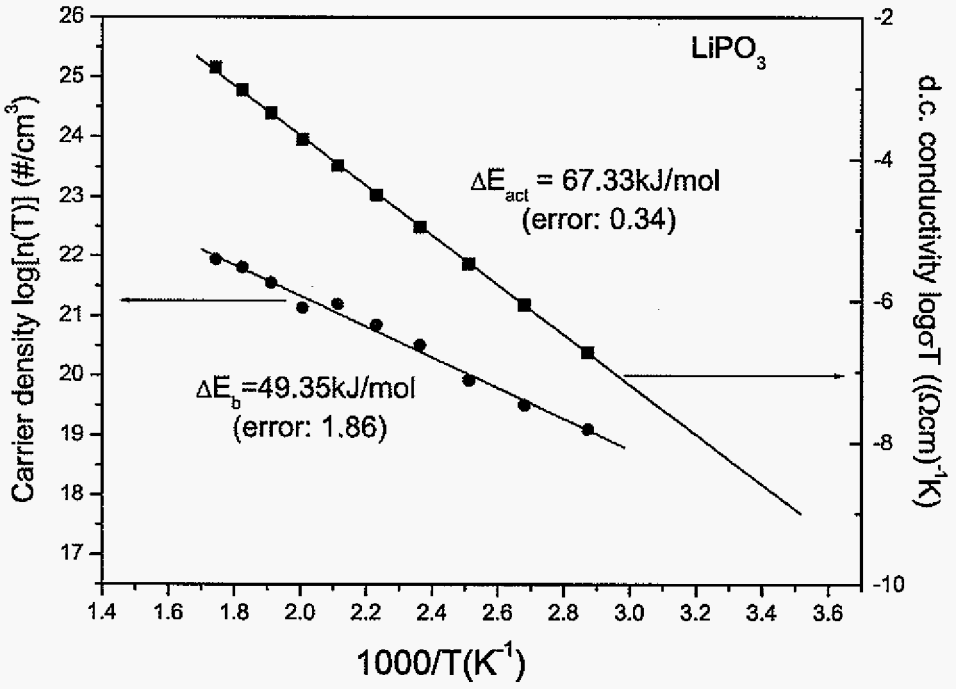
LiPO3
ΔEact = 67.33kJ/mol
(error: 0.34)
ΔEb=49.35kJ/mol
(error: 1.86)
Carrier density log[n(T)] (#/cm3)
d.c. conductivity logσT ((Ωcm)-1K)
1000/T(K-1)
26
25
24
23
22
21
20
19
18
17
-2
-4
-6
-8
-10
1.4
1.6
1.8
2.0
2.2
2.4
2.6
2.8
3.0
3.2
3.4
3.6

Figure 4- 6

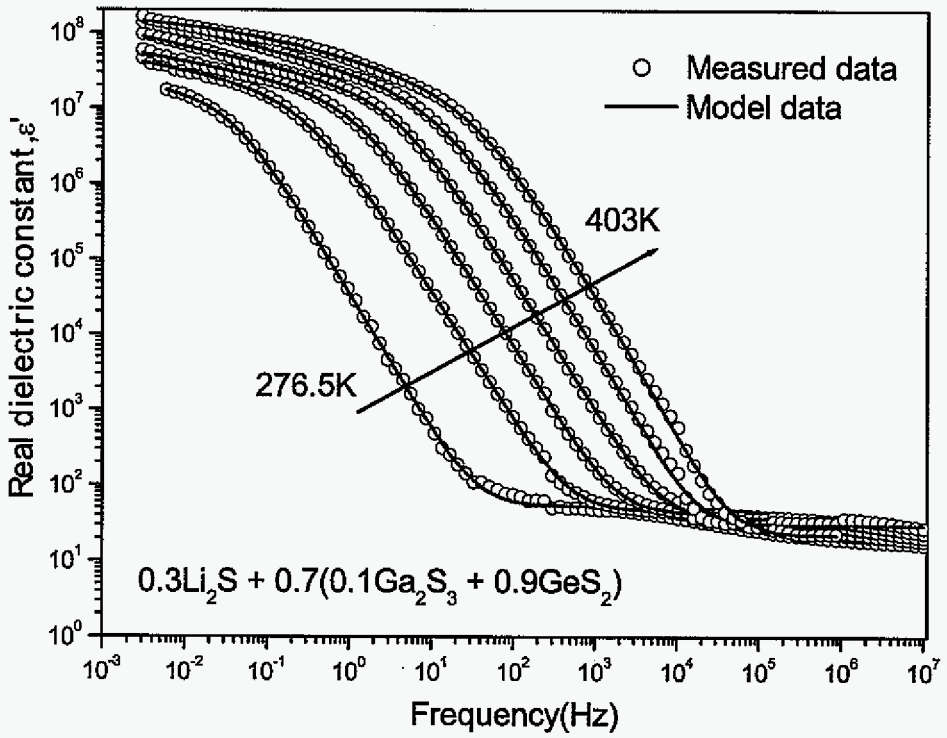
Measured data
Model data
403K
276.5K
0.3Li2S + 0.7(0.1Ga2S3 + 0.9GeS2)
Real dielectric constant,ε'
Frequency(Hz)

Figure 4- 7

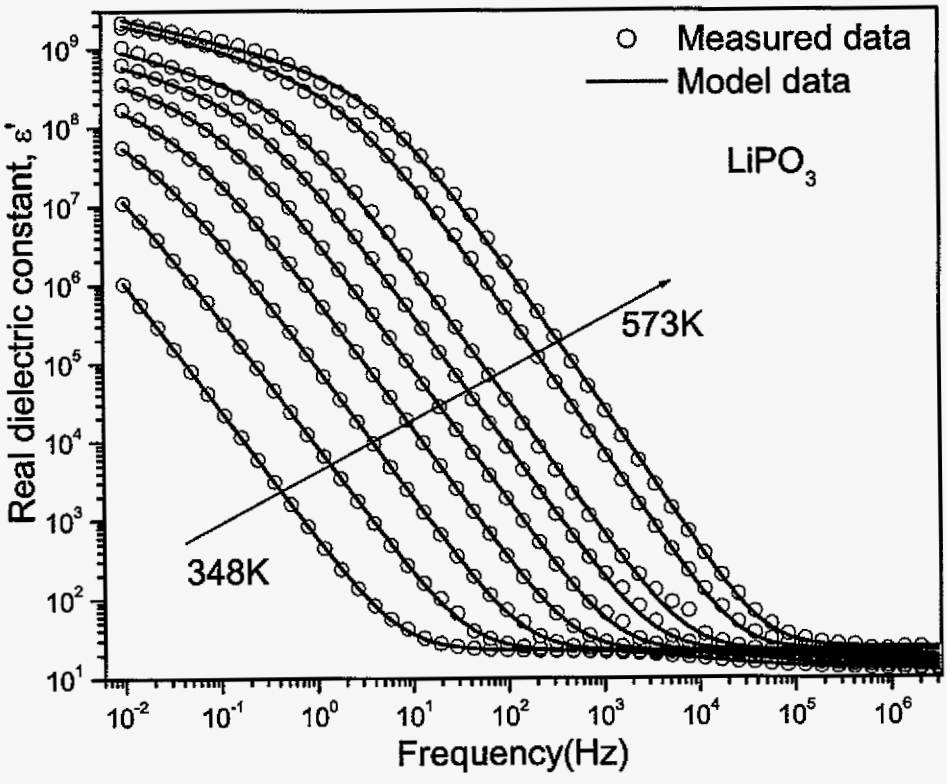
Measured data
Model data
LiPO3
573K
348K
Real dielectric constant, ε'
Frequency(Hz)
10^9
10^8
10^7
10^6
10^5
10^4
10^3
10^2
10^1
10^-2
10^-1
10^0
10^1
10^2
10^3
10^4
10^5
10^6

Figure 4-8

Table 4-1

Composition	A_{sc}	γ_{sc}
$0.3Li_2S + 0.7(0.1Ga_2S_3 + 0.9GeS_2)$ Au	2.2007E+07	7.1518E-01
$0.3Li_2S + 0.7(0.1Ga_2S_3 + 0.9GeS_2)$ Cu	4.0444E+07	4.9455E-01
$0.3Li_2S + 0.7(0.1Ga_2S_3 + 0.9GeS_2)$ Stainless steel	1.3011E+07	7.4817E-01
$0.5Li_2S + 0.5(0.1Ga_2S_3 + 0.9GeS_2)$ Au	1.8262E+07	7.0612E-01
$0.5Li_2S + 0.5(0.1Ga_2S_3 + 0.9GeS_2)$ Cu	3.4928E+07	4.0780E-01
$0.3Na_2S + 0.7(0.1Ga_2S_3 + 0.9GeS_2)$ Au	2.1649E+07	6.2308E-01
$0.3Na_2S + 0.7(0.1Ga_2S_3 + 0.9GeS_2)$ Cu	9.9120E+06	4.3893E-01
$0.5Na_2S + 0.5(0.1Ga_2S_3 + 0.9GeS_2)$ Au	1.0250E+07	7.5537E-01
$0.5Na_2S + 0.5(0.1Ga_2S_3 + 0.9GeS_2)$ Cu	2.1330E+07	6.0689E-01
$0.6Na_2S + 0.4(0.1Ga_2S_3 + 0.9GeS_2)$ Au	4.3162E+07	6.5864E-01
$0.6Na_2S + 0.4(0.1Ga_2S_3 + 0.9GeS_2)$ Cu	1.1931E+08	4.2582E-01

Table 4-2

Composition $xM_2S + (1-x)(0.1Ga_2S_3 + 0.9GeS_2)$	Calculated charge carrier number density (#/cm^3) 25°C	Nominal alkali number density (#/cm^3)	ΔE_{act} (kJ/mol)	ΔE_b (kJ/mol)	$\Delta E_s = \Delta E_{act} - \Delta E_b$ (kJ/mol)
M = Li, x = 0.3	6.73×10^{19}	8.75×10^{21}	47.78±0.49	27.78±2.62	20±2.62
M = Li, x = 0.5	3.86×10^{20}	1.62×10^{22}	38.77±0.22	27.99±2.16	10.78±2.16
M = Na, x = 0.3	1.22×10^{20}	7.85×10^{21}	52.7±0.46	22.31±2.91	30.39±2.91
M = Na, x = 0.4	4.58×10^{19}	1.07×10^{22}	48.52±0.61	31.91±5.14	16.61±5.14
M = Na, x = 0.5	3.79×10^{20}	1.36×10^{22}	47.9±0.42	34.39±4.73	13.51±4.73
M = Na, x = 0.6	2.70×10^{20}	1.67×10^{22}	44.75±0.45	27.34±7.22	17.41±7.22
$LiPO_3$	1.26×10^{19} (75°C)	1.65×10^{22}	67.33±0.34	49.35±1.86	17.98±1.86

4.8 References

[1] H. L.Tuller, D. P. Button, D. R.Uhlmann, Journal of Non-Crystalline Solids 40 (1980) 93.

[2] O. L. Anderson, D. A. Stuart, Journal of the American Ceramic Society 37 (12) (1954) 573.

[3] S. W. Martin, C. A. Angell, Journal of Non-Crystalline Solids 83 (1-2) (1986) 185.

[4] V. Clement, D. Ravaine, C. Deportes, R. Billat, Solid State Ionics 28-30 (Pt. 2) (1988) 1572.

[5] E. F. Hairetdinov, N. F. Uvarov, H. K. Patel, S. W. Martin, Diffusion and Defect Data, Pt.B 39-40 (Systems with Fast Ionic Transport - IV) (1994) 289.

[6] B.Roling, A. Happe, K. Funke, M. D. Ingram, Physical Review Letter 78 (11) (1997) 2160.

[7] D.Ravaine, J. L. Souquet, Physics and Chemistry of Glasses 18 (2) (1977) 27.

[8] D.Ravaine, J. L. Souquet, Physics and Chemistry of Glasses 19 (5) (1977) 115.

[9] A. Kone, J. L. Souquet, Solid State Ionics 18-19 (1) (1986) 454.

[10] C. Kim, M. Tomozawa, Journal of the American Ceramic Society 59 (3-4) (1976) 127.

[11] S. P. Mitoff, R. J. Charles, Journal of Applied Physics 43 (3) (1972) 927.

[12] J. M. Beaumont, P. W. Jacobs, Journal of Physics and Chemistry of Solids 28 (1967) 657.

[13] J.R. Macdonald, The Journal of Chemical Physics 58 (11) (1973) 4982.

[14] J. R. MacDonald, The Journal of Chemical Physics 29 (6) (1958) 1346.

[15] M. Tomozawa, D. W. Shin, Journal of Non-Crystalline Solids 241 (2,3) (1998) 140.

[16] A.Pitarch, J.Bisquert, G.Garcia-Belmonte, Journal of Non-Crystalline Solids 324 (1-2) (2003) 196.

[17] J.Cho, PhD thesis, Iowa State University (1995).

[18] S. A. Poling, S.W. Martin, J.T. Sutherland, US Patent Application Serial No. 10/627, 584(7-25-2003).

[19] S. A. Jeremy, PhD thesis, Iowa State University (2001).

[20] E. Barsoukov, J.R. Macdonald, Impedance Spectroscopy:theory, experiment, and applications,John Wiley & Sons, Inc (2005).

[21] J. R. Macdonald, Journal of Non-Crystalline Solids 212 (1997) 95.

[22] J. R. Macdonald, Journal of Non-Crystalline Solids 210 (1997) 70.

[23] J. R. Macdonald, Journal of Chemical Physics 116 (8) (2002) 3401.

[24] J. R. Macdonald, Journal of Physics: Condensed Matter 17 (2005) 4369.

[25] J. R. Macdonald, Journal of Non-Crystalline Solids 307-310 (2002) 913.

[26] J. R. Macdonald, Journal of Non-Crystalline Solids 197 (1996) 83.

[27] C. Kim, M. Tomozawa, Journal of the American Ceramic Society 59 (7-8) (2006) 321.

5. Structure Determination of Low-alkali-content $Na_2S + B_2S_3$ Glasses using Neutron and Synchrotron x-ray Diffraction

A paper published in Journal of Non-Crystalline Solids[1]

Wenlong Yao[2], Steve W. Martin[2,3], Valeri Petkov[4]

Abstract:

The structures of low-alkali-content $Na_2S + B_2S_3$ ($x \leq 0.2$) glasses have been studied by neutron and synchrotron x-ray diffraction. Similar results were obtained both in neutron and synchrotron x-ray diffraction experiments. One significant difference, however, is that with the high resolution obtainable in the x-ray atomic distribution function data, the peak at 1.8 Å splits into two components, one at 1.8 Å and one at 1.93 Å with the addition of Na_2S to B_2S_3. The experimental total atomic distribution functions have been compared to model ones computed on the basis of structure data for crystalline counterparts of the glasses. The results provide direct structural evidence that doping B_2S_3 with Na_2S creates a large fraction of tetrahedrally coordinated borons in the glass.

PACS: 61.12.Ex; 61.10.Eq; 61.43.Fs

5.1 Introduction

As a strong glass-forming material, boron trisulfide (B_2S_3) makes an excellent network glass former [1]. Recent interest in thioborate and related chalcogenide glasses is due to their fast ion conducting (FIC) behavior when suitably doped with alkali sulfide (M_2S) modifier and

---

[1] Reprinted with permission of Journal of Non-Crystalline Solids, 351, (2005), 1995-2002.

[2] Department of Materials Science & Engineering, Iowa State University, Ames, IA 50011

[3] Author to whom correspondence should be directed

[4] Department of Physics, Central Michigan University, Mt. Pleasant, MI 48859

considered as solid state electrolytes in solid state batteries [2, 3]. To optimize their electrical properties, it is important to fully understand their short-range order structure and model their FIC conductivity.

The atomic arrangement in vitreous B_2S_3 has been previously studied by Raman spectroscopy, ^{11}B NMR and neutron diffraction. Two sharp lines in the Raman spectra of v-B_2S_3 are interpreted as arising from B_3S_3 six-membered rings and B_2S_2 four-membered rings [4, 5]. Thus, the existence of similarities between the structure of glassy and crystalline B_2S_3 have been suggested. For reference, the structure of crystalline B_2S_3 is comprised of layers of planar B_3S_3 and B_2S_2 rings linked by sulfur bridges [6] as shown in Figure 5-1. Neutron diffraction on vitreous B_2S_3 provides evidence for the existence of B_3S_3 six-membered rings in the glass [7], but no direct evidence could be found for the existence of four-membered rings in v-B_2S_3. Thus details of the atomic ordering in B_2S_3 glass are still not fully known. Similarly, ^{11}B MASS NMR experiments of v-B_2S_3 show strong evidence for ~75% of the B residing in six membered thioboroxyl rings and 25% of the B residing in isolated "loose" trigonal units [8]. Such a structure is apparently identical to that of v-B_2O_3 where a similar fraction of boroxyl rings and loose trigonal units has also been observed in both neutron and NMR data [9, 10].

Boron trisulfide forms binary glasses over wide composition ranges when modified by alkali sulfide [11]. Notable structural differences exist between alkali thioborate and alkali borate glasses even though they have stoichiometric similarities [12]. With the addition of alkali sulfide to boron trisulfide , previous spectroscopic studies, such as infrared, Raman and NMR spectra [8, 12-17], show that the overall evolution of the structure is from $BS_{3/2}$ trigonally bonded boron groups to $BS_{4/2}$ tetrahedrally bonded boron groups in the low alkali glasses ($x < 0.3$). For the high alkali glass ($x > 0.5$), the tetrahedral boron units are then converted to trigonal boron units

with increasing fractions of non-bridging sulfurs such as $MSBS_{2/2}$, $(MS)_2\ BS_{1/2}$ and $(MS)_3B$, where M is an alkali metal. Significant differences, however, must exist in the short range structure of the different alkali thioborate glasses because NMR studies of the composition dependence of the fraction of tetrahedral borons in these glasses show marked differences in the number of tetrahedral borons that are created per added alkali metal. In $Na_2S + B_2S_3$ glasses, for example, each added Na_2S unit is found to create ~8 tetrahedral borons compared to the stoichiometric expected value of 2 which is observed in the analogous $Na_2O + B_2O_3$ oxide glass system. Surprisingly though, as the mass of the alkali metal increases, so the formation rate of tetrahedral borons decreases; K_2S creates 4-6 tetrahedral borons, Rb_2S creates 2-3 tetrahedral borons, and finally Cs_2S creates the expected value of 2 tetrahedral borons per added alkali metal sulfide unit. While the $Li_2S + B_2S_3$ compositions phase separate in the low alkali range and therefore cannot be formed into homogenous glasses, the high alkali range glasses ($x > 0.5$) must fit this pattern because they exhibit the highest fraction of tetrahedral borons of all the alkali thioborate glasses [18]. The phase separation in the low alkali lithium thioborate glasses may be a result of the extreme formation rate of tetrahedral borons producing incompatible structures.

At this point, there appears to be little detailed understanding of why the thioborate glasses exhibit such alkali-dependent rates of formation of tetrahedral borons. One possible reason is the formation in the glass of anion complexes, such as $B_{10}S_{18}^{6-}$, where every boron is in tetrahedral coordination and a high fraction of the sulfurs exhibit three-fold coordination [15]. A verification of this hypothesis by diffraction studies is worthwhile. However, diffraction studies on alkali modified thioborate glasses are very scarce. The only known neutron diffraction study has been performed on high alkali $xLi_2S + (1\text{-}x)\ B_2S_3$ ($x > 0.5$) glasses [19].

In this paper, therefore, both neutron and synchrotron x-ray diffraction have been performed on low-alkali-content $xNa_2S + (1-x)\ B_2S_3$ ($x \leq 0.2$) glasses where $BS_{3/2}$ units are converted to $BS_{4/2}$ units at a high conversion rate. We find direct structural evidence for the existence of such a structural transformation. A comparison between the experimental diffraction data with model ones computed from crystalline structures of similar chemical composition shows that the emerging $BS_{4/2}$ units are likely to form highly organized anion complexes.

The complimentary use of both neutron and x-ray diffraction allows us to gain insight on important details in the structure of the glasses. For example, while the B-B correlation is strong in the neutron diffraction data, these same correlations are hardly seen in the x-ray diffraction experimental data. On the contrary, the S-S correlations appear strong in the x-ray diffraction data and are much weaker in the neutron diffraction data. These differences will be used to obtain a clearer and more consistent understanding of the atomic ordering in thioborate glasses.

5.2 Structural determination of glasses using neutron and x-ray diffraction

The atomic-scale structure of glasses is usually described in terms of atomic pair distribution functions (PDF). The widely used atomic PDF, G(r), is defined as $G(r)=4\pi r[\rho(r)-\rho_o]$, where $\rho(r)$ and ρ_o are the local and average atomic number densities, respectively. G(r) peaks at real space distances where the most frequent interatomic distances occur and thus reflects the structure of material. The stronger the disorder in a glassy material the weaker the correlations between the positions of the atoms in it and, hence, the lower the number of well-defined peaks in the PDF. Thus by obtaining an experimental atomic PDF and analyzing the location, intensity and width of peaks one can obtain information about the atomic arrangement in the glass under study. The final stage of the analysis usually involves computer simulations and comparisons between model and experimental PDF data. A structure model that reproduces

well the experimental PDF data is considered to give a representative picture of the 3-D atomic arrangement in the glassy material.

Atomic PDFs can be obtained from neutron or x-ray diffraction experiments. A PDF is computed from the diffraction data via a Fourier transformation as follows

$$G(r) = (2/\pi) \int_{Q=o}^{Q_{max}} Q\,[S(Q) - 1] \sin(Qr)\, dQ\,, \qquad \text{Equation 5-1}$$

where Q is the magnitude of the wave vector ($Q=4\pi\sin\theta/\lambda$), 2θ is the angle between the incoming and outgoing radiation, λ is the wavelength of the radiation used and S(Q) is the so-called experimental total structure function. The structure function is related to the elastic part of the diffracted intensities, $I^{el.}(Q)$, as follows:

$$S(Q) = 1 + \left[I^{el.}(Q) - \sum c_i \left| f_i \right|^2 \right] / \left| \sum c_i f_i \right|^2, \qquad \text{Equation 5-2}$$

where c_i is the atomic concentration, and f_i is the x-ray or neutron scattering amplitude, respectively, for the atomic species of type i. It should be noted that for a material comprising n atomic species a single diffraction experiment yields an atomic PDF G(r) that is a weighted sum of $n(n+1)/2$ partial PDFs, $G_{ij}(r)$, each giving the spatial ordering of a particular i-j type atomic pair i.e.

$$G(r) = \sum_{i,j} w_{ij} G_{ij}(r) \qquad \text{Equation 5-3}$$

where $\sum_{i,j} w_{ij} = 100\%$. Here w_{ij} are weighting factors reflecting the relative abundance and scattering power of the atomic pairs of type i-j as follows:

$$w_{ij} = c_i c_j f_i f_j \,/ \left| \sum c_i f_i \right|^2, \qquad \text{Equation 5-4}$$

Table 5-1 lists the neutron and x-ray weighting factors for the $xNa_2S + (1-x)\ B_2S_3$ ($x \leq 0.2$) glasses studied here. Both the neutron scattering lengths and the atomic form factors were obtained from Sears [20] and Hubbell [21]. As can be seen from this table, the neutron diffraction data will be expected to reflect mostly B-B and B-S atomic correlations while the x-ray diffraction data will reflect the S-S and B-S correlations. Thus employing a combination of x-ray and neutron diffraction will better reveal all of the interatomic correlations between the majority atomic species in the glasses under study.

5.3 Experimental

5.3.1 Preparation of the glasses

High purity ν-B_2S_3 was synthesized in our laboratory following the method developed by Martin and Bloyer [1]. Stoichiometric amounts of amorphous boron powder (Cerac, 99.9%) and crystalline sulfur (Alfa, 99.999%) were reacted under vacuum at 800^0C in sealed, carbon-coated silica tubes in a furnace rotating at 6 rpm. ^{11}B is used in the neutron scattering experiment since ^{10}B has a large neutron absorption. So isotopically enriched ^{11}B powder (Eagle-Picher, 99.51% ^{11}B) instead of naturally abundant boron powder was used to prepare ν-$^{11}B_2S_3$.

The $xNa_2S + (1-x)^{11}B_2S_3$ ($x \leq 0.2$) glasses were prepared by melting stoichiometric amounts of Na_2S and B_2S_3 at 850^0C for ~10-15 mins. in vitreous carbon crucibles in a high-quality O_2- and H_2O-free (<10 ppm) glove box. The melt was quenched to room temperature between brass plates.

5.3.2 Neutron diffraction experiments

Time-of-flight neutron diffraction experiments were performed at room temperature. Powdered $xNa_2S + (1-x)^{11}B_2S_3$ (x=0, 0.1, 0.15 and 0.2) glasses were sealed in cylindrical

vanadium containers and measured on the GLAD diffractometer at the Intense Pulsed Neutron Source (IPNS) at the Argonne National Laboratory. The data analysis followed standard procedures and included corrections for the background, scattering from the containers, absorption, multiple scattering, inelasticity effects and incoherent scattering. The background, a standard vanadium rod, and the empty vanadium sample container were also measured to enable these corrections. It was found that there was about 1% hydrogen in the glass samples presumably in the form of B-S-H groups due to the hygroscopic character of B_2S_3. Because of the large incoherent scattering cross section of hydrogen, a standard method of hydrogen correction was performed. These were performed using the ATLAS software package for time-of-flight neutron diffraction data [22].

5.3.3 Synchrotron x-ray diffraction experiments

Synchrotron x-ray diffraction experiments were carried out at the BESSRC-CAT 11-ID-C beam line at the Advanced Photon Source (APS) at the Argonne National Laboratory. Three samples $xNa_2S + (1-x)B_2S_3$ (x = 0, 0.15, and 0.2) sealed in thin glass capillaries were measured. The measurements were done with x-rays of energy 114.67 keV (λ = 0.1081 $Å^{-1}$). The higher energy x-rays were used to extend the range of diffraction data (i.e. to obtain data at higher wave vectors $Q=4\pi\sin\theta/\lambda$), which is important to obtain improved resolution in the real-space of atomic pair distribution function (PDF) analysis, especially at short distances. Also, it helped reduce some unwanted experimental artifacts such as absorption and multiple scattering. Scattered radiation was collected with an intrinsic germanium detector coupled to a multi-channel analyzer. Several runs were conducted and the resulting XRD patterns were averaged to improve the statistical accuracy and to reduce any systematic effect due to instabilities in the

experimental setup. The experimental diffraction data were subjected to appropriate corrections for flux, background, Compton scattering, and sample absorption using the program RAD [23].

5.4 Results

5.4.1 Structure data from neutron diffraction

Figure 5-2 shows the reduced neutron structure function Q[S(Q)-1] for the four different compositions of $Na_2S + B_2S_3$ glasses that were studied. Although each data set was collected for approx. 12 h the reduced structure functions appear somewhat noisy due to relatively low flux of neutrons and the low scattering power of the samples. Also, although neutron diffraction data was collected to wave vectors as high as 40 $Å^{-1}$ the noise rendered the data above wave vectors of 16 $Å^{-1}$ unusable. This resulted in appreciable termination ripples in the corresponding atomic distribution functions. Nevertheless, as will be shown below, the neutron diffraction data are of quality good enough to reveal the details in the atomic ordering in the studies glasses.

The general features of the experimental data for the four glasses are fairly similar with the differences being mostly in the first peak at about 1.3$Å^{-1}$, which is the so-called first sharp diffraction peak (FSDP). The first peak changes greatly with the increase of Na_2S content, decreasing in intensity and shifting slightly to lower Q. The FSDP is regarded as a signature of medium-range order (MRO) in amorphous solids and its appearance in these glasses suggests that the addition of Na_2S significantly modifies the MRO in the B_2S_3 network [24]. Such trends in the FSDP with composition have also been reported previously in other glasses [25-27].

5.4.2 Atomic PDF function G(r) from neutron diffraction

The structure functions of Figure 5-2 were Fourier transformed to give the atomic pair distribution functions (PDF, G(r)) using a Lorch modification function with Q_{max} = 16 $Å^{-1}$, and

are shown in Figure 5-3 for all glasses studied. With increasing Na_2S contents, the intensity and position of peaks change slightly.

The peak at 1.83 Å is assigned to the B-S correlation in trigonally bonded $BS_{3/2}$ boron groups. This value is close to the first B-S distance in *c*-B_2S_3, where the first B-S distance varies between 1.778 Å and 1.838 Å in both B_2S_2 four-membered and B_3S_3 six-membered rings, respectively [6]. Also, this distance is very close to that obtained from previous neutron diffraction for pure *v*-B_2S_3 and $Li_2S + B_2S_3$ glasses [7, 19]. With the addition of Na_2S, the first B-S correlation shits slightly to larger distances. This may be due to the conversion from trigonally coordinated boron units to tetrahedrally coordinated boron units. The B-S distance in tetrahedrally bonded boron groups is found to vary between 1.879 Å to 1.951 Å [28]. Hence, the observed shift in the first PDF peak is consistent with the formation of tetrahedral boron in these low alkali glasses.

The peak at 2.98 Å is attributed to both B-B and S-S correlations because of their similar weighting factors and distances. The B-B distance in six-membered rings in the crystalline form of B_2S_3 is 2.94 Å and S-S distance varies between 3.06 Å and 3.26 Å [6]. Table 1 show that the weighting for the S-S distance is relative low, but with the increase of Na_2S, the relative weighting for the S-S correlation increases. This is reflected in the neutron data where the peak shifts slightly to larger distances.

It should be mentioned that the first PDF peak shows a low-r shoulder at a distance at 1.37 Å. The shoulder may arise from a small amount of B-O correlations coming from contamination of the commercial Na_2S with oxygen. The B-O bond length is identified as being 1.37 Å to 1.38 Å in previous studies of B_2O_3 glasses [29].

5.4.3 Structure data from synchrotron x-ray diffraction

Figure 5-4 shows the x-ray experimental reduced structure function for B_2S_3 glass and B_2S_3 glasses doped with Na_2S. The structure functions show noticeable oscillations up to the wave vector of 25 $Å^{-1}$ achieved in the present experiments. Like the neutron data, a careful inspection of the structure functions presented in Figure 5-4 shows that the first peak undergoes a dramatic change with Na_2S content: it is seen at ~ 2 $Å^{-1}$ in pure B_2S_3 and almost ceases to exist in the $0.20Na_2S + 0.80B_2S_3$ glass. This observation indicates that a considerable change in the immediate-range atomic order occurs as Na_2S enters the B_2S_3 network. This trend agrees well with that of the present neutron and previous results [25-27]. The higher-Q peaks in the experimental structure factors are also seen to change with Na_2S content, although the change is not so dramatic as it is with FSDP in Q[S(Q)-1]. The changes in the high-Q peaks suggest that the immediate atomic ordering, including the first neighbor atomic coordination, also experiences changes with Na_2S content.

5.4.4 Atomic PDF function G(r) from synchrotron x-ray diffraction

The PDF functions from synchrotron x-ray diffraction, G(r) , were obtained by Fourier transforming Q[S(Q)-1] with Q_{max} = 25 Å and are shown in Figure 5-5. It should be noted that the significant difference between the neutron and x-ray results is that the peak assigned to B-S correlation splits into two components at 1.8 Å and 1.93 Å, respectively, for the two glasses containing Na_2S. Because the neutron data were collected only over a range of out to 16 $Å^{-1}$, whereas the x-ray data extend up to 25 $Å^{-1}$, the larger Q_{max} used in Fourier transformation of the x-ray diffraction data allows greater resolution in x-ray diffraction PDFs. This in turn suggests that more local structure information in the glasses can be obtained from the x-ray data.

Similar to the neutron data, the B-O correlation peak at 1.4 Å is observed and increases with the addition of Na_2S. For pure B_2S_3, the peak at 1.8 Å can be assigned to the B-S correlation in trigonally coordinated borons. With the addition of Na_2S, this peak splits into two components at 1.8 Å and 1.93 Å, respectively. The peak at the slightly longer distance of 1.93 Å is assigned to the B-S correlation in tetrahedrally coordinated $BS_{4/2}$ units. In the crystal $Na_6B_{10}S_{18}$, the B-S distance in tetrahedral coordinated boron structure is found to lie between 1.879 Å and 1.951 Å [28]. The peak at 3.1 Å is attributed mostly to S-S correlations since the weighting factor for S-S (0.6) is much larger than that of B-B (0.02), as shown in Table 5-1.

5.5 Discussion

In the study of the short-range structure of glasses, it is often found that both the glass and the crystal share similar structural units because the short-range order is dominated by bond strength and atomic size packing features of the atoms (ions) in the material. The similarities between the short-range atomic ordering in glasses and the corresponding crystals were first pointed out by Zachariasen in a study of the silicate glasses [30]. Since, however, glasses lack the 3-D order of crystals, the structures of glasses and corresponding crystals usually disagree substantially at longer-range real space distances. For example, while the structure of both *v*-B_2O_3 and *c*-B_2O_3 are built up from trigonal $BO_{3/2}$ unit with approximately the same B-O distances and O-B-O bond angles, *v*-B_2O_3 is observed to have significant ordering at the intermediate range to form the well-known 6-membered boroxol B_3O_3 rings, whereas *c*-B_2O_3 does not possess any such rings [31]. In a similar way, the structure of *c*-B_2S_3 crystal has been studied by Diercks and Krebs [6] and they suggest that the structure of *c*-B_2S_3 is comprised of a stack of layers made of four-membered B_2S_2 rings bridged to six-membered B_3S_3 rings as shown in Figure 5-1.

A model atomic PDF of *c*-B_2S_3 calculated on the basis of this structure is compared to the experimental x-ray PDF for B_2S_3 glass in Figure 5-6. As can be seen in Figure 5-6, the model and experimental PDF data are similar to each other for short interatomic distances including the first near neighbor B-S (~1.8 Å) and S-S (~ 3.1 Å) atomic separations. This similarity suggests that the short range atomic ordering in both the crystal and the glass share similar features, i.e., they are built with the BS_3 unit with similar B-S distances and S-B-S angles. The model and experimental PDF data, however, disagree at longer (intermediate range) real space distances, in particular beginning around 4 Å. The model PDF shows a strong peak at ~ 4 Å reflecting the presence of the repeating layers in the crystal. There is no such a strong peak in the experimental PDF suggesting that B_2S_3 glass does not have the layered structure of the corresponding crystal as might be expected from its three dimensional disordered structure.

With the addition of Na_2S as a glass modifier to B_2S_3, the structure of the glasses changes in significant way. The NMR, IR and Raman studies have shown that as in the alkali borate glasses, tetrahedrally bonded boron groups, $BS_{4/2}$, are formed with added modifier [8, 12-17]. However, unlike the alkali borate glasses as described above, these $BS_{4/2}$ groups form at an extraordinary, "super-stoichiometric" rate. The $Na_2S + B_2S_3$ glasses have the highest conversion rate (approximately eight tetrahedral groups for every added Na_2S) of the alkali thioborate glasses. This compares to the alkali borate glasses where the stoichiometric rate of two tetrahedral boron groups form for every added alkali oxide independent of the alkali. One possible structure which incorporates large fractions of $BS_{4/2}$ units in alkali thioborate systems is comprised of a pyramidal arrangement of $BS_{4/2}$ units with trigonally coordinated sulfur atoms and six-membered ring groups around the outer edges and was proposed by zum Hebel et al. [32]. This structure is found in the compound $Na_6B_{10}S_{18}$ ($3Na_2S + 5B_2S_3$, x=0.375) and is

reproduced in Figure 5-7 (c) [26]. A formation mechanism for this structure from trigonal $BS_{3/2}$ to B_3S_3 units as proposed by Conrad and Krebs is shown in Figure 5-7 [33]. First, with just one additional sulfide (from M_2S) and one planar B_3S_3 boron-sulfur unit, a B_4S_{10} macrotetrahedral unit can be formed. In a similar way, a $B_{10}S_{18}$ unit can be formed from the addition of two more B_3S_3 units to one B_4S_{10} unit.

To help understand the structure of the alkali modified glasses, we have compared the experimental PDF of the $0.15Na_2S + 0.85B_2S_3$ glass with model ones created from the known structures of crystalline B_2S_3 and $Na_6B_{10}S_{18}$, where boron atoms adopt trigonal and tetrahedral coordinations, respectively. The comparison is given in Figure 5-8. As can be seen the first peak in the model PDF for crystalline B_2S_3 is positioned at ~ 1.8 Å, which is the B-S distance with trigonally coordinated boron. The first peak in the model PDF of crystalline $Na_6B_{10}S_{18}$ is positioned at ~ 1.93 Å and is the B-S distance with tetrahedrally coordinated boron. These first peaks of the model PDFs agree very well with the two components (trigonal and tetrahedral borons) of the first peak in the experimental PDFs. It is reasonable to assume therefore that the boron atoms in the $0.15Na_2S + 0.85B_2S_3$ and $0.20Na_2S + 0.80B_2S_3$ glass are both 3-fold and 4-fold coordinated by sulfur atoms. As can be seen in Figure 5-5, the second peak in the PDF of the glass (at ~ 3.1 Å) is better matched by the model PDF based on $Na_6B_{10}S_{18}$ structure. However, the number of S-S pairs in the $Na_6B_{10}S_{18}$ crystal is much larger than the one S-S pairs observed in crystalline B_2S_3. Obviously, the emerging tetrahedrally coordinated borons are accompanied by the creation of a large number of S-S pairs. Such a profound change in the immediate atomic ordering would inevitably involve a restructuring of the glassy network at longer-range distances as reflected by the dramatic change in the first sharp diffraction peak in

the S(Q) data. A fragment of $Na_6B_{10}S_{18}$ structure showing the B-S tetrahedral units of the type that are likely to occur in $Na_2S + B_2S_3$ glasses is shown in Figure 5-7 (c).

5.6 Conclusions

Neutron and synchrotron x-ray diffraction experiments have been performed on $xNa_2S + (1-x)B_2S_3$ ($x \leq 0.2$) glasses at room temperature. Systematic changes were observed in the FSDP with the increase of Na_2S content, and these suggest that there are changes in the degree of medium-range order. Both x-ray and neutron diffraction results provide the nearest neighbor atomic correlations in the atomic PDF functions G(r). Similar atom-atom distances were obtained both in the neutron and x-ray experiments. The significant difference is that in the x-ray diffraction data, the peak at 1.8 Å splits into two components, one at 1.8 Å and one at 1.93 Å, with the addition of Na_2S content. This result shows that the coordination of boron atoms undergoes transformation from trigonal to tetrahedral. Results of our diffraction and modeling studies provide direct structural evidence that doping B_2S_3 with Na_2S creates a large number of tetrahedrally coordinated boron and S-S pairs in the glass. It is likely that a structure of a pyramidal arrangement of BS_4 units, which is found in $Na_6B_{10}S_{18}$ polycrystalline, also occurs in $Na_2S + B_2S_3$ glasses.

5.7 Acknowledgements

This work was supported in part by NSF through grants DMR-9972466 and DMR-0304391. This work has benefited from the use of the Intense Pulsed Neutron Source and the Advanced Photon Source at Argonne National Laboratory. Thanks are given to J. Siewenie and Q. Mei from IPNS for the assistance with neutron experiments. M. Beno and Y. Ren from APS are thanked for the help with X-ray experiments. Use of both facilities was supported by the U. S.

Department of Energy, Office of Science, Office of Basic Energy Sciences, under Contract No. W-31-109-Eng-38.

5.8 Captions

Figure 5-1 Fragment of the layered structure of *c*-B_2S_3. Layers are made of chains of alternating four membered B_2S_2 and six membered B_3S_3 rings resulting in an average coordination number of three sulfur atoms for each boron. Boron atoms are represented as open and sulfur as solid circles

Figure 5-2 Neutron reduced structure functions Q[S(Q)-1] for $xNa_2S+(1-x)B_2S_3$ ($x \leq 0.2$) glasses (the curves have been offset for clarity)

Figure 5-3 Neutron atomic PDF functions G(r) of $xNa_2S + (1-x)B_2S_3$ ($x \leq 0.2$) glasses (the curves have been offset for clarity)

Figure 5-4 Synchrotron x-ray reduced structure functions $xNa_2S + (1-x)B_2S_3$ ($x \leq 0.2$) glasses (the curves have been offset for clarity)

Figure 5-5 Synchrotron x-ray atomic PDFs functions G(r) for $xNa_2S + (1-x)B_2S_3$ ($x \leq 0.2$) glasses (the curves have been offset for clarity)

Figure 5-6 Comparison between model (symbols) and experimental (line) PDFs for B_2S_3 glass. The model PDF is based on the structure of crystalline B_2S_3 shown in Fig. (5). First neighbor B-S and S-S atomic pairs are marked with arrows

Figure 5-7 Formation of B_4S_{10} and $B_{10}S_{20}$ macrotetrahedra from $BS_{3/2}$ and B_3S_3 redrawn from ref. [29]

Figure 5-8 Comparison between the experimental PDF for $0.15Na_2S + B_2S_3$ glass (symbols) and model PDFs for crystalline B_2S_3 (solid line) and crystalline $Na_6B_{10}S_{18}$ (broken line)

Table 5-1 Neutron and x-ray (at $Q = 0$ $Å^{-1}$) weighting factors for $xNa_2S + (1-x)\ B_2S_3$ ($x \leq 0.2$) glasses

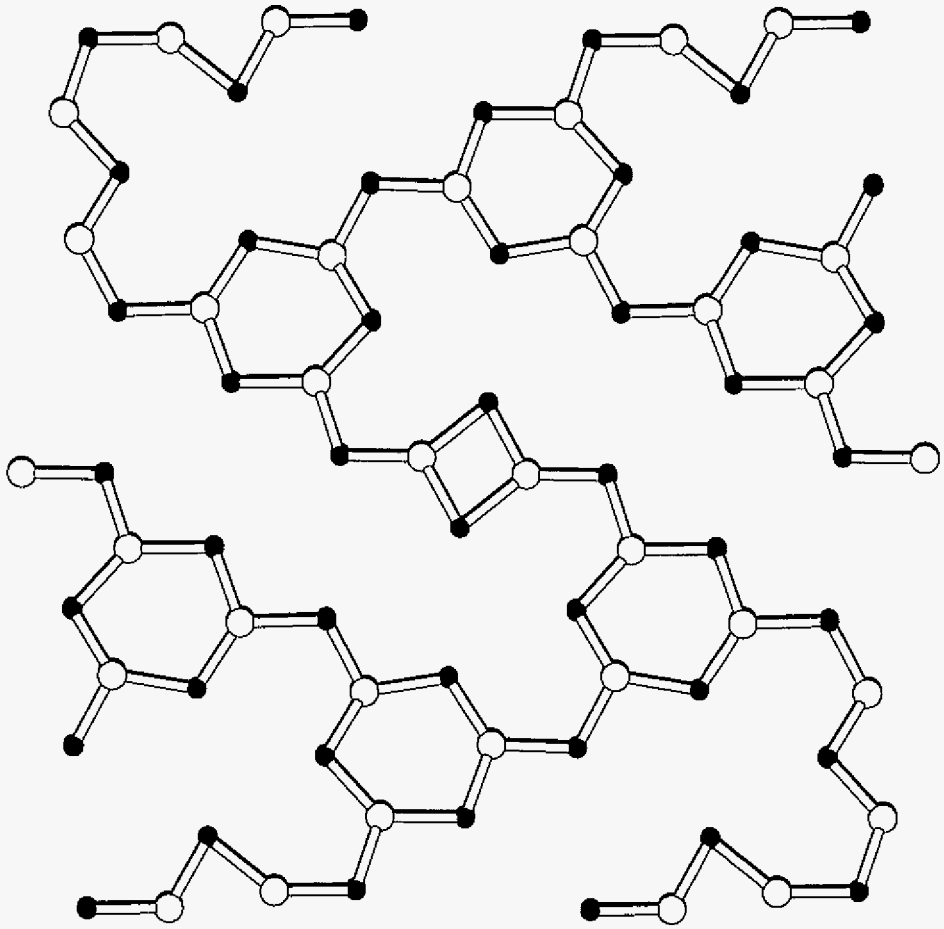

Figure 5- 1

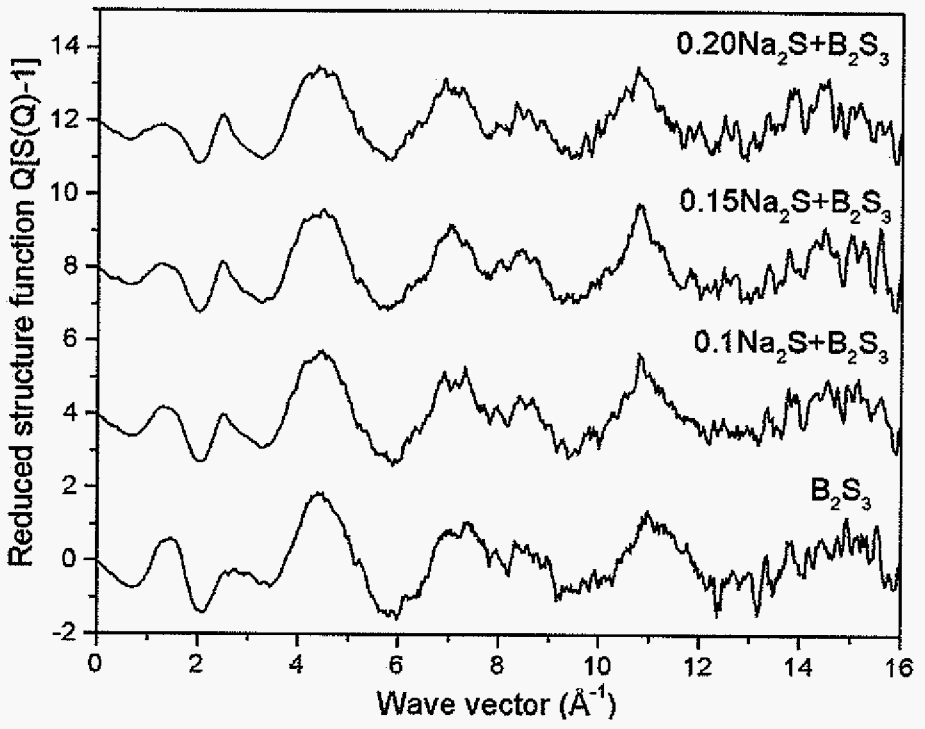
0.20Na2S+B2S3
0.15Na2S+B2S3
0.1Na2S+B2S3
B2S3
Reduced structure function Q[S(Q)-1]
Wave vector (Å-1)
14
12
10
8
6
4
2
0
-2
0
2
4
6
8
10
12
14
16

Figure 5- 2

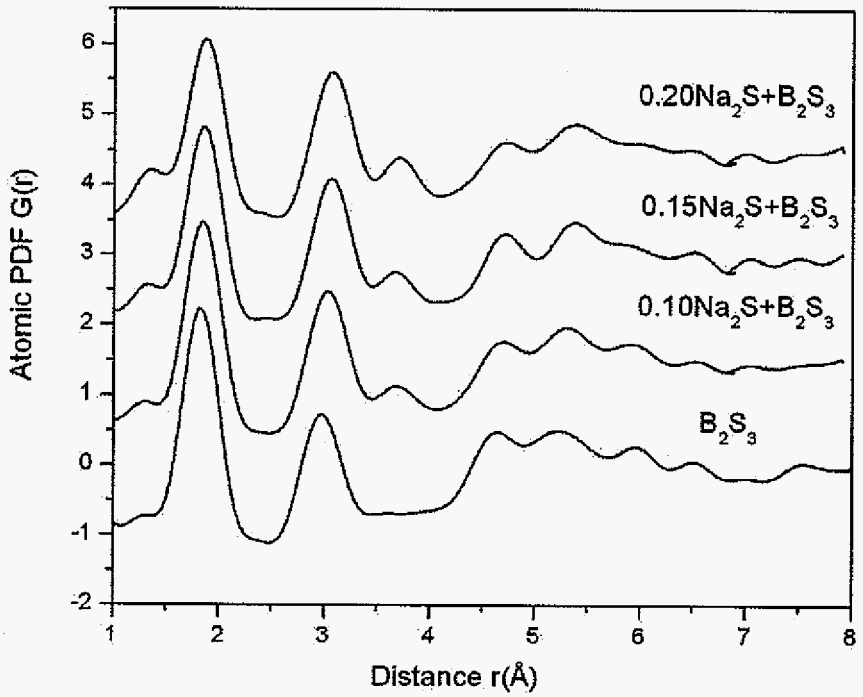
Atomic PDF G(r)
Distance r(Å)
0.20Na2S+B2S3
0.15Na2S+B2S3
0.10Na2S+B2S3
B2S3
6
5
4
3
2
1
0
-1
-2
1
2
3
4
5
6
7
8

Figure 5- 3

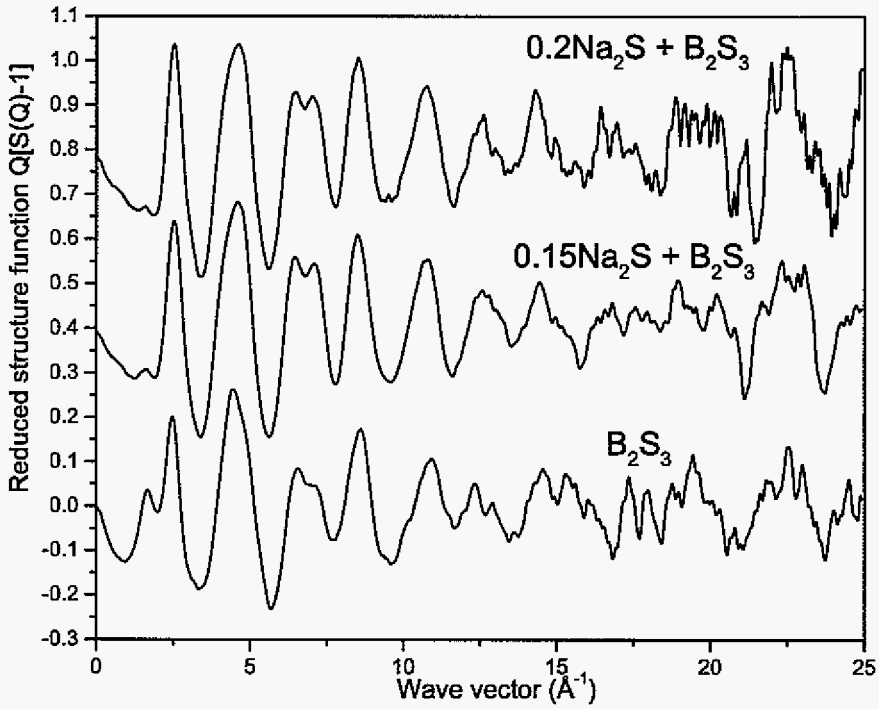
0.2Na2S + B2S3
0.15Na2S + B2S3
B2S3
Reduced structure function Q[S(Q)-1]
Wave vector (Å-1)
1.1
1.0
0.9
0.8
0.7
0.6
0.5
0.4
0.3
0.2
0.1
0.0
-0.1
-0.2
-0.3
0
5
10
15
20
25

Figure 5- 4

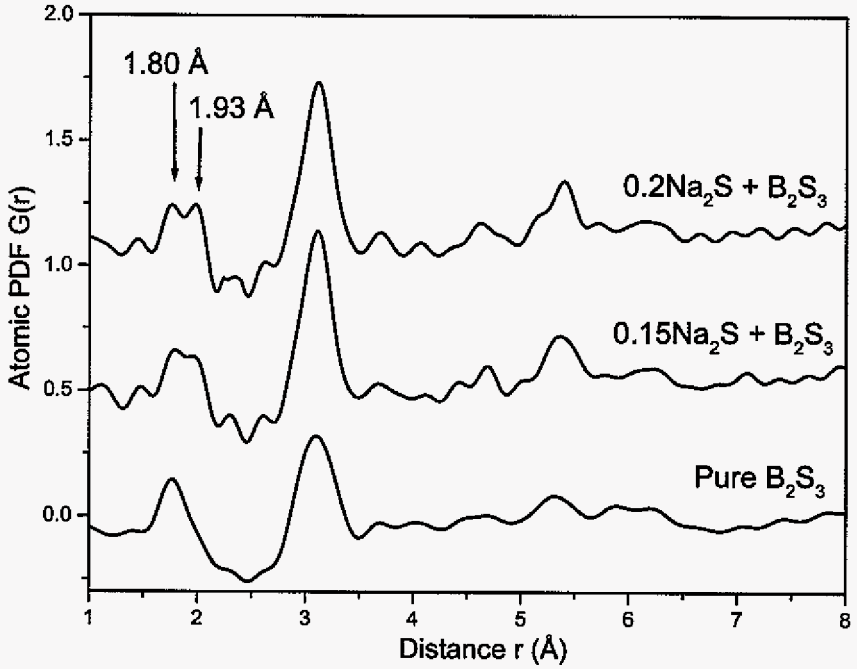
1.80 Å
1.93 Å
0.2Na2S + B2S3
0.15Na2S + B2S3
Pure B2S3
Atomic PDF G(r)
Distance r (Å)
2.0
1.5
1.0
0.5
0.0
1
2
3
4
5
6
7
8

Figure 5- 5

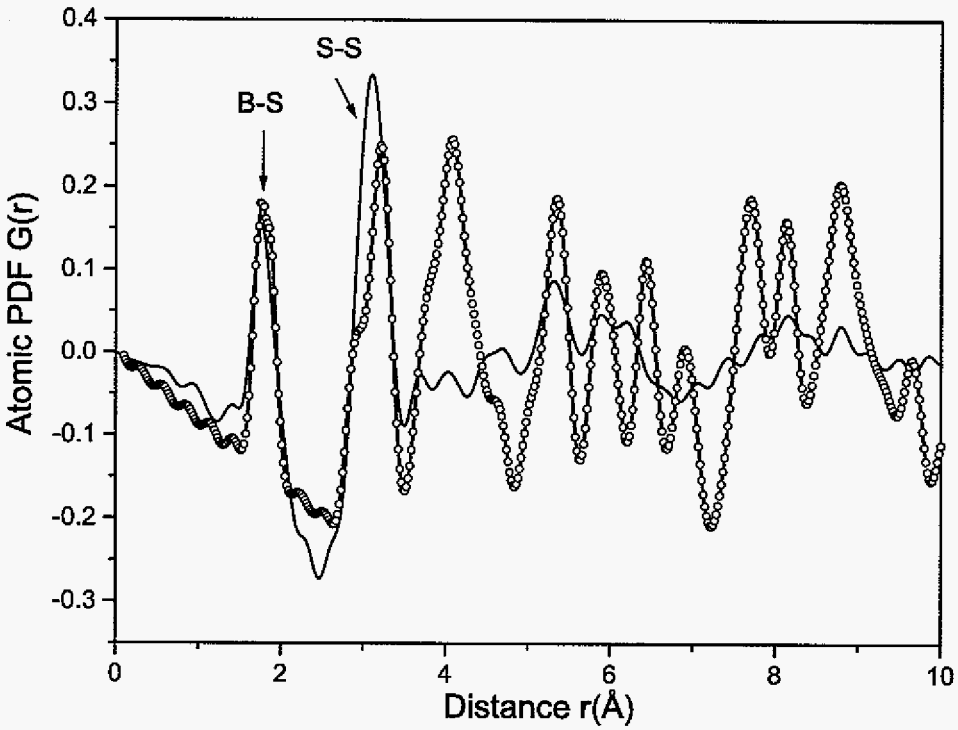

Figure 5- 6

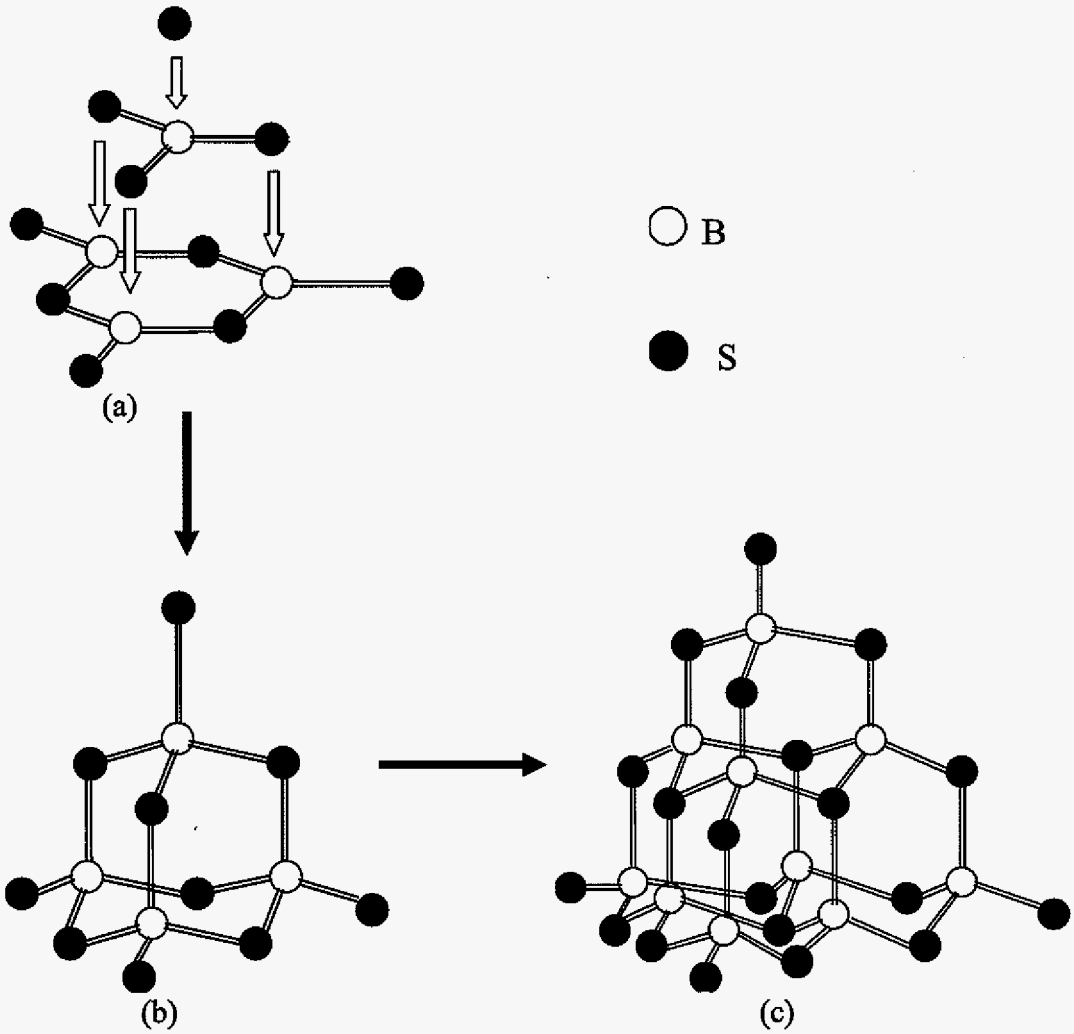

Figure 5- 7

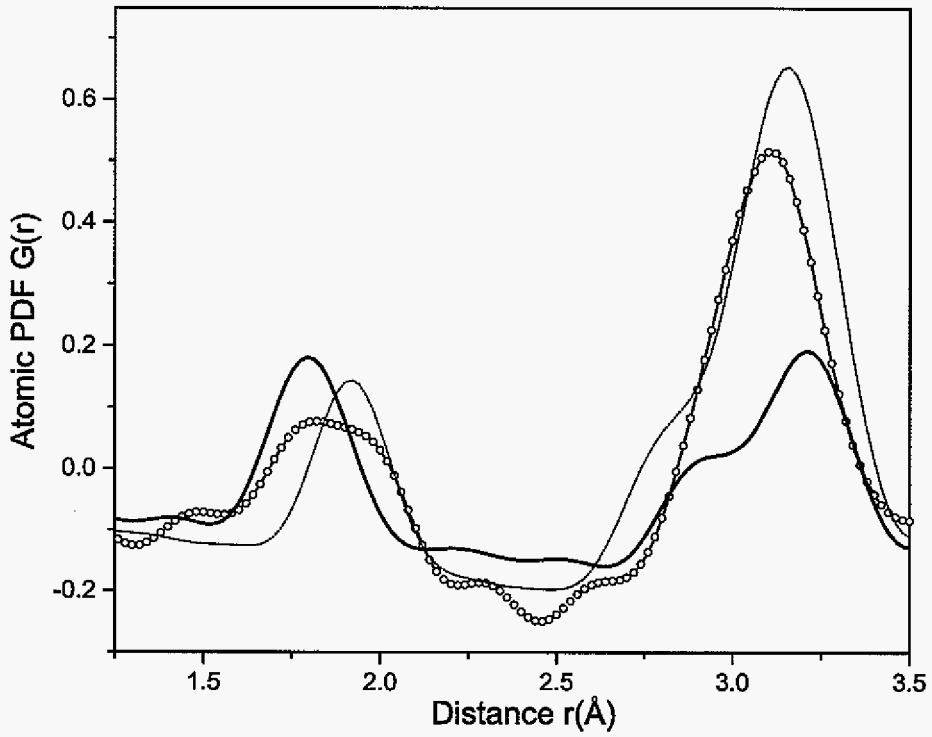

Figure 5- 8

Table 5- 1

	B-S	B-B	S-S	Na-S	Na-B	Na-Na
B_2S_3 neutron	0.476	0.834	0.153	--	--	--
B_2S_3 x-ray	0.285	0.0297	0.685	--	--	--
$0.1Na_2S$ neutron	0.447	0.335	0.145	0.027	0.041	0.001
$0.1Na_2S$ x-ray	0.257	0.026	0.640	0.063	0.013	0.002
$0.15Na_2S$ neutron	0.431	0.317	0.147	0.042	0.061	0.003
$0.15\ Na_2S$ x-ray	0.243	0.024	0.617	0.094	0.019	0.004
$0.2\ Na_2S$ neutron	0.414	0.298	0.144	0.056	0.081	0.006
$0.2\ Na_2S$ x-ray	0.228	0.022	0.594	0.126	0.024	0.007

5.9 References

[1] S.W. Martin, D.R. Bloyer, Journal of the American Ceramic Society 73 (1990) 3481.

[2] A. Pradel, M. Ribes, Materials Science & Engineering B3 (1989) 45.

[3] J. Kincs, S.W. Martin, Physical Review Letter 76 (1996) 70.

[4] A. E. Geissberger, F.L.Galeener, in: P.H. Gaskell, J.M. Parker, E.A. Davis (Eds), The Structure of Non-Crystalline Materials 1982, Taylor and Francis, London, (1983) 381.

[5] M.Menetrier, A.Hojjaji, A. Lavasseur, M. Couzi, K.J. Rao, Physics and Chemistry of Glasses 33 (1992) 222.

[6] H. Dietcks, B. Krebs, Angewandte Chemie International Edition 16 (1977) 313.

[7] R. N. Sinclair, C. E. Stone, A. C. Wright, S. W. Martin, M. L. Royle, A. C. Hannon, Journal of Non-Crystalline Solids 293-295 (2001) 383.

[8] S.-J. Hwang, C. Fernandez, J.P. Amoureux, J. -W. Han, J. Cho, S. W. Martin, M. Pruski, Journal of the American Ceramic Society 120 (1998) 7337.

[9] R.N. Sinclair, C.E. Stone, A.C. Wright, I.G. Polyakova, N.M. Vedishcheva, B.A. Shakhmatkin, S.A. Feller, B.C. Johanson, P. Venhuizen, R.B. Williams, A.C. Hannon, Physics and Chemistry of Glasses 41(2000) 286

[10] J.W. Zwanziger, R.E. Youngman, M. Braun, Borate Glasses, Crystals & Melts, (Proceedings of the International Conference on Borate Glasses, Crystals & Melts), 2nd Abingdon, UK, July 22-25 1996 (1997) 21.

[11] J. Cho, Ph.D Thesis, Iowa State University (1995).

[12] J.A. Sills, S. W. Martin, D.R. Torgeson, Journal of Non-Crystalline Solids 194 (1996) 260.

[13] D.R. Bloyer, J. Cho, S.W.Martin, Journal of the American Ceramic Society 76[11] (1993) 2753.

[14] J. Cho, S. W. Martin, Journal of Non-Crystalline Solids 182 (1995) 248.

[15] M. Royle, J. Cho, S. W. Martin, Journal of Non-Crystalline Solids 279 (2001) 97.

[16] J. A. Sills, S. W. Martin, D. R. Torgeson, Journal of Non-Crystalline Solids 168 (1994) 86.

[17] J. Cho, S. W. Martin, B. Meyer, K.-H. Kim, D. R. Torgeson, Journal of Non-Crystalline Solids 270 (2000) 205.

[18] K.S. Suh, A. Hojjaji, G. Villeneuve, M. Menetrier, A.J. Levasseur, Journal of Non-Crystalline Solids 128 (1) (1991) 13.

[19] C. Estournes, A.P. Owens, M. Menetrier, A. Levasseur, K. J. Rao, S. R. Elliott, Journal of Non-Crystalline Solids 171 (1994) 80.

[20] V. F. Sears, Neutron News. 3 (1992) 26.

[21] J. H. Hubbell, W. J. Veigele, E. A. Briggs, R. J. Howerton, Journal of Physical and Chemical Reference Data 4 (1973) 471.

[22] A. K. Soper, W. S. Howells, A. C. Hannon, Rutherford Appleton Laboratory Report, (1989) 89-046.

[23] V. Petkov, Journal of Applied Crystallography 22 (1989) 387.

[24] S.R. Elliott, Journal of Physics: Condensed Matter 4 (1992) 7661.

[25] M.Misawa, D. L. Price, K. Suzuki, Journal of Non-Crystalline Solids 37 (1980) 85.

[26] R. J. Dejus, S. Susman, K. J. Volin, D. G. Montague, D. L. Price, Journal of Non-Crystalline Solids 143 (1992) 162.

[27] J.H. Lee, A. P. Owens, A. Pradel, A.C. Hannon, M. Ribes, S. R. Elliott, Physical Review B. 54 (1996) 3895.

[28] A. Hammerschmidt, P. zum Hebel, F. Hilttmann, B. Krebs, Zeitschrift für anorganische und allgemeine Chemie 622 (1996) 76.

[29] M. Misawa, Journal of Non-Crystalline Solids 122 (1990) 33.

[30] W. H. Zachariasen, Journal of the American Ceramic Society 54 (1932) 3841.

[31] R. L. Mozzi, B. E. Warren, Journal of Applied Crystallography 3 (1970) 251.

[32] P. zum Hebel, B. Krebs, M. Grune, W. Muller-Warmuth, Solid State Ionics 43 (1990) 133.

[33] O. Conrad, B. Krebs, Phosphorus, Sulfur and Silicon, 124&125 (1997) 37.

6. Conclusions

6.1 General conclusions

Although many models have been proposed to explain the ionic conductivity in fast ionic conducting glasses, there is no generally accepted theory. One problem is to experimentally determine the separate influence of carrier density and mobility on the ionic conductivity in glasses. Resolving this problem can give a guide to further optimize the ionic conductivity in these glasses. Hence, this study investigated the structure and ionic conductivity in wide composition range glasses modified with Li, Na, K, and Cs cations to explore the role of the size of the cation and to determine the carrier density by space charge measurements for the first time to better understand the ion transport in the fast ionic conducting chalcogenide glasses.

A series of alkali sulfide, M_2S, and alkali iodide, MI, where M is Li, Na, K, and Cs, doped $0.1Ga_2S_3 + 0.9GeS_2$ glasses were studied since the ionic radius plays an important role in determining the ionic conductivity in glasses. Firstly, the structure of these glasses was characterized by Raman and IR spectroscopy. It was found that non-bridging sulfurs form in the glass structure with the addition of alkali sulfide. Different from Li_2S and Na_2S glasses, a peak at ~200 cm^{-1} in Raman spectra of K_2S and Cs_2S glasses indicates the existence of adamantine-like $Ge_4S_{10}^{4-}$ structure. As a further difference, in the other alkali iodide doped glasses, the three non-bridging sulfur peak at 385 cm^{-1} in the Raman spectra of $0.6Na_2S + 0.4(0.1Ga_2S_3 + 0.9GeS_2)$ glasses split into two peaks with the addition of NaI. This suggests that NaI may enter the glass structure instead of entering the interstitials in the glass structure network, like it appears to do in many other similar halide doped glasses.

Secondly the ionic conductivities of these glasses have been investigated. As expected, both additions of alkali sulfide (M_2S) and alkali iodide (MI) help to improve the conductivity of glass. It was found, however, that the conductivity 60% Na_2S doped glasses reaches saturation with the addition of NaI. The alkali radius was found to significantly increase the conductivity activation energy which leads to the large difference of ionic conductivities between Li_2S, Na_2S glasses and K_2S and Cs_2S glasses.

Thirdly for the first time, the charge carrier density in fast ionic conducting chalcogenide glasses was determined by space charge polarization theory. The temperature dependence of the charge carrier density was used to estimate the activation energy for mobile charge carrier density, ΔE_b. Both a simple well studied oxide glass, $LiPO_3$, and the sulfide glasses described above were examined. It was found that the oxide glass had a larger ΔE_b than the corresponding Li sulfide glass and this behavior is consistent with the expected weaker binding energy in sulfide glasses compared to oxide glasses. With values of the ΔE_b, values for the strain energy for ionic conduction were determined by difference through the relationship $\Delta E_s = \Delta E_{act} - \Delta E_b$, where ΔE_{act} is the total conductivity activation energy.

In addition, the structures of low-alkali-content $Na_2S + B_2S_3$ ($x \leq 0.2$) glasses were studied by neutron and synchrotron X-ray diffraction. The significant difference is that in the x-ray diffraction data, the peak at 1.8 Å splits into two components, one at 1.8 Å and one at 1.93 Å, with the addition of Na_2S content. This result shows that the coordination of boron atoms undergoes transformation from trigonal to tetrahedral. Results of our diffraction and modeling studies provide direct structural evidence that doping B_2S_3 with Na_2S creates a large number of tetrahedrally coordinated boron and S-S pairs in the glass.

6.2 Recommendations for future research

One of the most challenging parts of this study is the determination of mobile carrier density. To use the current method to determine the mobile carrier density precisely, more appropriate equivalent circuit and higher quality experimental data is required since the experimental data covers a wide range of frequency from 10^{-3} to 10^{7} Hz. Also highly polished and thinner samples help to obtain extensive compositions data and better data and avoid too many factors considered in the electrode effect. It was found that the input impedance of the present measuring system using a Solartron 1260 impedance analyzer was too small to enable highly accurate measurements when the overall conductivity of the sample became small as was the case for most of the K and Cs glasses.

7. Acknowledgements

I would like to thank Dr. Steve W. Martin for his expert guidance and support throughout my graduate study. He gave me the opportunity to work on several challenging research projects and provided me with many engineering experiences in the research lab.

I also would like to thank all of the members of the Glass and Optical Materials group at Iowa State who have worked with me for their help on experiments and many thoughtful discussions. I would especially like to thank Hang Yan Yuen, Youngsik Kim, Jason Saienga, Chad Martindale, Qiang Mei, Kyle Berg, Bryce Campbell, Carly Nelson, Inseok Seo, Ben Meyer, Steve Poling, and Annamalai Karthikeyan.

Grateful acknowledgement is given to the National Science Foundation for providing financial support of my research under grant DMR 0312081.

Finally, I give special thanks to my parents, Miaoshui Yao and Huilan Chen, and my wife, Jing Liu, for their love and support in my life.